

**Star-Disc Encounters in Young Star Clusters:  
Environmental Effects on the Evolution of Protoplanetary Discs**

In a u g u r a l - D i s s e r t a t i o n

zur

Erlangung des Doktorgrades

der Mathematisch-Naturwissenschaftlichen Fakultät

der Universität zu Köln

vorgelegt von

Christoph Olczak

aus Waldenburg (Polen)

Köln 2009

Berichtersteller/in: Prof. Dr. Susanne Pfalzner .....

Prof. Dr. Joachim Krug .....

Tag der mündlichen Prüfung: 13. Januar 2009

# Kurzzusammenfassung

Gemäß heutigem Kenntnisstand entstehen Sterne bevorzugt in Sternhaufen. Die Akkretions-scheiben, welche als Nebenprodukt des Sternentstehungsprozesses die jungen Sterne umgeben, stellen potentielle Geburtsstätten von Planeten und Planetensystemen dar. Eingebettet in einen Sternhaufen, unterliegen diese protoplanetaren Scheiben potentiell Wechselwirkungen mit Sternen. Diese Wechselwirkungen geben Anlass zu einer fundamentalen Frage der Sternentstehung in Sternhaufen: Inwieweit nimmt die Umgebung des Sternhaufens Einfluss auf die Entwicklung von protoplanetaren Scheiben und die Entstehung von Planeten?

Diese Frage wird in der vorliegenden Arbeit im Hinblick auf den Effekt gravitativer Wechselwirkungen von Sternen und deren Scheiben in jungen Sternhaufen behandelt. Die Untersuchung erfolgt durch die Kombination numerischer Simulationen isolierter Vorbeiflüge von Sternen an Stern-Scheibe-Systemen und der Stelldynamik junger Sternhaufen.

Die Untersuchung umfasst drei Schlüsselaspekte. Zum einen wird anhand von Simulationen eines dynamischen Modells des Sternhaufens im Orionnebel (ONC) gezeigt, dass die Zerstörung von Scheiben durch gravitative Wechselwirkungen mit massiven Sternen im Zentrum des Sternhaufens dominiert wird, welche als Gravitationszentren für Sterne geringer Masse dienen. Die massiven Sterne unterliegen somit wiederholten Wechselwirkungen welche zu einer kompletten Zerstörung der Scheibe führen können. Der Massenverlust der Scheibe erfolgt dabei schneller und weitreichender als dies für Sterne mittlerer Masse der Fall ist.

Zweitens wird die Frage untersucht, ob Beobachtungsgrößen existieren, mit deren Hilfe der durch gravitative Wechselwirkungen entstehende Massenverlust in Scheiben aufgezeigt werden kann. Die numerischen Simulationen ergeben, dass einige Sterne unerwartet hohe Geschwindigkeiten und zugleich zerstörte Scheiben als Folge von starken Wechselwirkungen aufweisen. Ein Vergleich mit Beobachtungen des ONC bestätigt das Vorhandensein solcher Sterne hoher Geschwindigkeit. Es handelt sich um junge Sterne, welche teilweise keine erhöhte Emission im Infraroten aufweisen. Die Sterne hoher Geschwindigkeit bilden ein charakteristisches Muster, welches anhand der numerischen Simulationen, die eine Korrelation zwischen anfänglicher Lage und Scheibenzerstörung aufzeigen, geklärt wird.

Ferner wird der Einfluss der Eigenschaften eines Sternhaufens auf den durch gravitative Wechselwirkungen bedingten Scheibenmassenverlust untersucht. Dies erfolgt durch Skalierung der Größe, Dichte und Anzahl der Sterne des dynamischen Ausgangsmodells des

ONC. Wie erwartet zeigt sich, dass der Scheibenmassenverlust mit der Dichte des Sternhaufens zunimmt, jedoch von der Größe der Sternenpopulation unberührt bleibt. Allerdings ist die Auswirkung der gravitativen Wechselwirkungen selbst in vier mal dünneren Sternhaufen sichtbar. Die Dichte des ONC stellt dabei einen Schwellenwert dar: in dünneren und weniger massiven Sternhaufen dominieren die massiven Sterne den durch gravitative Wechselwirkungen bedingten Scheibenmassenverlust während in dichteren und massiveren Sternhaufen die Sterne geringer und mittlerer Masse die entscheidende Rolle bei der Reduzierung der Scheibenmasse spielen.

# Abstract

According to current knowledge, star formation occurs preferentially in clustered environments. As a byproduct of the star formation process young stars are found to be surrounded by accretion discs that are potential birth places of planets and planetary systems. Located in the hosting cluster, these protoplanetary discs are potentially subject to stellar interactions. These interactions give rise to a fundamental question of clustered star formation: How far does the cluster environment affect the evolution of protoplanetary discs and the formation of planets?

The question is addressed in the present investigation in terms of the effect of stellar encounters on stars and their disc in young clusters by combining numerical simulations of isolated star-disc encounters and stellar dynamics of young star clusters.

The investigation is composed of three key aspects. First, simulations of a dynamical model of the Orion Nebula Cluster (ONC) show that disc destruction is dominated by encounters with high-mass stars that act as gravitational foci for the lower mass stars in the cluster centre. The massive stars are thus subject to repeated encounters which can lead to a total disc destruction. This happens much more quickly and to a larger degree than for intermediate-mass stars.

Secondly, the question whether there are any observables that could trace the mechanism of encounter-induced disc-mass loss, is addressed. From numerical simulations it is found that some stars show unexpectedly high velocities as an outcome of close interactions, combined with a completely destroyed disc. Observations of the ONC confirm the presence of these high-velocity stars, which are young low-mass stars that partially lack infrared excess emission. The high-velocity stars form a characteristic pattern that is explained by the numerical simulations, finding a strong correlation between initial location in the cluster and disc destruction dynamics.

Third, the influence of the cluster properties on the encounter-induced disc-mass loss is investigated by scaling the size, density and stellar number of the basic dynamical model of the ONC. Not unexpectedly, it is found that the disc-mass loss increases with cluster density but remains rather unaffected by the size of the stellar population revealing that even in clusters four times sparser than the ONC the effect of encounters is still *non-negligible*. The density of the ONC itself marks a threshold: in less dense and less massive clusters it is the massive

stars that dominate the encounter-induced disc-mass loss whereas in denser and more massive clusters the low- and intermediate-mass stars play the major role for the removal of disc mass.

# Contents

<b>1. Introduction</b>	<b>1</b>
<b>2. Young Star Clusters</b>	<b>5</b>
2.1. Cluster Dynamics . . . . .	5
2.2. Star Formation . . . . .	8
2.3. Cluster Formation . . . . .	19
2.4. The Initial Mass Function (IMF) . . . . .	25
<b>3. Numerics</b>	<b>29</b>
3.1. Introduction . . . . .	29
3.2. The Code: NBODY6++ . . . . .	31
3.3. Modifications of the Code . . . . .	40
<b>4. Environmental Effect on Discs in the Orion Nebula Cluster (ONC)</b>	<b>55</b>
4.1. Structure and Dynamics of the ONC . . . . .	55
4.2. Construction of a Numerical Model of the ONC . . . . .	58
4.3. Dynamical Evolution of the Numerical Cluster Model . . . . .	63
4.4. Disc-Mass Loss Induced by Star-Disc Encounters . . . . .	65
<b>5. Dynamical Imprints of Star-Disc Encounters in the ONC</b>	<b>81</b>
5.1. Introduction . . . . .	81
5.2. Observations . . . . .	81
5.3. Numerical Simulations . . . . .	91
5.4. Confronting Observations and Simulations . . . . .	100
<b>6. The ONC Revisited - A Family of Numerical Siblings</b>	<b>103</b>
6.1. Introduction . . . . .	103
6.2. Construction of the Numerical Models . . . . .	104
6.3. Dynamical Evolution of the Numerical Cluster Models . . . . .	107
6.4. Disc-Mass Loss Induced by Star-Disc Encounters . . . . .	115
6.5. Validity of the Results . . . . .	130

<b>7. Discussion</b>	<b>135</b>
<b>8. Summary</b>	<b>139</b>
<b>Bibliography</b>	<b>141</b>
<b>A. Conic Sections</b>	<b>155</b>
<b>B. Observational Constraints</b>	<b>157</b>
B.1. Observability of tidal tails due to star-disc encounters in the ONC . . . . .	157
B.2. Estimate of the mean uncertainty of stellar ages . . . . .	157
<b>C. Stellar Dynamics</b>	<b>159</b>
C.1. Minimum velocity for unperturbed escape of stars in the ONC . . . . .	159
C.2. Maximum velocity of a star ejected from a bound triple system . . . . .	159
<b>D. Star Cluster Models</b>	<b>161</b>
D.1. Determination of boundaries of mass groups . . . . .	161

# 1. Introduction

According to current knowledge, planetary systems form from the accretion discs around young stars. These young stars are in most cases not formed in isolation but are part of a cluster (e.g. Lada & Lada, 2003). Stellar number densities in these cluster environments vary considerably, spanning a range from  $10 \text{ pc}^{-3}$  (e.g.  $\eta$  Chamaeleontis) to  $10^6 \text{ pc}^{-3}$  (e.g. Arches Cluster). It is still an open question as to how far interactions with the surrounding stars influence planet formation in young clusters - in particular in the dense, massive stellar aggregates ( $n \gtrsim 10^4 \text{ pc}^{-3}$ ), where close interactions of stars are much more likely and the gravitational impact of massive stars is higher. In the last decade many young star clusters have been surveyed for the properties of the stellar members and their circumstellar discs (e.g. Haisch *et al.*, 2001; Hillenbrand, 2002; Sicilia-Aguilar *et al.*, 2006; Currie *et al.*, 2008). The general outcome has been that these discs disperse over time and in dense clusters the disc frequency seems to be lower in the core (e.g. Balog *et al.*, 2007b). This is attributed to external violent processes like photoevaporation or encounter-induced disc-mass loss, mainly caused by the massive stars that are concentrated in the cluster core.

Earlier numerical investigations seemed to indicate that photoevaporation should by far dominate the external disc destruction (Sclally & Clarke, 2001; Adams *et al.*, 2004). The question of whether encounters play a vital role in the formation process of stars and planets has been studied far less and is still open (e.g. Adams *et al.*, 2006). Analytical estimates of dynamical time scales and restrictions of numerical simulations to single-mass models led to the conclusion that encounters do not play an important role (e.g. Clarke & Pringle, 1993; Sclally & Clarke, 2001) in the general clustered star formation process but only when number densities approach those observed in globular clusters (Bonnell *et al.*, 2001b). Nevertheless, Sclally & Clarke (2001) found that nearly a third of stars in the central core of the ONC would suffer an encounter within 100 AU, and thus, for a significant minority of stars in the Trapezium Cluster star-disc encounters could be of some importance. However, a number of simplifying assumptions underlie this result that tend to underestimate the effect of stellar encounters as a disc-destructive mechanism.

Only recently has it been shown by simulations of isolated star-disc encounters (e.g. Pfalzner *et al.*, 2005b; Moeckel & Bally, 2006, 2007a,b) and combination with numerical models of the Orion Nebula Cluster (ONC) (Olczak *et al.*, 2006; Pfalzner *et al.*, 2006; Pfalzner, 2006;

Pfalzner & Olczak, 2007a,b) that stellar encounters do have an effect on the discs surrounding stars in a young dense cluster (see also the review by Zinnecker & Yorke, 2007). The importance of encounters has been previously underestimated because the focus has been mainly on encounters between solar mass stars (e.g. Clarke & Pringle, 1991; Heller, 1995). However, discs are most affected when the masses of the stars involved in the encounter are unequal (Olczak *et al.*, 2006; Moeckel & Bally, 2007a). Moreover, the massive stars in the centre of a stellar cluster act as gravitational foci for the lower mass stars and are thus subject to repeated encounters. These accumulated perturbations can lead to a total destruction of a massive star's disc (Pfalzner *et al.*, 2006).

Whether these results of the numerical simulations of a dynamical model of the ONC could be generalised towards other young star clusters has not been investigated so far. This would be in particular of interest in the light of the existence of much more massive and dense systems than the ONC. Naturally, one would expect that the effect of star-disc encounters becomes larger with increasing density and mass of a cluster. Indeed, recent observations of young star clusters do not only show a trend of decreasing disc fraction with time, as discussed above, but as well – most probably – a lower disc fraction in dense and massive clusters (Stolte *et al.*, 2004; Balog *et al.*, 2007b). However, observational biases prevent a decisive conclusion. First, the high density of these clusters makes the resolution of the individual stars – in particular in the even denser core – very challenging, as discussed for example by Schoedel *et al.* (2008). Second, because massive clusters are not found at distances closer than 2 kpc, their stellar population can not be sampled completely below one solar mass with current observational techniques and instruments (Stolte *et al.*, 2006; Kim *et al.*, 2006; Harayama *et al.*, 2008). According to the canonical mass function of Kroupa (2001), this means that about 90 % of the cluster population of massive clusters remains undetected. Third, because massive clusters tend to form more massive stars (e.g. Weidner & Kroupa, 2006), the effect of photoevaporation comes inevitably into play (e.g. Fatuzzo & Adams, 2008).

The evidence that stellar encounters do have a significant effect on discs in young star clusters is solely due to numerical investigations. Though perturbed discs in individual interacting star-disc systems have been observed (Beust *et al.*, 2005; Cabrit *et al.*, 2006; Lin *et al.*, 2006), a systematic investigation of such events in a young star cluster has not been undertaken so far. This is attributed to the low probability of tracing stellar encounters directly by observations due to their short duration and due to the fast dissipation of the disc perturbations on a time scale of  $10^3$  yr (cf. Pfalzner, 2003). One could overcome this observational limitation by tracing an observable that contains the information of an encounter event over a time scale comparable to the age of a cluster.

In this work the relevance of encounters on the destruction of protoplanetary discs in a young dense cluster is investigated by combining two different types of numerical simulations.

---

First, star-cluster simulations with NBODY6++ (Spurzem, 1999) are performed to model the stellar dynamics, the results of which are used to investigate the frequency of encounters, the mass ratio and separation of the stars involved, and the eccentricity of the encounter orbits. Second, the results of a parameter study of star-disc encounters are involved to determine the upper limits of the disc-mass loss in encounters of star-disc systems.

Here the ONC is used as a prototype young cluster because it is one of the best-studied regions in our galaxy, and the only young dense cluster for which velocities of more than 1000 of its members have been determined (Jones & Walker, 1988). In addition, its high density suggests that stellar encounters might be relevant for the evolution of circumstellar discs. Throughout this work it is assumed that initially all stars are surrounded by protoplanetary discs. This is justified by observations that reveal disc fractions of nearly 100% in very young star clusters (e.g. Haisch *et al.*, 2000; Lada *et al.*, 2000; Haisch *et al.*, 2001; Hillenbrand, 2005). The model of the ONC is used as a starting point for the development of numerical representations of other stellar systems that are used to investigate the dependence of the encounter-triggered disc-mass loss on the stellar number, stellar density, and size of a cluster. With these models it is aimed to investigate how stellar systems of different properties influence the effect of encounters on discs of young stars.

The other focus of this work is the question of whether there is direct observational evidence for encounters among star-disc systems and for disc-mass loss due to encounters in young clusters. It is difficult to distinguish observationally whether photoevaporation or gravitational interaction are responsible for the loss of (outer) discs. The reason is that in both cases interaction with a massive star is the most destructive process. Thus the observation of a decreased disc frequency in the cluster core, as mentioned above, does not allow one to favour either of the two mechanisms. The difficulty of tracing stellar encounters directly by observations is their short duration. Direct imaging of tidal tails of a disc would seem to be a good proof but the probability of such an event is very low: the perturbed disc circularises and tidal tails dissipate on a time scale of  $10^3$  yr. Nevertheless, there exist observations of tidal tails or spiral arms in star-disc systems (e.g. Beust *et al.*, 2005; Cabrit *et al.*, 2006; Lin *et al.*, 2006), but often it is unclear whether these can be attributed to the passage of an unbound perturber or a binary companion or gravitational instabilities caused by a giant planet. However, an unambiguous imprint of an encounter among stars is the high velocity of a star which has been expelled in a close gravitational interaction, mostly as a result of a three-body encounter (see Heggie, 1975). Thus an analysis of the velocity distribution of a cluster is the key to finding candidates of close encounters between young stars.

The present work is organised the following way. In Chapter 2 the formation and evolution of stars and star clusters and their fundamental properties are presented. Chapter 3 covers the description of the numerical code that has been used for the stellar dynamical

simulations. Extensions and modifications of the code that have been applied are addressed as well. Simulations of the numerical model of the ONC and, in combination with results from the parameter study of star-disc encounters, implications for the disc-mass loss in this young cluster are discussed in Chapter 4. This is followed, in Chapter 5, by an investigation of observable imprints of encounters in a young cluster from a combination of observational data and simulations of the ONC. An extension of the simulations of the dynamical model of the ONC towards two families of cluster models, scaled by density, size and stellar number, is presented in Chapter 6. A discussion of the results of the present work and a summary are given in Chapter 7 and Chapter 8.

## 2. Young Star Clusters

The formation of stars in the Galaxy occurs within groups scattered throughout the Galactic disc, with a strong concentration towards the spiral arms which harbour a large fraction of the Galactic molecular hydrogen. A large variety of sizes, shapes, densities and luminosities of stellar birthplaces is observed. These represent evolutionary stages during the formation of stellar groups from agglomerations of gas and dust to embedded clusters which will form later eventually open clusters or more likely disperse into unbound associations.

In the first section typical quantities and time scales of star cluster dynamics are presented. The second section deals with the most important stages of star formation, while in the third the properties and evolution of the hosting stellar groups will be described in more detail. Finally, the important concept of the Initial Mass Function (IMF) is discussed.

### 2.1. Cluster Dynamics

The dynamics of a star cluster are essentially determined by the gravitational interaction of its stellar population. Treated as particles, the cluster stars are representing – from the theoretical point of view – a (chaotic)  $N$ -body system. Though the motion of each star is thus unpredictable (on a longer time scale), the dynamics of the entire population can be well characterised by a set of fundamental physical quantities and time scales as discussed by Binney & Tremaine (1987).

The *virial ratio*,

$$Q_{\text{vir}} = \frac{E_{\text{kin}}}{|E_{\text{pot}}|} = \frac{R_{\text{hm}}\sigma^2}{GM}, \quad (2.1)$$

where  $E_{\text{kin}}$  and  $E_{\text{pot}}$  are the kinetic and potential energy,  $R_{\text{hm}}$  the half-mass radius,  $\sigma$  the velocity dispersion,  $G$  the gravitational constant, and  $M$  the cluster mass, describes the “thermal” state of a cluster: the larger the ratio, the larger the kinetic energy of a cluster – the cluster is termed to become “hotter”, in analogy to (collision-less) gas. Three regimes of the virial ratio are distinguished: a *cold* system is characterised by  $Q_{\text{vir}} < 0.5$ , a *hot* system has  $Q_{\text{vir}} > 0.5$ , while  $Q_{\text{vir}} = 0.5$  marks the state of *virial equilibrium*. This classification is due to the virial theorem which says that for any  $N$ -body system of mutually gravitating particles in a steady state  $E_{\text{pot}} = -2E_{\text{kin}}$ . Hence the virial ratio determines the evolution of the cluster volume:

a cold cluster will tend to contract, a hot cluster will expand with time, until equilibrium is reached.

The *crossing time*,

$$t_{\text{cr}} = \frac{2R_V}{\sigma}, \quad (2.2)$$

is the typical time scale for a particle to cross the hosting cluster. It represents the dynamical time scale of a self-gravitating system over which it adjusts globally to a significant deviation from an equilibrium state. Here  $R_V$  is the virial cluster radius, obtained from the potential energy  $E_{\text{pot}}$  by  $R_V = GN^2\bar{m}^2/2|E_{\text{pot}}|$ , where  $N$  is the number of particles,  $\bar{m}$  is the mean particle mass, and  $\sigma$  is the rms velocity dispersion (Binney & Tremaine, 1987). In a state of approximate equilibrium,  $\sigma^2 \simeq GN\bar{m}/2R_V$ , the crossing time can be expressed as

$$t_{\text{cr}} = 2\sqrt{2} \left( \frac{R_V^3}{GN\bar{m}} \right)^{1/2}. \quad (2.3)$$

The *close encounter distance*,

$$R_{\text{cl}} = 2 \frac{G\bar{m}}{\sigma^2}, \quad (2.4)$$

gives an estimate of the minimum distance between two stars. Thus it is a measure of the significance of collisions in a self-gravitating system (Aarseth & Lecar, 1975). The term ‘‘collision’’ here always refers to elastic two- or more-body encounters, not to physical collisions, where two stars collide and merge or disrupt each other. At equilibrium it takes the simple form

$$R_{\text{cl}} \simeq 4 \frac{R_V}{N}. \quad (2.5)$$

Another relevant time scale is the *two-body relaxation time*,

$$t_{\text{r2b}} = 0.34 \frac{\sigma^3}{G^2 m_* \rho_0 \ln \Lambda}, \quad (2.6)$$

where  $\sigma$  is again the velocity dispersion,  $m_*$  the stellar mass,  $\rho_0$  the stellar number density, and  $\Lambda = \gamma N$  the argument of the Coulomb logarithm with particle number  $N$  (Spitzer & Hart, 1971). Formally this factor is obtained by integrating over all impact parameters in two-body encounters, with a historical value of  $\gamma = 0.4$ . However, from numerical experiments Giersz & Heggie (1994) determined  $\gamma \simeq 0.11$ . The given two-body relaxation time is valid in the approximation of a homogeneous distribution of equal-mass stars with an isotropic Maxwellian velocity distribution. However, for a real star cluster the two-body relaxation

time varies by large factors between the central and outer parts. Thus it is useful to define a *half-mass relaxation time*,

$$t_{\text{rh}} = 0.138 \left( \frac{Nr_{\text{h}}^3}{Gm_{\star}} \right)^{1/2} \frac{1}{\ln \Lambda}, \quad (2.7)$$

where  $r_{\text{h}}$  is the half-mass radius. The relaxation time gives an estimate of the time for the rms velocity change arising from small angle deflections at the half-mass radius to become comparable to the initial velocity dispersion. Globally this means that significant dynamical changes of a self-gravitating system occur on this time scale and lead to a virialised (or “relaxed”) system.

The importance of encounters for a self-gravitating system to become relaxed can be expressed by the relation

$$\frac{t_{\text{rh}}}{t_{\text{cr}}} \simeq \frac{N}{22 \ln \Lambda}, \quad (2.8)$$

which gives an estimate of the number of cluster crossings of a particle before significant deflection. It shows that with increasing particle number encounters become less effective in changing cluster dynamics as a result of a deeper cluster potential. If the relaxation time of a self-gravitating system greatly exceeds the time interval of interest, the system can be approximately treated as collisionless.

To give an example of the numbers: a rich star cluster is characterised by  $N \simeq 10^4$ ,  $\bar{m} \simeq 0.5 M_{\odot}$ , and  $R_V \simeq r_{\text{h}} \simeq 4 \text{ pc}$ , which yields  $t_{\text{cr}} = 5 \cdot 10^6 \text{ yr}$ ,  $t_{\text{rh}} = 3 \cdot 10^8 \text{ yr}$ ,  $R_{\text{cl}} \simeq 3 \cdot 10^2 \text{ AU}$ , and  $t_{\text{rh}}/t_{\text{cr}} \simeq 10^2$ .

The presented relaxation time scale is only valid for equal mass systems. In the realistic case of a star cluster a mass spectrum has to be introduced. In the simplest approximation of a mass spectrum by a two-component system, dominated by the low-mass particles, another relevant time scale is the equipartition time for kinetic energy,

$$t_{\text{eq}} = \frac{(\bar{v}_1^2 + \bar{v}_2^2)^{3/2}}{8(6\pi)^{1/2} G^2 \rho_{01} m_2 \ln N_1}, \quad (2.9)$$

where  $\bar{v}_1$  and  $\bar{v}_2$  are the mean velocities of the two mass groups and  $\rho_{01}$  is the central density of the  $N_1$  low-mass stars of mass  $m_1$ . The high-mass particles of mass  $m_2$  lose kinetic energy through encounters with low-mass particles of mass  $m_1$  and spiral inwards. Finally the high-mass particles will form a self-gravitating system in the cluster core and the standard relaxation time (2.6) becomes relevant again, slowing down the evolution. This process is known as *mass segregation*. Combination of (2.9) and (2.7) gives the relation between the

two time scales,

$$\frac{t_{\text{eq}}}{t_{\text{rh}}} \simeq \frac{\bar{m}}{m_2}. \quad (2.10)$$

Hence the presence of a mass spectrum speeds up the early evolution of a self-gravitating system. Consequently, for rich young open star clusters, which typically have a mass range  $0.1\text{-}10 M_{\odot}$ , (2.7) overestimates the relaxation time by a factor of  $\lesssim 10^2$ . A re-estimate of the importance of close encounters in such a system results in  $t_{\text{rh}} \simeq t_{\text{cr}}$ , inevitably showing that young rich star clusters are strongly collision dominated systems. It is also evident that mass segregation of the massive stars occurs before relaxation of the entire cluster becomes significant. However, one has to emphasise that as yet there is no consistent theory of the relaxation time for a realistic mass spectrum.

Collisions between single stars modify the stellar distribution function in two ways. One process is *ejection*, in which a single close encounter leads one of the stars to acquire a velocity greater than the local escape velocity  $v_e$  and to escape from the cluster. The time scale for this is  $t_{\text{ej}} = -Ndt/dN \simeq 1.1 \cdot 10^3 \ln 0.4 N t_{\text{rh}} \simeq 10^4 t_{\text{rh}}$  (Henon, 1969). The second process is *evaporation* and is caused by the cumulative effect of many weak encounters, which gradually increase a star's energy until  $v \geq v_e$ . From detailed calculations Gerhard (2000) found a relation  $t_{\text{ev}} \simeq 300 t_{\text{rh}}$  for the evaporation time scale.

## 2.2. Star Formation

The star formation process is linked to the gravitational collapse of a cloud of gas, forming individual stellar objects of a large range of masses. These stellar objects are involved in an evolutionary process that is made up of four characteristic stages with the young star finally entering its *main sequence*, possibly surrounded by a planetary system that formed from a disc of circumstellar matter as a byproduct of the stellar evolution. The properties of the clouds, the isolated stellar evolution process and properties of the young stars' disc are described below in detail.

### 2.2.1. Molecular Clouds

Molecular clouds are the precursors of stellar formation and are observed in a great variety, as summarised in Table 2.1. However, only the cold and massive complexes like the giant molecular clouds or the less massive dark clouds, where the main cohesive force is the cloud's own gravity, are in favour to produce new stars. These large entities are built up by the agglomeration of many smaller clumps with individual masses and random relative velocities, the so-called individual dark clouds. However, the individual dark clouds are as well built up

by much more compact objects, the so-called dense cores, which are hosts of individual star formation (e.g. Myers & Benson, 1983).

Within the Milky Way, over 80 percent of the molecular hydrogen resides in giant cloud complexes which are the places where the supermassive O and B stars are formed. Due to their intense radiation and stellar winds, the survival time of a giant molecular cloud is typically some  $10^7$  yr. On average, the cloud converts about 3 percent of its mass into stars during this time. Given the total H II mass in the Galactic disc, it follows that the star formation rate from giant clouds is about  $2M_{\odot}\text{yr}^{-1}$ .

Cloud Type	$n_{\text{tot}}$ [ $\text{cm}^{-3}$ ]	$R$ [pc]	$T$ [K]	$M$ [ $M_{\odot}$ ]
Diffuse	500	3	50	50
Giant Molecular Clouds	100	50	15	$10^5$
Dark Clouds				
Complexes	500	10	10	$10^4$
Individual	$10^3$	2	10	30
Dense Cores / Bok Globules	$10^4$	0.1	10	10

Table 2.1.: Physical properties of molecular clouds.

### 2.2.2. Stellar Evolution

Dense cores harbour infrared point sources of emission which are the best hint for star formation occurring in these entities. The process itself is induced by the gravitational collapse of a core which forms a temporary configuration known as the *first core*. As its density climbs, the central lump quickly becomes opaque to its own infrared, cooling radiation. The total compressed mass is still small at this stage, about  $5 \times 10^{-2}M_{\odot}$ , but the radius is large by stellar standards, roughly 5 AU or  $200 R_{\odot}$ . With the addition of mass and shrinking of the radius, the internal temperature soon surpasses 2000 K. At this point, the rise in temperature is damped due to the absorption of most of the energy through the collisional dissociation of H II forming H I. This evolutionary phase ends as the entire configuration becomes unstable and collapses because pressure can not oppose compression any more due to the level off in temperature (e.g. Larson, 1973; Terebey *et al.*, 1984; André *et al.*, 2008).

The evolutionary stage following the collapse of the first core is designated as a *protostar*. It is the first dynamically stable configuration. With a radius of several  $R_{\odot}$ , a protostar of

$0.1 M_{\odot}$  has a mean internal temperature above  $10^5$  K. Objects in this phase are observable as bright infrared point sources in molecular clouds. As opposed to real stellar bodies the emitted radiation stems not directly from their surface but from an obscuring dust envelope still surrounding the central object, which serves as well as a reservoir for massive accretion. It is therefore conventional to define a protostar as a mass-gaining star whose luminosity stems mainly from external accretion, known as the *main accretion phase*. The ignition of nuclear fusion in terms of deuterium ( $^2\text{H}$ ) burning begins when the quasi-static contraction of the protostellar core pushes the temperature near  $10^6$  K (e.g. Shu *et al.*, 1987; Lada, 1987).

Although the main accretion phase of a protostar involves dynamical motion, the protostar itself is always in a state of hydrostatic equilibrium. With the end of infall, the further evolution of the star, now of fixed mass, is driven almost entirely by radiation from its surface layers. With this transition the star enters the *pre-main-sequence* phase and becomes optically visible. In this stage, for the first time nuclear fusion and self-gravity become the only sources of energy. The radiation from the stellar surface transports this internal energy directly into space, not hindered by surrounding dust. The loss in heat causes the star to shrink and releases gravitational binding energy. According to the virial theorem, this energy is equally partitioned to increase the thermal energy and compensate the loss through radiation. Hence, the cooling of a star results in a *rise* of the internal temperature. A pre-main-sequence star is therefore an object with negative heat capacity. The onset of nuclear fusion is generally correlated with the formation of a strong stellar wind, usually along the axis of rotation. Thus, many young stars have a bipolar outflow, a flow of gas out of the poles of the star. A stellar object that belongs to one of the former classifications is generally termed *Young Stellar Object*, or shortly *YSO* (e.g. Adams *et al.*, 1987; Andre & Montmerle, 1994).

Further contraction of an YSO finally leads to central temperatures reaching  $10^7$  K where fusion of hydrogen is enabled. As the burning increases, the nuclear energy released can balance the surface loss through radiation and the object's radius stabilises. At this point the star has reached the *zero-age main-sequence (ZAMS)* and will stay there until a significant amount of its fuel is destroyed (Iben, 1965).

This scenario is only valid for objects more massive than  $0.08 M_{\odot}$ . Falling under this limit, contraction for such low masses causes densities high enough for electron pressure degeneracy which makes the internal temperature fall below the value required for hydrogen ignition. Such substellar objects are designated as *brown dwarfs* (see the review by Liebert & Probst, 1987).

Observationally, two general classes of pre-main-sequence stars are distinguished, *T Tauri* and *Herbig Ae/Be* stars. The former is named for the prototypical object discovered in the Taurus-Auriga dark cloud complex and represents pre-main-sequence stars with masses lower than approximately  $1-2 M_{\odot}$ , the latter contains the more massive objects which are, in terms

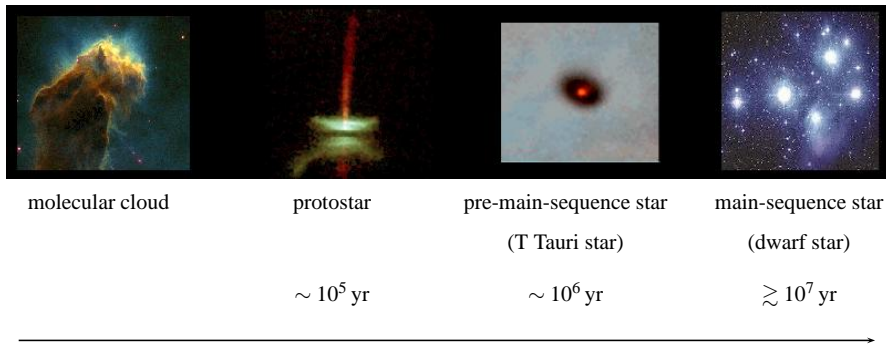


Figure 2.1.: The formation process of a solar-type star illustrated by images from NASA/HST.

of spectroscopy, A and B stars with emission lines. Herbig Ae/Be stars are usually observed only in giant clouds like Orion (Palla, 2005).

There is still some debate about how massive stars form. The reason to consider different formation scenarios for massive stars is due to the enormous energy output of massive stars. It is still rather unclear whether the radiation pressure is too large to build up the stellar mass by isolated accretion onto a core (see the review by Zinnecker & Yorke, 2007). This scaled-up version of the low-mass star formation is confronted with theories of “competitive accretion” in a protocluster environment and stellar collisions and mergers in very dense systems (Bonnell *et al.*, 2001a; McKee & Tan, 2003; Bonnell & Bate, 2005). Evidence in support of the core model of massive star formation includes the fact that massive starless cores are observed and the mass function of these cores is similar to the stellar initial mass function (IMF) (Beuther & Schilke, 2004; Reid & Wilson, 2006). Massive cores tend to have line widths that are much broader than thermal (Caselli & Myers, 1995), indicating that other forms of pressure support such as turbulent motions and magnetic fields are important.

### 2.2.3. Circumstellar Discs

#### Formation of Protoplanetary Discs

In the stellar evolution from protostars to pre-main-sequence objects accretion of matter plays a vital role. The general understanding of the accretion process is that due to the rotation of the parent cloud and the harboured protostar the infall is not spherically symmetric but the matter forms a disc geometry before it is transported to the stellar surface. The main issue here is that as the specific angular momentum of a cell of matter is sufficiently large, it inevitably veers away from the geometrical centre of the cloud during infall while still spinning up due to angular momentum conservation. Any such element enters a parabolic orbit, misses the

stellar surface and accumulates in an annulus around the central object. This phase marks the formation of a *protostellar disc* (see Saigo *et al.*, 2008).

With progressing time an increasing portion of the collapsing gas misses the star and contributes at first to the growth of the disc radius but not its mass. This is due to the equatorial symmetry of the accretion process. Any trajectory that misses the star has its counterpart with a negative velocity component perpendicular to the equatorial plane. Two opposing streams collide at supersonic speed and cause an accretion shock which deflects this portion of matter toward the protostar. The transport of matter through these streamlines directly onto the star works well for low disc surface densities but once the disc grows beyond a critical radius, the outermost particles can no longer penetrate to the stellar surface. The streamlines miss the central protostar as a consequence of the disc's buildup of angular momentum and converge to form a dense ring, which diminishes the mass transport onto the protostar. Consequently, the disc mass and density begins to rise which again causes a decreasing infall onto the stellar surface. Finally, all accreted matter from the cloud contributes to the disc's mass, which now climbs nearly linearly with time (e.g. Stahler *et al.*, 1986).

If this process would continue unabated, the mass of the disc would soon exceed that of the protostar. However, observations show that pre-main-sequence stars always have discs with relatively low masses, typically a few percent of the stellar mass. To avoid the rapid buildup of a massive disc, some process stronger than the drag from infall must allow material to spiral continually onto the protostar. The simplest way to achieve this is by *internal torquing*. Considering two neighbouring annuli, the inner annulus could lose angular momentum due to a torque exerted by the outer one through some kind of friction. The shrinking of the inner annulus would then be accompanied by a spreading of the disc. This simple model presents a very effective method for mass and angular momentum transport but a generally accepted physical source of the internal friction has still not been found (e.g. Larson, 1984).

Once the parent cloud of the protostar has vanished, accretion onto the disc stops and this marks the subsequent evolution of a *protoplanetary disc*. In this phase the formation of planets is thought to occur. The interactions of these young stellar objects in a cluster environment are in the focus of the present work.

### **Observational Detection and Geometry**

Circumstellar discs can be detected by emission throughout different wavelength regimes. Magnetic activity associated with the host pre-main-sequence (PMS) stars, plasma production from magnetic star-disc-jet interactions, and probably accretion shocks in the disc surface produce X-rays when two opposing streams of matter collide at supersonic speed (Kastner *et al.*, 2005). Intense starlight can ionise gas like oxygen or sulphur which have strong emission lines in the optical (O'Dell *et al.*, 1993). Optically-thick dust heated to some 100 K close

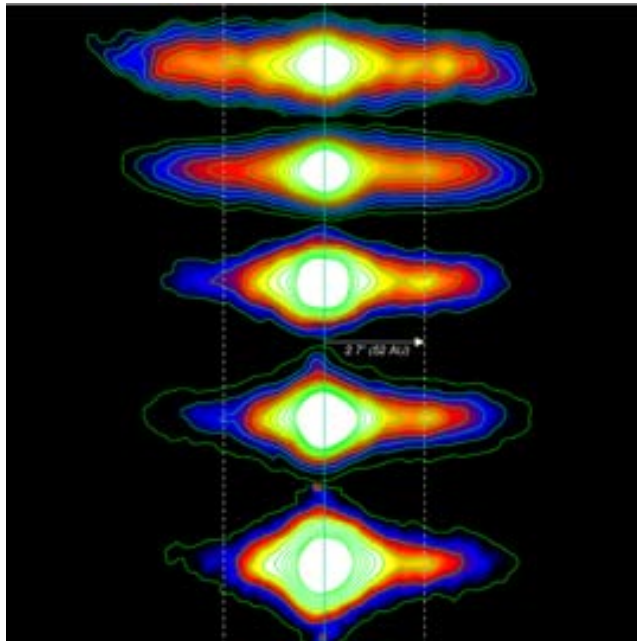


Figure 2.2.: Multiwavelength mid-IR imaging of the disc of Beta Pictoris. From top to bottom images from longer to shorter wavelengths are presented. Courtesy Gemini Observatory / AURA.

to the star emits preferentially in the infrared (IR) and with lower temperatures in the outer parts in the (sub-) millimetre regime. Fig. 2.2 shows how the disc size varies with observing wavelength. Because the cool outer parts of discs represent the vast majority of their mass and volume and most of the emission is optically thin, the submillimetre luminosity is a diagnostic of the total disc mass (Beckwith *et al.*, 1990). Finally, radio observations can provide information on the gas mass from continuum measurements or the velocity structure of the disc from characteristic molecular lines, typically CO or CS (Cabrit *et al.*, 2006).

While the X-ray activity of a PMS star is not yet sufficiently understood to derive properties of its circumstellar disc (Preibisch *et al.*, 2005), there has been large progress in the lower frequency bands. The first optical images of a young stellar disc were obtained by the Hubble Space Telescope (HST) of the star Beta Pictoris in the early 1980s (Smith & Terrile, 1984) and very soon more such systems were detected, giving rise to some spectacular images of star-disc systems in the Orion Nebula Cluster (McCaughrean & O'Dell, 1996). The challenge in optical imaging is the need for high resolution in order to distinguish the disc from the much more luminous stellar component. Thus only close-by star forming regions can be surveyed for discs by direct imaging. In cases where the two components are not well separated, the infrared or millimetre regimes are more advantageous because disc emission

at these wavelengths constitutes a significant fraction of the stellar radiation. This makes it comfortable to identify stars that are surrounded by discs by their *excess* in the observed wavelength band in comparison to pure photospheric stellar emission.

The favourite observation in the near-infrared (NIR) involves the standard broad band filters *J*, *H*, *K*, and *L* with central wavelengths at 1.25, 1.65, 2.2, and 3.5  $\mu\text{m}$ . NIR colour-colour diagrams (e.g. a plot of  $\text{mag}_J - \text{mag}_H$  vs.  $\text{mag}_H - \text{mag}_K$ ) are then used as a tool for investigating the physical natures of YSOs in young clusters. Objects lying in the infrared excess region of these diagrams are considered to be sources with candidate circumstellar discs (e.g. Haisch *et al.*, 2000; Lada *et al.*, 2004; Oliveira *et al.*, 2004). Identification problems can arise from contamination by extended emission in H II regions, reflection nebulosity, stellar photospheric emission, and source crowding in high-density regions. Such effects could lead to artificially high or low disc fractions. Furthermore, the magnitude of the NIR excess from a disc also depends on the parameters of the star/disc system (e.g., stellar mass/age, disc inclination, accretion rate, and inner disc hole size) (Adams *et al.*, 1987; Meyer *et al.*, 1997; Hillenbrand *et al.*, 1998). Since these effects are the more severe the shorter the wavelength used for observations, and the magnitude of the infrared excess produced by a circumstellar disc increases rapidly with wavelength, longer infrared wavelengths are preferable. However, because the stellar energy distribution of a typical late type star peaks near the *L*-band wavelength, *L*-band observations are far superior to mid-infrared observations (i.e.,  $\geq 10 \mu\text{m}$ ) to detect relatively faint low mass stars. Therefore combining NIR *JHK* observations with *L*-band data is a powerful method for investigating the nature of young stellar sources (Haisch *et al.*, 2000).

Additionally, properties of the inner disc can be derived from radiation driven by accretion. Accretion onto the host star is usually identified from strong H $\alpha$  emission. The presence of an inner disc appears to correlate with the presence or absence of spectroscopic signatures of active accretion onto the star (Hartigan *et al.*, 1995). However, accretion signatures and IR excess are not strictly correlated. Currie *et al.* (2007) find that while accretion may imply IR excess, IR excess need not imply accretion.

One should be aware that observations of the excess in a certain frequency band only trace circumstellar dust of the corresponding size and temperature, thus at each frequency band only a small annular portion of the disc is investigated due to the decreasing temperature with increasing distance from the central star. Sensitivity to grain size depends on wavelength and each regime provides information on grains within approximately a range of 0.1-10 times the wavelength (Meyer *et al.*, 2006). Observations in the NIR bands *J*, *H*, *K*, and *L* trace disc material typically at distances  $\lesssim 0.1$  AU of the central star (Haisch *et al.*, 2005).

Surveys at far-infrared ( $> 30 \mu\text{m}$ ) and submillimetre wavelengths trace the coolest dust at large radii. Often, this emission is optically thin and is therefore a good tracer of the total

dust mass at radii  $> 10$  AU (Meyer *et al.*, 2006). However, the flux from disc material at this wavelengths is typically rather low and provides often only upper limits on the disc mass. Our own solar system cold dust mass would be undetectable in submillimetre surveys. Thus it is still difficult to assess statistically the properties of cold discs (Meyer *et al.*, 2006). Using the increased resolution and sensitivity of the SMA interferometer, Andrews & Williams (2007) observed photoevaporating discs in the ONC and provided the first estimates of their masses, which turned out to be similar to discs in the comparatively quiescent Taurus region (Williams *et al.*, 2005). They further determined the distribution of disc masses in Taurus-Auriga over  $\sim 3$  orders of magnitude and found that the median disc is 0.5% as massive as the central star, with a typical mass of  $0.005 M_{\odot}$  (Andrews & Williams, 2007).

Using the information from multiple wavelengths, YSOs can be characterised by their spectral energy distributions (SEDs) (Adams *et al.*, 1987; Lada, 1987). Based on the SED, four main types of YSOs are distinguished: class 0, I, II, III. The class 0/I objects are deeply embedded and their SEDs peak in the submillimeter or the far infrared indicating that the source of the emission is cold dust. The class II sources are optically visible stars with infrared excess emission that is attributed to a disc surrounding the central object. Class III sources have almost no infrared excess and their photometric properties are very similar to normal main-sequence stars. Mid-infrared two-colour diagrams can be used to distinguish between class I, II and III objects (Balog *et al.*, 2007a).

Information about a disc's geometry can be only inferred either directly from optical images or indirectly using velocity information in the submillimetre to radio wavelengths from molecular lines.

### Evolution of Protoplanetary Discs

Nearly all stars are thought to be born with circumstellar discs (Hillenbrand *et al.*, 1998). About 20-30% of stars aged  $\sim 1$  Myr appear to possess circumstellar discs with masses greater than  $\sim 0.01 M_{\odot}$ , comparable to the minimum mass of the presolar nebula (Weiden-schilling, 1977; Anthony-Twarog, 1982), and the median disc mass is  $\lesssim 0.004 M_{\odot}$  (Eisner & Carpenter, 2003). Recent work based on NIR excess data has shown that these discs dissipate on time scales of order 3 Myr (Haisch *et al.*, 2001). However, the data also suggests a dispersion of inner disc lifetimes from 3-10 Myr (Meyer *et al.*, 2006), as shown in Fig. 2.3. The same picture is evident from accretion signatures. The typical mass accretion rates onto the star are  $\sim 10^{-8} M_{\odot} \text{ yr}^{-1}$  for  $\sim 1$  Myr old T Tauri stars (Hartmann *et al.*, 1998). After  $\sim 5$  Myr, fewer sources show strong  $H\alpha$  emission indicative of accretion, and accretion rates are typically much lower ( $\sim 10^{-9} M_{\odot} \text{ yr}^{-1}$ ) than at earlier ages. By  $\sim 10$  Myr, few sources show signs of active accretion (Sicilia-Aguilar *et al.*, 2005a). Muzerolle *et al.* (2000) found that two members of the 8-10 Myr old TWA – TW Hya and Hen 3-600A – are experiencing ongo-

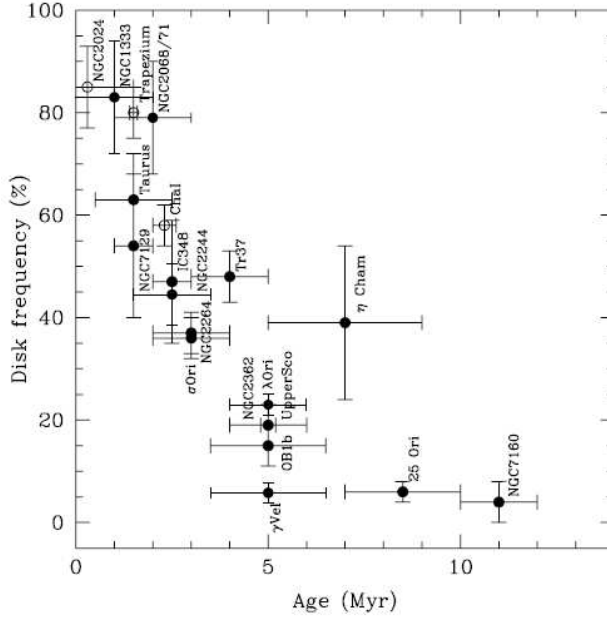


Figure 2.3.: Fraction of stars with near-infrared disc emission as a function of the age of the stellar group from Hernández *et al.* (2008). Open circles represent the disc frequency for stars in the T Tauri (TTS) mass range ( $\sim K5$  or later), derived using *JHKL* observations: NGC 2024 and Trapezium (Haisch *et al.*, 2001), and Chamaeleon I (Gómez & Kenyon, 2001). Solid symbols represent the disc frequency calculated for stars in the TTS mass range using Spitzer data (see text of Hernández *et al.* (2008) for references).

ing disc accretion, albeit at rates of a few orders of magnitude lower than 1-Myr-old T Tauri stars. The same authors derived the accretion rate for the TWA member ECHA J0843.3-7905 which implies a minimum disc mass  $\dot{M}t = 0.01 M_{\odot}$ , a value comparable to that of younger PMS stars, though for some other accreting stars in TWA it is 20 times lower.

Currie *et al.* (2007) state that the population of accreting sources is strongly spectral type dependent. The existence of accreting pre-main-sequence stars in  $\eta$  and  $\chi$  Persei implies that circumstellar gas in some systems, especially those of spectral type G5 or later, can last longer than 10-15 Myr.

The detection of inner discs and of ongoing disc accretion in objects with ages  $\gtrsim 10$  Myr appears to be in conflict with a common disc lifetime of  $< 6$  Myr as derived by Haisch *et al.* (2001). The issue is discussed by Lyo *et al.* (2003) and they argue that the limiting sensitivity of the NIR studies masks the detection of inner discs in many PMS stars, emphasising that the disc lifetime derived by Haisch *et al.* (2001) relies heavily on the distant ( $d = 1.5$  kpc) cluster NGC 2362 for which the presence of discs in the low-mass ( $M < 1 M_{\odot}$ ) population is

unknown. Low-mass stars are disc rich in the  $\eta$  Cha cluster, with 7/11 low-mass members showing IR-excess in the  $L$ -band. Undoubtedly the inner disc fraction declines with stellar age, but the study of the TWA and the  $\eta$  Cha cluster suggests that a significant fraction of PMS stars may retain their inner discs for 10 Myr (Lawson *et al.*, 2004).

Though most disc surveys are focused on the detection of dust, observations of the disc accretion is essential because gas dominates the mass of primordial discs and is the building material of giant planets. Classical T Tauri stars with excess emission from the near-IR through the submillimetre are gas rich discs with some evidence for Keplerian support (Meyer *et al.*, 2006).

The transition from optically thick to optically thin emission is an important tracer of the evolution of protoplanetary discs, indicating growth of dust grains which can lead to the formation of planetesimals. Young stars (with ages  $< 3$  Myr) lacking optically-thick near-infrared excess emission but possessing optically-thick mid-infrared emission are rare (Skrutskie *et al.*, 1990). This suggests that the transition time between optically-thick and thin from  $< 0.1$  AU to  $> 3$  AU is rapid,  $\ll 1$  Myr (Wolk & Walter, 1996; Kenyon & Hartmann, 1995; Simon & Prato, 1995).

The general picture is that primordial accretion discs commonly surround very young stars (approaching 100%), and that gas-rich discs around more (less) massive stars are bigger (smaller), but last shorter (longer). Because of the higher surface density of solids in the disc, more massive discs surrounding higher mass stars will probably form planetesimals faster (Meyer *et al.*, 2006).

However, observations of protoplanetary discs at different wavelengths seem to restrict the time scale for planet formation significantly. This evolution is very complex and not well understood, thus there exists no consistent model so far which could follow the entire formation process from the admixture of gas and dust to a complete planetary body. However, two main physical concepts are competing to explain planet formation: gravitational instabilities and coagulation. A major reason why gravitational instabilities have not been strongly advocated for T Tauri discs is that disc masses seem to be too low. Disc masses need to be of the order of 0.1 of the stellar mass for gravitational instabilities to operate (Pringle, 1981), while typical T Tauri disc mass estimates have been of the order of  $0.01 M_{\odot}$ , roughly a minimum-mass solar nebula. A very recent comprehensive survey of the Taurus star-forming region suggests a median disc mass of  $5 \times 10^{-3} M_{\odot}$  (Andrews & Williams, 2005), albeit with a large scatter. This median mass estimate is an order of magnitude lower than what is required for gravitational instability, though estimates for a small number of objects are much closer to the limiting value (Hartmann *et al.*, 2006). Recent studies of Herbig Ae/Be stars, T Tauri stars, and brown dwarfs suggest that the grains in the surface layers of the discs around these objects have undergone significant thermal processing and have grown well beyond typical

sizes in the interstellar medium (Przygodda *et al.*, 2003; van Boekel *et al.*, 2003; Kessler-Silacci *et al.*, 2005; Apai *et al.*, 2005), suggesting that the initial phases of planet formation could be under way in these objects and thus favouring the coagulation hypothesis (Shuping *et al.*, 2006).

Recent work has shown that even optically-thin mid-infrared emission (tracing material between 0.3-3 AU) is rare around sun-like stars with ages 10-30 Myr (Mamajek *et al.*, 2004; Weinberger *et al.*, 2004; Silverstone *et al.*, 2006). It appears that circumstellar disc material between 0.1-1 AU typically drops below detectable levels on time scales comparable to the cessation of accretion. These levels are probably below what our solar system might have looked like at comparable ages (3-30 Myr).

It is important to distinguish between surveys for primordial discs, gas and dust rich discs left over from the star formation process, and debris discs, where the opacity is dominated by grains released through collisions of larger parent bodies. Often this distinction is based on whether remnant gas is left in the system. With a gas to dust ratio  $> 1$ , dust dynamics are influenced by their interaction with the gas (Takeuchi & Artymowicz, 2001). In the absence of gas, one can argue based on the short dust lifetimes that observed dust has been likely recently generated through collisions in a planetesimal belt (Jura *et al.*, 1998).

Debris discs are found around stars generally older than  $\sim 10$  Myr, with no signs of gas accretion, as judged from the absence of emission lines or UV excess (Hillenbrand, 2005). In the absence of gas drag, a  $10 \mu\text{m}$  dust grain from the primordial, protoplanetary nebula cannot survive longer than  $\sim 1$  Myr within 10 AU of a star due to a number of clearing processes like sublimation, radiation pressure, Poynting-Robertson and stellar wind drag (Chen *et al.*, 2005). Therefore, any main sequence star older than 10 Myr with an infrared excess is a candidate to have circumstellar material supplied through debris disc processes (Gorlova *et al.*, 2006). Rieke *et al.* (2005) demonstrated both the overall decline of debris discs with age (first noted in Holland *et al.*, 1998; Spangler *et al.*, 2001) and the large scatter of disc properties at any given age (as previously noted in Decin *et al.*, 2003). By probing excesses to within 25 % of the photospheric emission, Rieke *et al.* (2005) found a surprising number of non-excess stars even at ages as young as 10-20 Myr, implying very rapid clearing of the inner 10-60 AU region in these systems.

In general, it is observed that the cold dust mass diminishes with time as expected from models of the collisional evolution of debris belts. However, at any one age there is a wide dispersion of disc masses. Whether this dispersion represents a range of initial conditions in disc mass, a range of possible evolutionary paths, or is evidence that many discs pass through short-lived phases of enhanced dust production is unclear (Meyer *et al.*, 2006).

It is interesting to note that extrapolations of the detection frequency of extra-solar planets as a function of radius beyond current survey limits suggest a frequency  $\sim 10$ -20 % of extra-

solar giant planets with masses  $> 1 M_{\text{JUP}}$  out to 20 AU, consistent with debris disc statistics for G stars (Meyer *et al.*, 2006). Combining data on A stars, G dwarfs, and M dwarfs, there is to date no evidence for wildly divergent evolutionary histories for debris discs as a function of stellar mass averaged over main sequence lifetimes. Moreover, preliminary results from the Spitzer Space Telescope suggest that debris disc evolution is not a strong function of multiplicity, and may even be enhanced in close binaries.

The main results can be summarised as follows: 1) Warm circumstellar material inside of 1 AU dissipates rapidly on time scales comparable to the cessation of accretion; 2) The gas content of discs much older than 10 Myr is incapable of forming giant planets; 3) While massive analogues to our asteroid belt lacking outer discs appear to be rare overall (1-3 %), warm discs (lacking inner hot dust) seem to enjoy a preferred epoch around stars with ages between 10-300 Myr old; 4) Cold outer discs (analogous to our own Kuiper Belt, but much more massive) are found around 10-20 % of sun-like stars. Yet in affecting these comparisons, one must remember that the current observational sensitivity is too low to observe tenuous debris discs comparable to our own asteroid belt or our Kuiper Belt (Meyer *et al.*, 2006).

The general picture of a protoplanetary disc is that of a thin disc consisting of gas and dust, with an inner hole and a smoothed outer edge (Mundy *et al.*, 2000). The inner hole is usually found to increase in size from  $< 0.1$  AU up to several AU in several Myr (e.g. Hughes *et al.*, 2007). The typical diameter is 200 AU for low- and intermediate-mass stars, though even discs larger than  $10^4$  AU surrounding massive stars have been observed. The disc mass is usually at most several percent that of the central star (McCaughrean & O'Dell, 1996; Andrews & Williams, 2007).

One should caution that since stars do not form in isolation disc evolution is affected by the environmental conditions of a star's hosting entity. In particular, massive stars are usually found in very massive and dense clusters that can potentially have a significant influence on the evolution of a massive star's disc. Moreover, the general picture of the disc of lower mass stars is obtained from observations of different environments that can vary considerably. The formation, evolution and properties of young star clusters is thus subject of the next section.

## 2.3. Cluster Formation

### 2.3.1. Formation and Evolution

Cluster formation is a fundamental part of star formation. Star clusters make a significant, perhaps dominant, contribution to the total star formation rate of galaxies (Lada & Lada, 2003; Fall *et al.*, 2005). The formation of stars throughout the Galaxy does not process randomly but is confined to a spatial and temporal structure. A strong association is found

between the location of clusters and of dense, massive molecular cloud cores (e.g. Lada *et al.*, 1991).

As described in the previous section, the birthplaces of stars are hierarchical complexes. The inner clumping is not only confined to space but occurs as well in time, so that formation of individual stars in a clump sets in nearly simultaneously. The essence of this process is the birth of stars in groups with a velocity distribution according to the Maxwell-Boltzmann distribution (Clarke *et al.*, 2000). Due to the different properties of their precursors, the molecular clouds, stellar groups show a great variety in densities and stellar composition. Cluster densities have a spread of  $\sim 10^2$  to a few  $10^6$  stars  $\text{pc}^{-3}$ , the latter value being found in massive clusters like NGC 3603 or the Arches Cluster. However, the sizes of young clusters (of ages less than a few  $10^6$  years) appear fairly uniform (with a half-mass radius in the range 0.2-0.8 pc) and, notably, are a factor of 5-10 times smaller than the typical sizes of Galactic open clusters (with ages of a few  $10^7$  to  $10^9$  years; Phelps & Janes, 1994; Janes *et al.*, 1988). With velocity dispersions of  $1-2 \text{ km s}^{-1}$ , smaller and less dense clusters can disperse quickly, possibly causing an overestimate of “typical” cluster membership numbers and projected densities (Clarke *et al.*, 2000).

Embedded, dense clusters typically have ages  $\lesssim 2$  Myr (Carpenter, 2000). This narrow age range has led Palla & Stahler (2000) to reanalyse published H-R diagrams for a number of nearby star-forming regions with a single set of pre-main-sequence models. They argue that star formation over entire molecular clouds (e.g., Taurus and Chamaeleon I) and individual clusters (e.g., the Orion Nebula Cluster) started at a low rate  $\gtrsim 10$  Myr ago and has increased dramatically within the past 1-3 Myr. In their scenario, molecular clouds remain relatively dormant for much of their cloud lifetime since individual dense cores are supported against gravitational collapse by magnetic fields, and the time scale to dissipate the magnetic support is on the order of  $\sim 10$  Myr (see also Palla & Galli, 1997).

This picture of a relatively isolated cluster formation is confronted by the concept of triggered star formation where the location of young stellar objects – and clusters – in the dense gas swept up by expanding H II regions lends credence to this scenario (Elmegreen & Lada, 1977). Observations of IC 1396 (Patel *et al.*, 1998), the Rosette Molecular Cloud (White *et al.*, 1997), IC 1805 (Heyer *et al.*, 1996), or Gem OB1 (Carpenter *et al.*, 1995) show clear examples of this mode of cluster formation. In other cases, however, the locations of young clusters give no hint of external triggering (e.g. Taurus, NGC 2264). Thus the key question whether cluster formation is induced or spontaneous remains unanswered at the present time.

Simulations of cluster dynamics are often undertaken in spherical geometry, motivated in part by the shapes of globular clusters in the Galaxy. It is however well known that some clusters are significantly flattened, the best studied examples being the globular clusters in the LMC (Clarke *et al.*, 2000). In the Galaxy, obvious examples of flattened young clusters

are the ONC, Mon R2, and NGC 2024, where isophotal fitting of the outer regions yields a projected axis ratio of about 1:2 (Hillenbrand & Hartmann, 1998; Carpenter *et al.*, 1997; Lada *et al.*, 1991). The relation between ‘initial’ and ‘final’ (i.e. relaxed) morphologies is set by the principle of adiabatic invariance, and yields the prediction that the initial geometry is substantially more flattened than that of the relaxed cluster. When applied to the LMC globulars, initially flattened geometries with a projected axis ratio of 1:5 are required (Clarke *et al.*, 2000).

Evidence for radial mass segregation has been seen in many open clusters (see Scalo, 1986, for a review). Besides dynamical origin, Lada *et al.* (1991) note a second mechanism that could produce mass segregation in clusters, namely the star-formation process itself. Stars form in molecular gas. If this gas is centrally concentrated, then more massive stars would tend to form in the centre of the gas condensation whereas lower mass stars could form throughout. Evidence that molecular cloud cores are centrally condensed has been presented in studies of a number of Bok globules (Snell, 1981; Arquilla & Goldsmith, 1985). However, as discussed by Bonnell *et al.* (1998), simple Jeans mass arguments do not lead to the expectation that the most massive stars should form in the centre of dense clusters. Since these regions have high densities, the associated Jeans mass is low, unless the local temperature is anomalously high. Evolutionary effects, involving accretion and protostellar collisions, are probably required to build up massive stars in cluster cores.

It is well known that the formation of a bound cluster requires a high fraction (30-50 %) of gas to be turned into stars before destructive feedback mechanisms from massive stars come into play (e.g. Lada *et al.*, 1984; Goodwin, 1997). In practice this means a high conversion efficiency within a few cluster dynamical times. The fate of a particular cluster in response to gas loss depends on the initial gas fraction, the removal time scale and the stellar velocity dispersion when the gas is dispersed (Lada *et al.*, 1984; Pinto, 1987; Verschueren & David, 1989; Goodwin, 1997). If the gas comprises a significant fraction of the total mass ( $\gtrsim 50\%$ ) and is removed quickly compared to the cluster crossing time, then the dramatic reduction in the binding energy, without affecting the stellar kinetic energy, results in an unbound cluster. Alternatively, if the gas is removed over several crossing times, then the cluster can adapt to the new potential and can survive with a significant fraction of its initial stars (see Goodwin, 1997; Kroupa *et al.*, 2001; Boily & Kroupa, 2003). For example, clusters with gas fractions as high as 80 % can survive with approximately half of the stars if the gas removal occurs over 4 or more crossing times (Lada *et al.*, 1984).

The results of unbiased surveys of star forming regions suggest that the fraction of star formation taking place in clusters varies quite strongly from place to place. Although it is not clear why this is the case, all of the regions surveyed thus far seem to support a basic picture in which the majority of star formation at all masses takes place in clusters (Lada, 1992; Lada

& Lada, 2003). An even higher incidence of clustering appears in the surveys of regions containing massive stars. The near-infrared surveys of Herbig Ae/Be stars by Hillenbrand (1995) and Testi *et al.* (1997, 1998) indicate that clusters are present around those Ae/Be stars with masses in excess of  $3\text{-}5 M_{\odot}$ , with little evidence of clustering around less massive objects. All locally-observed massive stars appear to form in star clusters (de Wit *et al.*, 2005), particularly in rich star clusters (Massi *et al.*, 2006).

One possible correlation in the data is that between stellar density and the mass of the most massive cluster member (Hillenbrand, 1995; Testi *et al.*, 1998). Since clusters exhibit a rather small range of projected radii (see Table 1 and Fig. 1 in Testi *et al.*, 1998) this also translates into a correlation between the number of cluster stars and the mass of the most massive star. It is at present unclear whether this correlation represents a genuine physical requirement of a high density or a large number of stars for massive star formation (e.g. Bonnell *et al.*, 1998), or whether it is merely a consequence of random drawing from a canonical initial mass function (IMF), which would imply that a given cluster is more likely to contain a massive star if it has a large stellar population. However, Weidner & Kroupa (2006) find that the mass of the most massive star in a cluster correlates non-trivially with the cluster mass.

Mini-clusters comprising  $N$  members dissolve due to point mass gravitational interactions on a time scale that is a strong positive function of  $N$  (van Albada, 1968; Heggie, 1974). Thus point mass gravitational effects are the main agent of dissolution for small  $N$ -body systems, where a central binary can interact and eject the majority of stars, whereas gas expulsion may predominate in larger stellar systems. Therefore, compact small clusters are short-lived even if gas expulsion is neglected: for example, a cluster of 10 stars in a volume of radius 0.1 pc dissolves in less than a million years. This fact underlines the difficulty of assessing the level of sub-clustering at birth in star forming regions, inasmuch as information on the smallest scales is rapidly erased, sometimes before the cluster becomes optically visible.

In summary, then, a number of physical processes occurring in very compact mini-clusters can profoundly affect the properties of the stars and their associated discs. It is also becoming increasingly apparent, given the high stellar densities measured in young clusters and therefore the possible role of encounters, that whether a star forms in a cluster or in isolation may be important in determining its fundamental properties, such as its mass, binarity or possession of planets (Clarke *et al.*, 2000).

The effect on star formation in an environment dominated by high mass stars is still an unresolved problem of astrophysics (Balog *et al.*, 2007a). Strong stellar winds from high mass O- and B-type stars can trigger star formation by compressing the interstellar material, which eventually becomes gravitationally unstable (Elmegreen & Lada, 1977). Also photoevaporation can heat the surface of an interstellar cloud and lead to a radiatively driven implosion, thus playing a similarly (if not more) important role in triggering star formation in this envi-

ronment (Adams *et al.*, 2004). On the other hand, the strong extreme ultraviolet (EUV) and far ultraviolet (FUV) radiation from the same hot stars might so vigorously photoevaporate the material around the forming stars that it truncates the star formation process (Balog *et al.*, 2007a).

Furthermore, planetesimal formation by means of gravitational instability may in fact be enhanced by the photoevaporation of the disc surface layers (Throop & Bally, 2005), leading to the somewhat paradoxical conclusion that planet formation around low-mass stars may in fact be more efficient in the harsh environments of high-mass clusters (Shuping *et al.*, 2006).

Recent meteoritic studies suggest that primitive solar system materials were subject to intense UV irradiation (Lyons & Young, 2005) and that the whole protoplanetary disc may have been polluted by the ejecta from a nearby supernova explosion (Tachibana & Huss, 2003; Hester *et al.*, 2004) – both suggesting that our own solar system may have formed in a region similar to Orion (Shuping *et al.*, 2006).

Similarly, the evolution of debris discs can be influenced by the stellar environment. To initiate a collisional cascade the velocity dispersion in the disc must be excited to allow collisions to be catastrophic. Models which follow the collisional evolution of planetesimal belts from the growth phase to the cascade phase show that the transition may occur after the formation of a planet sized object (Kenyon & Bromley, 2002b, 2004) or due to the excitation by a passing star (Kenyon & Bromley, 2002a).

Balog *et al.* (2007a) find from observations of NGC 2244, a young, nearby open cluster containing 7 O and 65 B stars, that in the central region of 0.5 pc radius, containing all the O stars, the disc ratio is about 27%. In the remaining region the disc ratio is about 45%, similar to the overall disc fraction in the cluster of 44%. They conclude that the effect of high mass stars on the disc fraction is significant only in their immediate vicinity (< 0.5 pc). Though the authors attribute the destructive effect on the protoplanetary discs to photoevaporation by the massive stars, also gravitational interactions could lead to such a feature, as will be shown later.

Any event which causes a loss of disc mass can act destructive on the process of planet formation. One such scenario could be strong gravitational perturbations by stellar encounters during the pre-main-sequence phase. Hence the probability of the formation of planetary systems is directly affected by the results of the present investigation.

### 2.3.2. Classification

Young stellar groups build a classification sequence characterised by the mass of their earliest-type stars. It stretches from the OB associations (O stars, e.g. ONC) through R associations (B stars, e.g. Mon R2), to T associations such as Taurus-Auriga in the Taurus dark cloud which contain only low-mass stars.

### T Associations

Cloud complexes of lower mass, classified as dark cloud complexes in Table 2.1, produce entities designated as *T associations*. They contain only low-mass stars which are still in the pre-main-sequence evolutionary stage, already introduced as T Tauri stars. A T association is only loosely bound and as its members evolve towards main-sequence objects, even the weak stellar winds and molecular outflows can remove great portions of the cloud's material before it can contract significantly. This stops the inward motion and expansion reduces the stellar density until the whole population disperses into the field. The ageing pre-main-sequence stars are mingled observationally with the general field and become hard to identify. A famous example for an T association is the Taurus-Auriga complex (Strom *et al.*, 1975).

### R Associations and Open Clusters

If a complex has a somewhat higher mass and density, also a population of intermediate-mass stars will be produced. Such *R associations* show the conspicuous *reflection nebulae*. That is, the contraction times of intermediate pre-main-sequence stars are short enough that they become visible in the optical while molecular gas resides in their proximity. This matter is illuminated by the intense stellar radiation and eventually scatters the photons back into the observers direction. Due to their fraction of more massive Herbig Ae/Be members R associations may form bound entities that last much longer than the contraction phase of the T Tauri stars inside. Such *open clusters* consist of ZAMS stars and are completely depleted of gas. They can exceed ages of several  $10^8$  yr until they are destroyed by tidal disruption in encounters with giant molecular clouds. A prototype of an R Association is Mon R2 (Herbst & Racine, 1976).

### OB Associations and Rich Star Clusters

The cloud fragments that give rise to high-mass stars are still rarely found. One possible scenario is that high-mass stars arise from the coalescence of previously formed cluster members. The clue to this missing link may as well be the fact that new born O and B stars are removing their dust envelopes on time scales too short to be observed. However, it is significant that massive stars have the tendency to cluster and are often found in loose collections of a few dozen members, designated as *OB associations* (Elmegreen & Lada, 1977). Furthermore, every Galactic OB association thus far observed is closely associated with a giant molecular cloud while dark cloud complexes do not produce OB associations. Even more significant, rich clusters with stellar densities exceeding  $10^3 \text{ pc}^{-3}$  only appear around O or B stars strongly concentrated in the cluster core (Massi *et al.*, 2006). Thus one may conclude that each such system must result from the contraction of a very massive cloud clump. Here

self-gravity has the strongest influence and the contraction quickly accelerates. But this circumstance can lead also, somewhat paradoxically, to expanding OB associations, the large internal velocities of which can be often observed. The reason is the fast expulsion of the molecular material in which the stellar group is embedded. Massive winds and intense radiation heats the surrounding material and blows it away, removing in this way a significant portion of matter and thus reducing the gravitational potential. The survival time of a giant molecular cloud is typically some  $10^7$  yr (Strom *et al.*, 1975).

From this point of view, the possible fate of a group containing massive stars depends on accurate observations of the stars' velocity dispersion. In any case, the dispersal of gas from the parent cloud seems to be the determining process for cluster dynamics (e.g. Kroupa *et al.*, 2001). One of the most conspicuous nearby site of massive star formation is the complex in Orion.

## 2.4. The Initial Mass Function (IMF)

To understand the evolutionary process of star clusters, one has to know the initial conditions when they were formed. Here the initial distribution of stellar masses, the *Initial Mass Function (IMF)*, is one of the key parameters determining the dynamical evolution and composition of a cluster population. It is common to investigate the IMF in five characteristic mass regimes: brown dwarfs (BDs) ( $< 0.08 M_{\odot}$ ), very-low-mass stars ( $0.08$  to  $0.5 M_{\odot}$ ), low-mass stars ( $0.5$  to  $1 M_{\odot}$ ), intermediate-mass stars ( $1$  to  $8 M_{\odot}$ ), and massive stars ( $m > 8 M_{\odot}$ ) (Kroupa, 2002).

The IMF is analytically represented by a mass function  $\xi(m)$  that describes the number of stars  $dN$  in a mass interval  $dm$ , or equivalently by the corresponding logarithmic mass function  $\xi_L(m)$ ,

$$dN = \xi(m)dm = \xi_L(m)d\log_{10}m, \quad (2.11)$$

which leads to the relation

$$\xi_L(m) = (m \ln 10)\xi(m). \quad (2.12)$$

The slope of the mass function in a given mass interval is the key parameter that reflects the relative abundance of stars of the corresponding spectral types. The slope is defined by

$$\alpha(m) \equiv -\frac{d}{d\log_{10}m}(\log_{10}\xi(m)) \quad (2.13)$$

or

$$\Gamma(m) \equiv \frac{d}{d\log_{10}m}(\log_{10}\xi_L(m)). \quad (2.14)$$

From (2.12), (2.13), and (2.14) one obtains easily the relation

$$\Gamma = 1 - \alpha. \quad (2.15)$$

Historically a consistent analysis of the stellar mass distribution began in 1955 at the Australian National University, when E. Salpeter published the first estimate of the IMF for stars in the solar-neighbourhood (Salpeter, 1955). For stars with masses in the range  $0.4$  to  $10 M_{\odot}$ , he found that it can be described by a power-law form with an index  $\alpha = 2.35$ . Massey (1998) demonstrated through spectroscopic classification that Salpeter’s original result extends up to the most massive stars known to exist with  $m \gtrsim 120 M_{\odot}$ .

Investigations of the IMF aim at one of the most fundamental questions of star formation, namely whether the functional form of the IMF is dependent on the local characteristics of a star-forming environment, or if it is universal, unchanging between different regions (Liu *et al.*, 2003). Meyer *et al.* (2000) state that the near-IR study of the Trapezium by Luhman *et al.* (2000), as well as studies of NGC 2024, including those by Comeron *et al.* (1996) and Meyer (1996), along with studies of other star-forming regions, have shown evidence that the IMF is universal, unchanging regardless of local environmental conditions. However, Scalo (1998) cautions that there is strong evidence for IMF variations, and these variations do not seem to depend systematically on physical variables such as metallicity or stellar density. A conclusive difference has not been found as well between the IMF in Taurus-Auriga (Kenyon & Hartmann, 1995; Briceño *et al.*, 2002) and  $\rho$  Oph (Luhman & Rieke, 1999) on the one hand, and the ONC (Hillenbrand & Carpenter, 2000; Palla & Stahler, 1999; Muench *et al.*, 2000) on the other.

Deriving the IMF from observational data deals with many difficulties and biases. The field star IMF around  $m \approx 1 M_{\odot}$  is hopelessly entangled with the galactic star formation history, which shows a peak around 6-8 Gyr ago. Thus the IMF in the mass range  $0.85$  to  $1.3 M_{\odot}$  can only be estimated from open cluster IMFs (Scalo, 1998). The “cleanest” place for estimating the IMF is the  $1$ - $15 M_{\odot}$  range in star clusters. There are cluster-specific uncertainties which partly compensate for these advantages. Since nearly all findings of radial mass segregation find higher-mass stars more concentrated than lower-mass stars (see Section 2.3.1), this effect means that the true IMF may be steeper than the derived IMF, i.e. derived values of  $\Gamma$  must be considered as upper limits (Scalo, 1998).

Studying the distribution of massive stars is complicated because they have short main-sequence lifetimes (Massey, 1998) and mass estimates from the luminosity are uncertain by up to 50% (Massey *et al.*, 2002), a source of error also not yet taken into account in the derivations of the IMF (Weidner & Kroupa, 2006). For example, a  $85 M_{\odot}$  star cannot be distinguished from a  $40 M_{\odot}$  star on the basis of its magnitude alone. Furthermore, observations have shown that most massive stars are in binary and higher-order multiple systems

(Duchêne *et al.*, 2001; Preibisch *et al.*, 1999). Correcting for the missed companions leads to systematically steeper slopes (Sagar & Richtler, 1991).

Moreover, it has been shown that the derived IMF is extremely sensitive to different types of data and analysis methods (Scalo, 1998).

Nevertheless, the distribution of stars in young clusters seems to be fairly well described by a IMF that is represented by a multiple power-law function (Kroupa *et al.*, 1993; Kroupa, 2001),

$$\xi(m) = k \begin{cases} \left(\frac{m}{m_1}\right)^{-\alpha_0} & , m_0 < m \leq m_1 \\ \left(\frac{m}{m_1}\right)^{-\alpha_1} & , m_1 < m \leq m_2 \\ \left[\prod_{i=2}^{n \geq 2} \left(\frac{m_i}{m_{i-1}}\right)^{-\alpha_{i-1}}\right] \left(\frac{m}{m_n}\right)^{-\alpha_n} & , m_n < m \leq m_{n+1} \end{cases} \quad (2.16)$$

where  $k$  is a normalisation factor and has the value  $k = 0.877 \pm 0.045 \text{ stars pc}^{-3} \text{ M}_\odot^{-1}$  for scaling to the solar neighbourhood (Weidner & Kroupa, 2006). The slopes derived by Kroupa (2001) are

$$\begin{aligned} \alpha_0 &= +0.3 \pm 0.7 & 0.01 \leq m/\text{M}_\odot < 0.08, \\ \alpha_1 &= +1.3 \pm 0.5 & 0.08 \leq m/\text{M}_\odot < 0.50, \\ \alpha_2 &= +2.3 \pm 0.3 & 0.50 \leq m/\text{M}_\odot < 1.00, \\ \alpha_3 &= +2.3(+0.4) \pm 0.7 & 1.00 \leq m/\text{M}_\odot, \end{aligned} \quad (2.17)$$

where the value in brackets for  $\alpha_3$  indicates that it may be systematically steeper due to unresolved massive binary systems by at least this amount. For  $m < 1 \text{ M}_\odot$  unseen companions are corrected for, thus  $\alpha_0$ ,  $\alpha_1$ , and  $\alpha_2$  are the slopes of the real single star IMF.

Weidner & Kroupa (2006) refer to this form as the standard or *canonical stellar IMF* because it fits the luminosity function of Galactic field and cluster stars below  $1 \text{ M}_\odot$  and also represents young populations above  $1 \text{ M}_\odot$  (Kroupa *et al.*, 1993; Kroupa, 2001, 2002). Because this IMF has been obtained from solar-neighbourhood data for low-mass and very-low-mass stars and from many clusters and OB associations for massive stars, it is an average IMF.

It is apparent that  $\xi(m)$  becomes considerably flatter below  $1.0 \text{ M}_\odot$  with a broad peak between  $0.08$  and  $1.0 \text{ M}_\odot$ . The latter is a fundamental fact that remains unexplained but one should remark the success of recent numerical studies to reproduce the observed IMF to some degree by simple hydrodynamical simulations of star-forming regions (Bate & Bonnell, 2005).

There exist two other fundamental questions regarding the IMF. The first is the question whether there exists a physical upper mass limit of stars. From the theoretical point of view it is still under debate whether the formation process of stars allows for masses larger than

$100 M_{\odot}$  (e.g. Weidner & Kroupa, 2004). Observational studies, that tried to answer this question by statistical means (e.g. Oey & Clarke, 2005; Figer, 2005; Koen, 2006) or high-resolution observations of the most massive objects known (e.g. Maíz Apellániz *et al.*, 2007) provide evidence that stars do not seem to exceed a mass of  $150 M_{\odot}$  (see also the review of Zinnecker & Yorke, 2007).

Second and strongly correlated with the first point, it is not yet clear whether the mass of the most massive star in a cluster correlates *non-trivially* with the cluster mass, i.e. the mass function of a cluster is simply obtained by random sampling from the IMF or a physically determined process. Recently, Weidner & Kroupa (2006) found evidence that there exists a well-defined relation between the most massive star in a cluster and the cluster mass and conclude that the conjecture that a cluster consists of stars randomly picked from an invariant IMF between  $0.01$  and  $150 M_{\odot}$  appears to be wrong. The algorithm that best corresponds to the observational data is one in which the cluster masses are picked from a mass function of embedded clusters and then filled with stars by randomly selecting from the canonical IMF, sorting the stellar masses in ascending order and constraining their sum to be the cluster mass (“sorted sampling”). Their interpretation of the results is that star clusters appear to form in an ordered fashion, starting with the lowest-mass stars until feedback by consecutive addition of more massive stars is able to outweigh the gravitationally induced formation process. However, one has to stress that large observational uncertainties of stellar masses and cluster masses and ages do make the correlation between cluster mass and maximum stellar mass less clear.

# 3. Numerics

## 3.1. Introduction

Numerical simulations are a powerful tool to examine the physical processes of complex systems that can not be solved analytically or when it is too dangerous, time consuming or simply impossible to carry out a real experiment. Typical applications are simulations of fluid dynamics, chemical or nuclear reactions, structure of molecules or solids, and evolution of self-gravitating systems. In the present thesis the focus is on the investigation of self-gravitating systems, in particular the dynamics of young star clusters.

In any numerical simulation a balance has to be found between two constraints: On the one hand the *realism*, i.e. the inclusion of all physical effects, and the maintenance of the accuracy of calculations; and on the other hand, the *efficiency*, i.e. the limitations given by the computational effort. For the specific numerical treatment of star cluster dynamics many different kinds of approaches have been undertaken to suffice both, the most important of which are listed in the following:

- codes based on direct force integration, among them
  - the family of NBODY-codes NBODY1–NBODY6 (Aarseth, 2003),
  - Starlab (McMillan & Hut, 1996),
- statistical models, among them
  - Fokker-Planck approximation (Cohn, 1979),
  - Monte-Carlo method (Hénon, 1971),
- usage of high-performance parallel computers (Spurzem, 1999), or
- the construction of special hardware devoted to this purpose (Makino *et al.*, 1997).

Since the dynamics of star clusters are dominated by two-body relaxation, the numerical treatment of such *collisional systems* (see Chapter 2) requires very high accuracies (with an energy error per crossing time typically  $\Delta E/E < 10^{-5}$ ). Because the present investigation concentrates on young stellar systems, i.e. only several crossing times old, numerical errors

introduced by long integration times (e.g. rounding errors) are negligible. The term “collisional” here always refers to systems, whose evolution is influenced by relaxation through elastic two- or more-body encounters, not to physical collisions, where two stars collide and merge or disrupt each other.

Direct  $N$ -body methods require the treatment of the classical gravitational “ $N$ -body” problem, that is - the challenge of finding a solution for the orbital motions of  $N$  bodies, represented by point-masses, that are interacting with one another purely by gravitational forces. This is done by solving numerically a set of  $N$  Newtonian equations of motion of the form

$$\ddot{\mathbf{r}}_i = \mathbf{a}_i = \frac{\mathbf{F}_i}{m_i} = - \sum_{\substack{j=1 \\ j \neq i}}^N Gm_j \frac{\mathbf{r}_i - \mathbf{r}_j}{|\mathbf{r}_i - \mathbf{r}_j|^3} = - \sum_{\substack{j=1 \\ j \neq i}}^N Gm_j \frac{\mathbf{r}_{ij}}{r_{ij}^3}, \quad i = 1, \dots, N \quad (3.1)$$

where  $G$  is the gravitational constant,  $m_i$  and  $m_j$  the masses,  $\mathbf{r}_{ij} = \mathbf{r}_i - \mathbf{r}_j$  the relative coordinate, and  $r_{ij} = |\mathbf{r}_i - \mathbf{r}_j|$  the modulus of bodies  $i$  and  $j$ .

The sums have to be evaluated for all  $N - 1$  neighbours (index  $j$ ) of each of the  $N$  particles (index  $i$ ), thus for a complete calculation of all forces,

$$\sum_{i=1}^N \sum_{j=1}^{i-1} 1 = \frac{N(N-1)}{2} = O(N^2) \quad (3.2)$$

operations have to be performed. Hence the computational effort for a direct  $N$ -body calculation rises quadratically with the particle number.

When performing numerical simulations one has to be aware that this method is not straight forward and suffers from several error contributions, among them (i) the chaotic behaviour of  $N$ -body systems and thus strong dependence on initial conditions, (ii) the discreteness of integration time steps, and (iii) the operation with finite floating points. Fortunately, there are possibilities to control these contributions by (i) averaging over a sample of identical systems with (small) random deviations in their initial conditions, (ii) choosing substantially smaller time steps than the minimum time scale of the entire system, and (iii) extending floating point precision by operation on architectures with higher bit counts.

As a consequence of the high accuracy requirements for simulations of cluster dynamics, the use of high-order time-integration schemes and direct force summations are the tools of choice to track the stellar trajectories as precisely as possible (c.f. Spurzem, 1999).

For this reason NBODY6++ (Spurzem, 1999) was selected for the present investigation of star cluster dynamics. It is a direct  $N$ -body code which allows high precision calculations due to its 4th order Hermite integrator. In comparison to NBODY6 (Aarseth, 2003), it has the additional advantage of a parallelised force summation, allowing for considerable speed up by using multiple processor machines.

## 3.2. The Code: NBODY6++

An extensive description of the code NBODY6 is given by Aarseth (2003). It is also used as a reference for NBODY6++ in the following which is identical to NBODY6 apart from the additional parallelisation of the force calculation. NBODY6++ is a state of the art application for simulations of gravitational systems, as well for few-body systems as massive clusters or even galaxies, including miscellaneous options and switches which allow to include effects of primordial binaries, tidal fields, interstellar clouds, stellar evolution and many more. The general force integration as given by Eq. (3.1) is realised by a 4th order Hermite integrator. The main motivation for the use of NBODY6++ is its high accuracy in treating two-body interactions which is indispensable when following the trajectory of each star deep into the potential of its neighbour. The two-body integration is solved by a regularisation scheme which eliminates the numerical problem of the singular Newtonian force. There are some more features like individual block-time steps or a neighbour scheme which are described in the following.

### 3.2.1. The Hermite Integration Method

The Hermite scheme is a predictor-corrector scheme, which needs the acceleration as well as the first time derivative of the acceleration for the computation of a particle's position. It has proven to be effective in calculations where high accuracy in time integration as well as in the force integration is of need.

A predictor-corrector scheme is a three-step algorithm which can be used to solve initial value problems of ordinary differential equations. First, from the positions and their time derivatives known at time  $t$  a Taylor expansion of a certain order is used to generate an estimate of the same quantities at time  $t + \Delta t$ , known as the *prediction*. The truncation of the Taylor expansion controls the order of the integration method. Next, the predicted quantities are used for the evaluation of the acceleration and its derivatives at time  $t + \Delta t$ . These will be in general different from the predicted ones. Finally, these differences, the so-called *error signals*, are used together with appropriate coefficients, depending on the order of the integration algorithm, to calculate the positions and their derivatives anew. This step is known as the *correction* and is the main ingredient of a predictor-corrector algorithm. It accounts for a feedback mechanism which damps the instabilities that might be introduced by the predictor step. This general scheme will be now presented in more detail for the Hermite integration method.

Each particle is completely specified by its mass  $m$ , position  $\mathbf{r}_0$ , and velocity  $\mathbf{v}_0$ , where the subscript 0 denotes an initial value at time  $t_0$ . The equation of motion for a particle  $i$  is given

by its momentary acceleration  $\mathbf{a}_{0,i}$  due to all other particles and its time derivative  $\dot{\mathbf{a}}_{0,i}$  as

$$\mathbf{a}_{0,i} = - \sum_{i \neq j} G m_j \frac{\mathbf{r}_{0,ij}}{r_{0,ij}^3}, \quad (3.3)$$

$$\dot{\mathbf{a}}_{0,i} = - \sum_{i \neq j} G m_j \left[ \frac{\mathbf{v}}{r_{0,ij}^3} + \frac{3\mathbf{r}_{0,ij}(\mathbf{v}_{0,ij} \cdot \mathbf{r}_{0,ij})}{r_{0,ij}^5} \right], \quad (3.4)$$

where  $G$  is the gravitational constant,  $\mathbf{r}_{0,ij} = \mathbf{r}_{0,i} - \mathbf{r}_{0,j}$  the relative coordinate,  $r_{0,ij} = |\mathbf{r}_{0,i} - \mathbf{r}_{0,j}|$  the modulus, and  $\mathbf{v}_{0,ij} = \mathbf{v}_{0,i} - \mathbf{v}_{0,j}$  the relative space velocity to the particle  $j$ . In NBODY6++ a new position and velocity is predicted for the next time step  $t$  by a Taylor expansion for  $\mathbf{r}_i(t)$  and  $\mathbf{v}_i(t)$  up to third order:

$$\mathbf{r}_{p,i}(t) = \mathbf{r}_0 + \mathbf{v}_0(t-t_0) + \mathbf{a}_{0,i} \frac{(t-t_0)^2}{2} + \dot{\mathbf{a}}_{0,i} \frac{(t-t_0)^3}{6}, \quad (3.5)$$

$$\mathbf{v}_{p,i}(t) = \mathbf{v}_0 + \mathbf{a}_{0,i}(t-t_0) + \dot{\mathbf{a}}_{0,i} \frac{(t-t_0)^2}{2}. \quad (3.6)$$

The direct values of  $\mathbf{r}_p$  and  $\mathbf{v}_p$  do not fulfil the requirements for an accurate high-order integrator. Therefore, an improvement is made by the Hermite interpolation which approximates the higher accelerating terms by an own Taylor series:

$$\mathbf{a}_i(t) = \mathbf{a}_{0,i} + \dot{\mathbf{a}}_{0,i}(t-t_0) + \mathbf{a}_{0,i}^{(2)} \frac{(t-t_0)^2}{2} + \mathbf{a}_{0,i}^{(3)} \frac{(t-t_0)^3}{6}, \quad (3.7)$$

$$\dot{\mathbf{a}}_i(t) = \dot{\mathbf{a}}_{0,i} + \mathbf{a}_{0,i}^{(2)}(t-t_0) + \mathbf{a}_{0,i}^{(3)} \frac{(t-t_0)^2}{2}. \quad (3.8)$$

Here, the values of  $\mathbf{a}_{0,i}$  and  $\dot{\mathbf{a}}_{0,i}$  are already known, but a further derivation of Eq. (3.4) for the two missing orders on the right hand side turns out to be quite cumbersome. Instead, one determines the additional acceleration terms from the predicted (“provisional”)  $\mathbf{r}_p$  and  $\mathbf{v}_p$ ; their acceleration and time derivative according to Eq. (3.3) and (3.4) are calculated anew, calling these new terms  $\mathbf{a}_{p,i}$  and  $\dot{\mathbf{a}}_{p,i}$ , respectively. Because these values ought to be generated by the former high-order terms also (which was avoided), they are put into the left-hand sides of (3.7) and (3.8). Solving Eq. (3.8) for  $\mathbf{a}_{0,i}^{(2)}$ , then substituting it into (3.7) and simplifying yields the third derivative:

$$\mathbf{a}_{0,i}^{(3)} = 12 \frac{\mathbf{a}_{0,i} - \mathbf{a}_{p,i}}{(t-t_0)^3} + 6 \frac{\dot{\mathbf{a}}_{0,i} + \dot{\mathbf{a}}_{p,i}}{(t-t_0)^2}. \quad (3.9)$$

Similarly, substituting (3.9) into (3.7) gives the second derivative:

$$\mathbf{a}_{0,i}^{(2)} = -6 \frac{\mathbf{a}_{0,i} - \mathbf{a}_{p,i}}{(t-t_0)^2} - 2 \frac{2\dot{\mathbf{a}}_{0,i} + \dot{\mathbf{a}}_{p,i}}{t-t_0}. \quad (3.10)$$

Note, that the desired high-order accelerations are found just from the combination of the low-order terms for  $\mathbf{r}_0$  and  $\mathbf{r}_p$ . Although one never derived higher than the first derivative, the higher orders are easily achieved through (3.3) and (3.4). This is called the Hermite scheme. The accuracy of the integrator is virtually the same as in the case of an explicit high-order derivation (Makino & Hut, 1988). Finally, one extends the Taylor series for  $\mathbf{r}_i(t)$  and  $\mathbf{v}_i(t)$ , Eqs. (3.5) and (3.6), by two more orders, and finds the “corrected” position  $\mathbf{r}_{1,i}$  and velocity  $\mathbf{v}_{1,i}$  of the particle  $i$  at the computation time  $t_1$  as

$$\mathbf{r}_{1,i}(t) = \mathbf{r}_{p,i}(t) + \mathbf{a}_{0,i}^{(2)} \frac{(t-t_0)^4}{24} + \mathbf{a}_{0,i}^{(3)} \frac{(t-t_0)^5}{120}, \quad (3.11)$$

$$\mathbf{v}_{1,i}(t) = \mathbf{v}_{p,i}(t) + \mathbf{a}_{0,i}^{(2)} \frac{(t-t_0)^3}{6} + \mathbf{a}_{0,i}^{(3)} \frac{(t-t_0)^4}{24}. \quad (3.12)$$

The integration cycle for other upcoming steps may now be repeated from the beginning, Eqs. (3.3) and (3.4). The error in  $\mathbf{r}$  and  $\mathbf{v}$  within the two time steps  $\Delta t = t_1 - t_0$  is proportional to  $\Delta t^4$  (Makino, 1991; Makino & Aarseth, 1992).

### 3.2.2. Hierarchical Time Steps

Stellar systems are characterised by a fair range of densities which gives rise to different time scales of the orbital parameters. In the classical picture, the two closest bodies, which require the smallest time-step due to the strong gravitational attraction, would determine the time-step of force calculation for the entire system. However, for bodies in regions where the force variation is relatively small, a permanent re-computing of the force terms is time consuming, so, in order to economise the calculation, these objects shall be allowed to move a longer distance before a recomputation of the forces becomes necessary. This is the idea of a vital method used in NBODY6++ for assigning different time-steps,  $\Delta t = t_1 - t_0$ , that are quantised powers of 2, between the force computations, the so-called “block time-step scheme” (Aarseth, 1963).

First, each particle is assigned its own individual  $\Delta t_i$ . The block-time steps are then synchronised by taking the next-lowest  $\Delta t_i$  that is a quantised power of 2 (Makino, 1991), building a set  $\{2^{-i}, i = 0, \dots, i_{\max}\}$ , where  $i_{\max}$  is the minimum integer that fulfils the relation for the smallest time step,  $\Delta t_{\min} > 2^{-i_{\max}}$ . This creates a group (block) of several particles which are due to movement at each time step, as illustrated in Fig. 3.1. In this example, the particle  $i$  has the smallest time step at the beginning, so its phase space coordinates are determined at each time step. The time step of particle  $k$  is twice as large as  $i$ 's, and its coordinates are just extrapolated (“predicted”) at the time steps marked by odd numbers, while a full force calculation is due at multiples of the largest  $\Delta t_i$  of all particles, here determined by particle  $m$ . The step width of each particle may be altered after the end of the integration cycle, as demonstrated

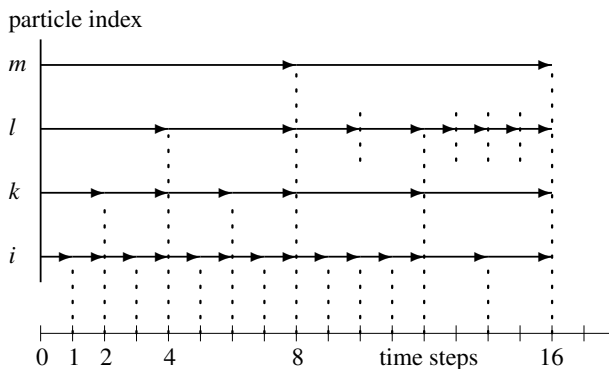


Figure 3.1.: Block time steps exemplary for four particles.

for the particles  $k$  and  $l$  beyond the label “8”. The time steps have to stay commensurable with both, each other as well as the total time, such that a hierarchy is guaranteed.

As a first estimate, the rate of change of the acceleration seems to be a reasonable quantity for the choice of an appropriate time step:  $\Delta t_i \propto |\mathbf{a}_i|/|\dot{\mathbf{a}}_i|$ . But it turns out that for special situations in a many-body system, it provides some undesired numerical errors, so that nowadays the following formula is mainly used (Aarseth, 1985):

$$\Delta t_i = \sqrt{\eta \frac{|\mathbf{a}_{1,i}| |\mathbf{a}_{1,i}^{(2)}| + |\dot{\mathbf{a}}_{1,i}|^2}{|\dot{\mathbf{a}}_{1,i}| |\mathbf{a}_{1,i}^{(3)}| + |\mathbf{a}_{1,i}^{(2)}|^2}}, \quad (3.13)$$

where  $\eta$  is a dimensionless accuracy parameter which controls the error. In most applications it is taken to be  $\eta \approx 0.02$  to  $0.04$ .

In the code, the time-steps are adjusted to their appropriate values fairly quick. Although successive steps normally change smoothly, it is prudent to restrict the growth by a stability factor of 1.2 in order to exclude rapid changes in peculiar cases and to guarantee maximum precision in the force calculation.

### 3.2.3. The Ahmad-Cohen Scheme

The computation of the full force for each particle in the system makes simulations very time-consuming for large particle numbers. Therefore, it is desirable to construct a method to speed up the calculations in NBODY6++ while retaining the collisional approach. One way to achieve this is to employ a “neighbour scheme”, suggested by Ahmad & Cohen (1973).

The basic idea is to split the force polynomial (3.7) for a given particle  $i$  into two parts, an

irregular and a regular component:

$$\mathbf{a}_i = \mathbf{a}_{i,\text{irr}} + \mathbf{a}_{i,\text{reg}}. \quad (3.14)$$

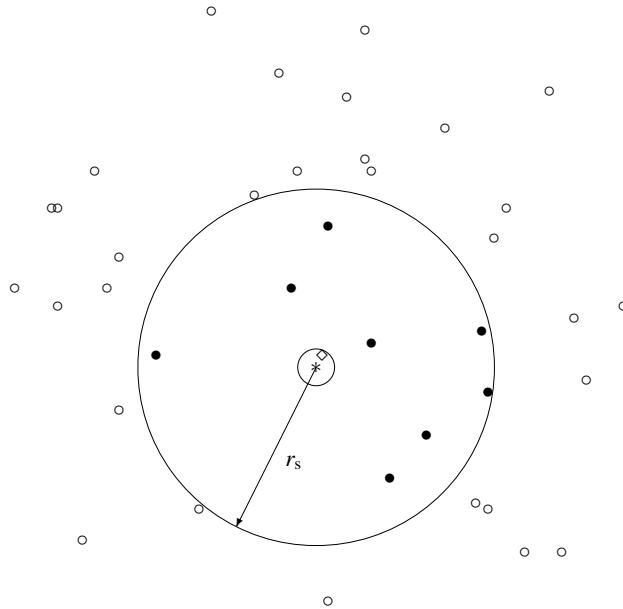
The irregular acceleration  $\mathbf{a}_{i,\text{irr}}$  results from particles in a certain neighbourhood of  $i$ . They give rise to a stronger fluctuating gravitational force, which is determined more frequently than the regular one of the more distant particles that do not change their relative distance to  $i$  so quickly. The full summation in Eq. (3.3) can be replaced by a sum over the  $N_{\text{nb}}$  nearest particles for  $\mathbf{a}_{i,\text{irr}}$  and a distant contribution from all the other. Whether a particle is a neighbour or not is determined by its distance; all members inside a specified sphere (“neighbour sphere”) with radius  $r_s$  are held in a list, which is modified at the end of each “regular time-step” when a total force summation is carried out. In addition, approaching particles within a surrounding shell satisfying  $\mathbf{r}_{0,ij} \cdot \mathbf{v}_{0,ij} < 0$  are included. This “buffer zone” serves to identify fast approaching particles before they penetrate too far inside the neighbour sphere.

Fig. 3.2 and 3.3 show how the Ahmad-Cohen scheme works for one particle (Makino & Aarseth, 1992). At the beginning of the force calculation, a list of neighbour objects around the particle  $i$  is created first (filled dots). From this neighbour list the irregular component  $\mathbf{a}_{i,\text{irr}}$  is calculated, and then the summation is continued to the distant particles obtaining  $\mathbf{a}_{i,\text{reg}}$ . At the same time the first time derivative is also calculated. From Eqs. (3.7) and (3.8) the position and velocity of the particle  $i$  are predicted. At time  $t_{1,\text{irr}}$  the “corrector” is applied only for  $\mathbf{a}_{i,\text{irr}}$  from the neighbours; the regular component is not corrected, but obtained by extrapolating  $\mathbf{a}_{i,\text{reg}}$ . At the next step,  $t_{2,\text{irr}}$ , the same predictor-corrector method proceeds for the neighbour particles, while the correction of the distant acceleration term is still neglected. When  $t_1$  is reached, the total force is calculated on the basis of the full application of the Hermite predictor-corrector method. Also, a new neighbour list is constructed using the positions at time  $t_1$ . Thus, at certain times only the forces from neighbours (irregular time-step,  $t_{\text{irr}}$ ), while at other times both the forces from neighbours and distant particles (regular time-step,  $t_{\text{reg}}$ ) are calculated.

For a neighbour list of size  $N_{\text{nb}} \ll N$ , this procedure can lead to a significant gain in efficiency, provided the respective time scales for  $\mathbf{a}_{i,\text{irr}}$  and  $\mathbf{a}_{i,\text{reg}}$  are well separated (Makino & Aarseth, 1992). The actual size is controlled by choosing an appropriate radius  $r_s$  for the neighbour sphere. Aarseth (1985) determined

$$\frac{N_{\text{nb}}}{N/2} \left( \frac{r_{\text{hm}}}{r_s} \right)^3 \approx \frac{n_{\text{nb}}}{n_{\text{hm}}}, \quad (3.15)$$

where  $N$  is the total particle number,  $r_{\text{hm}}$  and  $r_s$  are the half-mass radius and the radius of the



- \* particle  $i$
- ◇ regularized neighbour of particle  $i$
- $r_s$  radius of neighbour sphere of particle  $i$
- members of the neighbour sphere of particle  $i$  ("irregular" forces contribution)
- particles outside the neighbour sphere of particle  $i$  ("regular" forces contribution)

Figure 3.2.: Illustration of the neighbour scheme for particle  $i$  (after Aarseth, 1985).

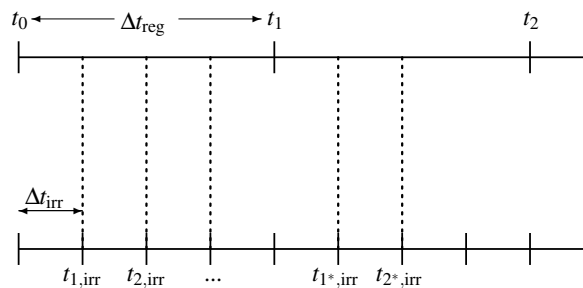


Figure 3.3.: Regular and irregular time steps (after Makino & Aarseth, 1992).

neighbour sphere, and  $n_{\text{nb}}$  and  $n_{\text{hm}}$  are the particle densities inside the neighbour sphere and inside the half-mass radius, respectively. The approximation in the equation is due to the fact, that one-half of the total particle number is not necessarily the half of the total mass, to which  $r_{\text{hm}}$  is related.

The implementation of both the neighbour scheme and the hierarchical time-step scheme makes the overall integration quite complex. The neighbour scheme is a *spatial* hierarchy, which avoids a frequent force calculation of the remote particles that provide a smooth potential with respect to particle  $i$ ; that potential is superposed by fluctuations caused by close-by stars that are compensated by the more frequent force determination. The time step scheme, in contrast, exhibits the *temporal* behaviour of the intervals for re-calculation of the full force in order to maintain the exactness of the trajectory; time steps chosen too small slow down the advancing calculation losing the computer's efficiency.

### 3.2.4. KS-Regularisation

The fourth main feature of the NBODY6++code is the treatment of close interactions. In case that the relative distances  $R$  of particles decrease ( $R \rightarrow 0$ ), integration time steps  $\Delta t$  must be reduced to impracticable small values and at the same time forces  $F$  can become arbitrarily large (see Eqs. (3.3) and (3.4)), introducing numerical errors due the limited precision of floating point numbers represented by a processor. It is the numerical integration of bound systems, i.e. binaries in the simplest case, that is most critical, since the recurring minimum distances lead to a significant slow-down of the entire integration and to a fast accumulation of numerical errors that could dominate the cluster evolution early on. An elegant solution to deal with such close interacting particles is the *regularisation*, symbolised as the diamond in Fig. 3.2.

In the case of a binary, the idea is to take both stars out of the main integration cycle, replace them by their centre of mass and advance the usual integration with this pseudo-particle. For the resolution of the orbital motion of the two components a different *regularised* coordinate system is used. The underlying transformation involves the mapping in the complex plane by a  $4 \times 4$  matrix. Thus the transformation from physical spacial coordinates in three dimensions and time requires a set of four regular spatial coordinates, including one fictitious spatial coordinate, and a fictitious time (Aarseth, 1985). The  $4 \times 4$  matrix maps the space and velocity into a form resembling a harmonic oscillator. The equations of motion become *regular* then, removing the singularity with respect to the distance  $R$  in the equations of motion. The method itself goes back to Kustaanheimo & Stiefel (1965), known as *KS-regularisation*. It makes an accurate calculation of a perturbed two-body motion possible and reduces force contributions from distant particles that act only as tidal forces,  $F_{\text{ext}} \propto R^{-3}$ . The time-step of such a *KS-regularised pair* is independent of the eccentricity, the number of integration steps

is lower than in the non-regularised case, and numerical stability of even circular motion is improved.

In the case of strong interactions among more than two bodies, a description in terms of one dominant two-body motion tends to break down and the application of a single KS-regularisation would require frequent initialisations of the dominant pair. Thus a new formulation, generally known as *multiple regularisation* is required, where *multiple* refers to the special treatment of at least two separations to remove singularities. By expanding the KS-regularisation to two coupled KS-regularisation, the isolated and perturbed 3-body problem can be integrated in a well-behaving manner (Aarseth & Zare, 1974). For higher particle numbers, a new concept with improved notation is realised by introducing the dominant two-body forces along a chain of inter-particle vectors, where the pair-wise attractions are treated by the KS formalism, thus termed *Chain Regularisation*. The mathematical method is described in more detail by Mikkola & Aarseth (1993) and references therein.

### 3.2.5. Data structure

Special attention is paid to the data structure of the code. The main point here is that all particles, single particles and pseudo-particles (that represent regularised multiples), are stored in an array in ordered fashion. Because the number of single particles can decrease due to escape from the cluster and the number of pseudo-particles changes due to initialisation or termination of regularised multiples, the data structure must be maintained by a flexible scheme. Instead of using pointers, the arrays are reordered each time the particle configuration changes. This *relabeling scheme* involves additional computational effort and programming complexities, but has the advantage of a well-ordered scheme and fast operation on arrays. The reordering, of computational effort  $O(N)$ , pays off in particular because it allows a sequential force summation, thus optimising a process that is  $O(N^2)$ .

The present data structure is composed of domains in a storage array according to the particle type and hierarchical level of regularisation. Single particles are stored sequentially in the range 1 to  $N$ , where  $N$  is the number of single particles. Pseudo-particles resulting from two-body regularisation of two single particles are arranged behind, in the range  $N + 1$  to  $N_{\text{tot}} = N + N_p$ , where  $N_p$  is the number of regularised pairs. The components of each such pseudo-particle, i.e. the two single particles, are always located at the beginning of the single particle domain. Thus the components of the first KS-pair at position  $N + 1$  are the first two single particles at position 1 and 2, the components of the second KS-pair at position  $N + 2$  are the next two single particles at position 3 and 4 and so forth. In general, the single particles at  $I_{s,1} = 2I_p - 1$  and  $I_{s,2} = 2I_p$  are components of the KS-pair  $I_p$ , which itself is located at  $N + I_p$ . Consequently, the domain of single particles is composed of two sub-domains, the regularised single particles located in the range 1 to  $2N_p$ , and the non-regularised single

particles in the range  $2N_p + 1$  to  $N$ . If a new KS solution is initialised, particle array locations at  $2N_p + 1$  and  $2N_p + 2$  are exchanged with those of the regularisation candidates and the corresponding pseudo-particle is introduced at  $N + N_p + 1$ . Afterwards, the current pair index,  $N_p$ , is increased by one. In the reverse case of terminating an existing KS regularisation with index  $I_p^{\text{term}}$ , all pairs with larger index,  $I_p^{\text{term}} < I_p \leq N_{\text{tot}}$ , i.e. those that have been initialised more recently, are moved down by one position and the corresponding pseudo-particle is removed. Accordingly, its components  $I_{s,1}^{\text{term}} = 2I_p^{\text{term}} - 1$  and  $I_{s,2}^{\text{term}} = 2I_p^{\text{term}}$  are placed at  $2N_p - 1$  and  $2N_p$ , which are liberated by shifting all regularised single particles with index  $2I_p^{\text{term}} < I_s \leq 2N_p$  down by two positions.

Due to the reordering and removal of particles in storage it is convenient to define a unique label,  $\mathcal{N}_i$ , for each particle before the integration is started. This label is then used to identify a particle at any time during integration. Initially all single particles, regularised and non-regularised, are labelled  $\mathcal{N}_i = i$ ,  $i = 1, \dots, N_0$ , where  $N_0$  is the initial single particle number. The pseudo-particles of KS pairs are labelled  $\mathcal{N}_{N_0+k} = \mathcal{N}_{2k-1} + N_0$ ,  $k = 1, \dots, N_p$ .

The data structure becomes more complicated if hierarchically regularised particles occur. Though regularisation is done straight forward by building larger pseudo-particles from lower level hierarchies, bookkeeping of names and particle attributes requires a clever scheme. This is realised by the so-called *ghost particle* in order to maintain relevant quantities of the original second KS component. The ghost particle is taken out from integration and placed at the array position of the original second KS component. The new KS regularisation replaces the original primary component. The higher order pseudo particle is introduced into a new list, the *merger list*, with index  $I_m$ , which serves to store the unique merger and ghost labels for later recovery. In case of the lowest order hierarchy, i.e. a binary-single or binary-binary merger, the pseudo-particle is given a negative label  $\mathcal{N}_{N_0+N_p+i} = -\mathcal{N}_{N_0+k}$ , related to the label of the first KS component,  $\mathcal{N}_{N_0+k}$ . In order to distinguish between higher levels of a hierarchy, the convention is to assign a label  $\mathcal{N}_i$  which is effectively  $-2N_0$  smaller than the previous one. This clear algorithm allows an arbitrary number of hierarchical levels referring to the same system as it increases in complexity. However, currently NBODY6++ allows only up to six members to form a hierarchical pseudo-particle.

### 3.2.6. Parallelisation

The parallelisation of NBODY6 was implemented by Spurzem (1999) using the Message Passing Interface standard (MPI).

In the version of NBODY6++ used in this work, the parallelisation is restricted to the Hermite integration algorithm and related routines (e.g. energy calculation) whereas the regularisation schemes (KS, Chain) are not optimised for the distribution of numerical effort on multiple processors. Thus any speedup on parallel computers can only be achieved in the di-

rect force integration while the formation of regularised subsystems reduces the performance immediately to that of a single processor machine.

The crucial requirement for an efficient parallelisation is a hierarchical time step scheme, as described in Section 3.2.2. The implementation of the block step scheme provides an even superior parallel efficiency: at the large time steps always huge groups of particles are due in time for correction.

The optimal neighbour number for the Ahmed-Cohen neighbour scheme is not well defined for parallelised processes. However, it has been found that adopting a constant neighbour number of the order of 20-50 is sufficient at least up to particle numbers of  $N = 50000$  (Spurzem, 1999). After each regular time step the new neighbour list is communicated along with the new particle positions to all processors of the parallel machine, thus making it possible to do the irregular time step in parallel as well.

In the present implementation the parallelisation is done only according to parallel sections (“do loops”) in the code; there is no domain decomposition (distributing particles on the processor). Thus at the end of any time steps new results have to be broadcast to all other processing units. A systolic algorithm is used for that which scales linearly in communication time with the number of processors,  $N_{\text{comm}} \propto n_{\text{PE}}$ . In this so-called “parallel group execution algorithm” only subgroups of particles, whose size scales as  $N^{2/3}$ , have to be communicated across the processor network. Thus the overall communication overhead scales as  $N_{\text{comm}} \propto N^{2/3} n_{\text{PE}}$ .

### 3.3. Modifications of the Code

For the purpose of the present framework – the setup of dynamical cluster models and tracking of encounters – the original NBODY6++ code had to be modified and extended by self-written procedures. The tasks involve

1. the generation of a Maxwellian velocity distribution,
2. the generation of a two-part density distribution,
3. the estimate of a numerically robust cluster centre,
4. the tracking of encounters,
5. the implementation of a spatially and temporally variable external potential,

and will be discussed in the forthcoming sections.

### 3.3.1. Maxwellian Velocity Distribution

As discussed in Section 2.3.1, the velocity distribution of young star clusters is well approximated by a Maxwellian distribution, in agreement with theoretical considerations and observational data. The requirement for an adequate setup led to the implementation of a random number generator with Gaussian deviates. The adopted algorithm is described by Press *et al.* (1993) and is briefly outlined in the following.

Generalising transformation methods to multiple dimensions, the joint probability distribution  $p(y_1, y_2, \dots) dy_1 dy_2 \dots$  of functions  $y_1, y_2, \dots$  of random deviates  $x_1, x_2, \dots$  is

$$p(y_1, y_2, \dots) dy_1 dy_2 \dots = p(x_1, x_2, \dots) \left| \frac{\partial(x_1, x_2, \dots)}{\partial(y_1, y_2, \dots)} \right| dy_1 dy_2 \dots, \quad (3.16)$$

where  $p(x_1, x_2, \dots) dx_1 dx_2 \dots$  is the joint probability distribution of the  $x$ 's and  $|\partial(\cdot)/\partial(\cdot)|$  is the Jacobian determinant of the  $x$ 's with respect to the  $y$ 's. The *Box Muller* method involves the transformation of the Gaussian distribution,

$$p(y) dy = \frac{1}{\sqrt{2\pi}} e^{-y^2/2} dy, \quad (3.17)$$

using the relations

$$y_1 = \sqrt{-2 \ln x_1} \cos 2\pi x_2, \quad (3.18)$$

$$y_2 = \sqrt{-2 \ln x_1} \sin 2\pi x_2, \quad (3.19)$$

between two uniform deviates in the interval  $[0, 1]$ ,  $x_1, x_2$ , and the quantities  $y_1, y_2$ . If one picks the coordinates  $v_1$  and  $v_2$  of a random point in the unit circle, instead of picking the uniform deviates  $x_1$  and  $x_2$  in the unit square, then the sum of the squares,  $R^2 \equiv v_1^2 + v_2^2$  is a uniform deviate, that can be used for  $x_1$ , while the angle that  $(v_1, v_2)$  defines with respect to the  $v_1$  axis can serve as the random angle  $2\pi x_2$ . The advantage of this scheme is that the cosine and sine in Eq. (3.18) can be written as  $v_1/\sqrt{R^2}$  and  $v_2/\sqrt{R^2}$ , obviating the trigonometric function calls. The Maxwellian velocity distribution is then generated by picking for each particle three Gaussian deviates, one for each velocity component.

### 3.3.2. Two-Part Density Distribution

In simulations of star clusters mainly one of three types of density distribution functions is used: (i) the Plummer sphere (Plummer, 1911), (ii) the isothermal sphere (e.g. Binney & Tremaine, 1987), or (iii) the family of King models (King, 1966). The advantage of distributions (i) and (iii) is that they behave well and provide a good fit to a large variety of (most

older) clusters. In contrast, (ii) has infinite density at the origin but is a good representation of the density *and* velocity distribution of young clusters, the latter being the Maxwellian distribution (see Section 2.3.1).

However, detailed observations of young clusters show that the distribution varies towards the core of the cluster, becoming flatter or steeper. To account for this feature, the setup procedure in NBODY6++ has been extended to generate a two-part density distribution, with different slopes for the core,  $\rho \propto r^{-\alpha_1}$ , and the outer region,  $\rho \propto r^{-\alpha_2}$ . For simplicity, the cluster is generated as a uniform sphere and scaled to the desired size in a second step.

The generation of such a distribution is straight forward. First, the probability of a particle to be in one of the two regions is evaluated. Then a random uniform deviate is picked from the interval  $[0, 1]$  which determines the membership. The coordinates of the particle are assigned uniform deviates  $x_1, x_2, x_3$  in the interval  $[0, 1]$ , and the corresponding radius vector,  $r = (x_1^2 + x_2^2 + x_3^2)^{\frac{\alpha+1}{2}}$ , is calculated, where  $\alpha$  is either  $\alpha_1$  or  $\alpha_2$ . If the particle is a member of the outer region,  $\alpha = \alpha_2$ , then the radius vector must be evaluated against the core radius,  $r_{\text{core}}$ ; if  $r < r_{\text{core}}$  the algorithm must be repeated. For a member of the core no further decision making is required.

### 3.3.3. Cluster Centre

The analysis of data from numerical simulations of star clusters requires – in particular when compared to observational data – a reference point that is representative of the cluster centre. The determination of a robust central reference point is an important *non-trivial* task.

From a theoretical point of view, the centre-of-mass should define the cluster centre. However, in numerical simulations of star clusters a small fraction of particles is accelerated in close encounters to velocities largely exceeding the escape velocity of the system. Because small in number and thus not isotropically distributed, these escapers cause, at large distances from the cluster, a significant shift of the centre-of-mass towards the outer cluster regions. Hence the centre-of-mass does not serve as a good central reference point. Another candidate for a central reference point would be the (mass or number) density centre of a cluster. Because observers usually use either the highest brightness concentration or the maximum projected number density of objects as a reference point, this approach would seem to be promising when comparing numerical results and observational data.

In the original NBODY6++ code there already exists a routine to calculate the density centre (core.f). The scheme works as follows: First, a sample of particles is built by cutting out a spherical volume around the cluster centre that contains at least 20 % of the total population. For each particle the local mass and number density of the five nearest neighbours is calculated. The cluster density centre is then built from the sum of the particle positions of the subsample weighted with the local mass densities. However, using the density centre as the

central reference point has as well some disadvantages. First, since star clusters are dynamically very active, the local particle densities change very fast with time and thus the estimated density centre also fluctuates very strong with time. Moreover, the choice of the five nearest neighbours to calculate the local densities is somewhat arbitrary. Depending on the geometry and the density and mass distribution of a cluster the determination of the density centre might depend significantly on the choice of the number of nearest neighbours.

Because the density centre is the ideal measure of the highest concentration of stars but varies strongly with time and cluster structure it appears intuitive to use the density centre in combination with a smoothing algorithm as the central reference point. This approach has been realised by combining the calculation of the density centre and the centre-of-mass and is described by the following algorithm:

1. Sort all stars in increasing order of the distance to the cluster density centre.
2. Pick the stars sequentially from the sorted list and build a subsample until
  - a) the subsample contains at least 10 % of total stellar population *and*
  - b) the mass of the subsample is at least 10 times the mass of the most massive star in the cluster.
3. Calculate the centre-of-mass of the subsample.

The restriction 2b takes into account that a very massive star would dominate dynamically a too small subsample. It suppresses a strong influence of one star on the density centre. The centre-of-mass of the subsample serves as the new cluster centre. This algorithm combines the advantages of both quantities, the density centre and the centre of mass: it keeps the cluster centre close to the strongest concentration of particles in the cluster but takes a larger stellar sample into account to smooth the fluctuations with time and cluster structure.

### 3.3.4. Encounter Tracking

The key aspect of this work is the determination of the encounter-induced disc-mass loss in a cluster environment. For this purpose two different types of numerical simulations have been combined. First, as part of previous work, a parameter study of star-disc encounters has been performed, resulting in a fit formula for the disc-mass loss as a function of the masses and the separation of two stars (see Section 4.4.2). Using this fit formula, in a second step the individual disc-mass loss of star cluster members was determined from simulations of star cluster dynamics, in which the encounter history of all stars was tracked. In the present investigation the encounter tracking has been widely extended in the form of additional routines in NBODY6++.

### Numerical method

The first ingredient of the encounter tracking is the determination of the strongest perturber of each star at a given integration time step, i.e. the body with the maximum gravitational force. Numerically this algorithm is effective because the neighbour scheme of NBODY6++ (see Section 3.2.3) allows to restrict the search of a particle's potential perturbers to its neighbour list and thus reduces the number of calculations significantly. However, a marginal slow-down occurs because the determination of the strongest perturber requires the consequent update of positions and its derivatives for all members of the neighbour list to the current time step (see the discussion of time steps in Section 3.2.2). The separate integration of KS-regularised particles in NBODY6++ (see Section 3.2.4) requires an additional scheme to account for perturbations. However, trivially, the two members of a KS-regularised pair are each other's strongest perturbers.

This scheme, repeated for each (irregular) integration step in the course of the simulation (see Section 3.2.3 for the definition of an irregular time step), provides the masses and the positions and velocities of the perturber and the perturbed star that are used to determine the orbital parameters and the time period of interaction. This information is required to determine the disc-mass loss later on (see Section 4.4.2). While the interaction period can be easily obtained by recording the time step of the beginning and the end of the interaction with the same perturber, the determination of the periastron is more challenging. Due to the discreteness of time in numerical simulations the minimum separation of two particles at a certain time step is usually not the minimum distance of their orbits as shown in Fig. 3.4. This drawback can be solved by an interpolation of the periastron (and the corresponding time) from the interaction parameters at some other time steps and is described in detail further below.

Once the full interaction parameters are determined they are checked for consistency with the isolated star-disc encounters of the parameter study. This involves two criteria: (i) the orbit curvature has to be concave with respect to the perturbed star, i.e. the perturbed star must be located in the focus closest to the orbit (because only this type of orbits has been simulated), and (ii) the opening angle of the orbit section must amount to at least 10 % of the maximum opening angle of the corresponding conic section (in terms of eccentricity), because otherwise the interaction time is too short and the disc-mass loss would be overestimated by the fit formula. Orbits that fulfil these criteria, termed “regular” in the following, are stored in a list that forms the backbone for the subsequent determination of the disc-mass loss.

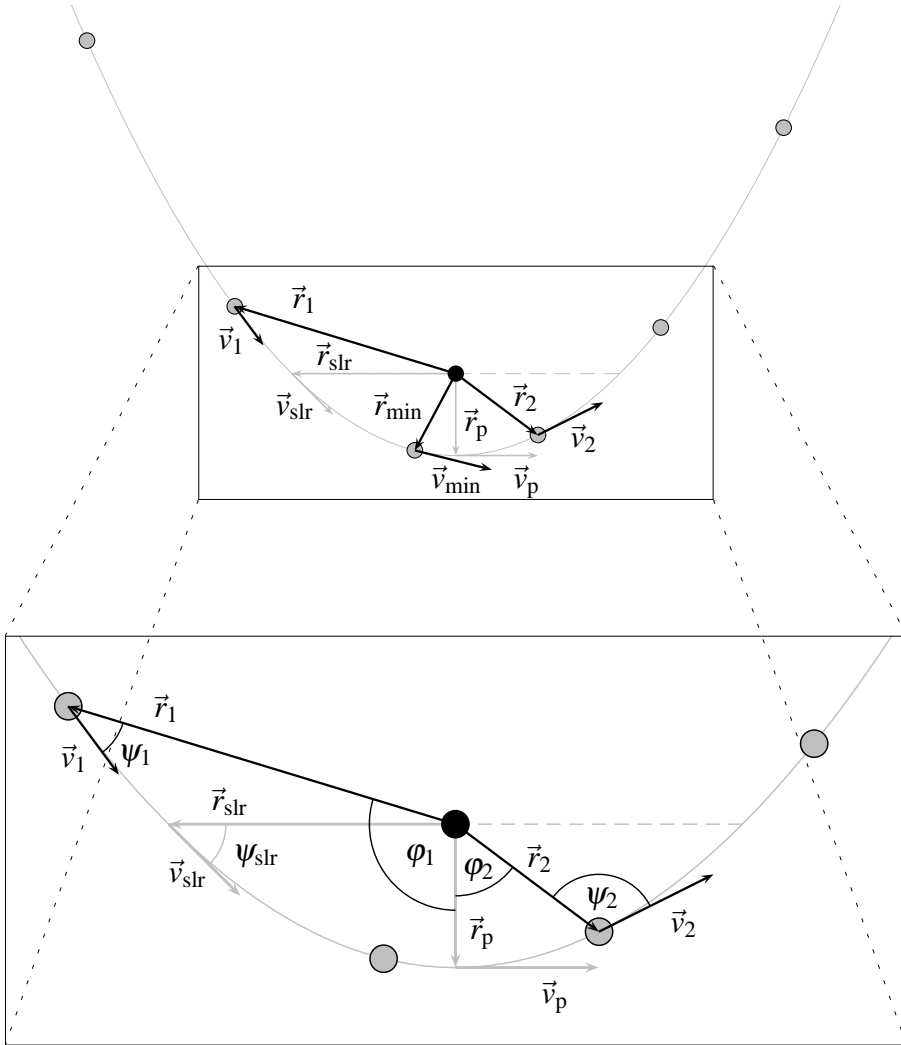


Figure 3.4.: Illustration of the geometrical parameters of the periastron interpolation scheme. The black circle marks the position of the perturbed star, the grey circles mark the positions of the perturber at sequential time steps. Quantities of the two time steps before,  $t_1$ , and after the minimum separation,  $t_2$ , are denoted by the corresponding indices. The upper part of the figure illustrates a larger portion of the orbit with positions and velocities of the three time steps before, after and at the minimum separation itself. The lower part represents an enlarged view and contains all quantities that are used for the interpolation scheme (see text).

### Periastron interpolation

For the calculation of the disc-mass loss of a star due to the fly-by of a perturber, the determination of the minimum separation – the distance at periastron – is crucial. Due to the discreteness of time in numerical simulations the minimum separation of two particles at a certain time step is usually not the minimum distance of their orbits as shown in Fig. 3.4. As long as the interaction is weak and orbital periods are long the difference between the numerical minimum separation and the distance at periastron is negligible. However, in case of strong interactions differences can be quite large - large enough that the estimated relative disc-mass loss differs by more than a tenth or the orbit may be even classified as non-regular (with respect to the criteria presented above) and rejected.

Thus it is necessary to interpolate the periastron from the given discrete orbit points. For the interpolation the encounter parameters at time steps before,  $t_1$ , and after the minimum separation,  $t_2$ , are used. In the following the frame will be always centred on the perturbed star, so only the orbital motion of the perturber is investigated.

For the interpolation it is assumed that the orbit is (nearly) Keplerian, i.e. there is no significant perturbation by a third body. This assumption is of course not always valid in the dense cluster regions, where encounters can occur between small  $N$ -body systems. However, since the derived disc-mass loss is based on simulations of two-body systems, contributions from higher order perturbations can not be quantified. So the disc-mass loss can be underestimated in this case.

Exact circular orbits can not be treated with this method because there is no global minimum of separation over time. However, circular orbits are neither expected due to the perturbation by the cluster stars nor is the applied disc-mass loss calculation valid for low eccentricities. Circular orbits will be thus neglected in the following.

The interpolation scheme is as follows (see also Fig. 3.4): The vectors  $\vec{r}_1$  and  $\vec{r}_2$  are the separation vectors at the time step before and after the minimum separation, respectively. They enclose the angle  $\vartheta$ ,  $\vartheta = \sphericalangle(\vec{r}_1, \vec{r}_2)$ , while  $\varphi_1$  and  $\varphi_2$  are the angles enclosed by the (not yet determined) separation vector at periastron,  $\vec{r}_p$ , and either one of the separation vectors,  $\varphi_1 = \sphericalangle(\vec{r}_p, \vec{r}_1)$  and  $\varphi_2 = \sphericalangle(\vec{r}_p, \vec{r}_2)$ . Hence

$$\vartheta = \varphi_2 - \varphi_1. \quad (3.20)$$

The given variables underlie some restrictions. Since the separation vectors are estimated at different times, they usually cannot be identical. Consequently, the angle  $\vartheta$  cannot be an integer multiple of  $2\pi$ , and the angles  $\varphi_1$  and  $\varphi_2$  have to be non-zero. Furthermore, the

problem is restricted to one single orbit revolution. In summary,

$$\begin{aligned}
 \vec{r}_1 &\neq \vec{r}_2, \\
 \vartheta &\in (0, 2\pi), \\
 \varphi_1 &\in (-\pi, 0), \\
 \varphi_2 &\in (0, \pi).
 \end{aligned} \tag{3.21}$$

The first step towards a determination of the periastron is to determine the enclosed angle  $\vartheta$ .

### Determination of $\vartheta$ .

The cosine of  $\vartheta$  can be easily determined from

$$\vec{r}_1 \vec{r}_2 = |\vec{r}_1| |\vec{r}_2| \cos \vartheta,$$

yet it requires to determine whether  $\vartheta$  is in the interval  $[0, \pi)$  or  $[\pi, 2\pi)$ . According to Fig. 3.4, the problem can be solved by including the direction of motion. Via the projection of the velocity vector at time  $t_1$ ,

$$\vec{v}_1 \vec{r}_1 = v_1 r_1 \cos \psi,$$

where  $v_1 = |\vec{v}_1|$  and  $r_1 = |\vec{r}_1|$ , one can determine the velocity component tangential to  $\vec{r}_1$ , called here  $\vec{v}_{1,t}$ ,

$$\vec{v}_{1,t} = \frac{\vec{r}_1}{r_1} v_1 \cos \psi.$$

The normal component  $\vec{v}_{1,n}$ ,

$$\vec{v}_{1,n} = \vec{v}_1 - \vec{v}_{1,t} = \vec{v}_1 - \vec{r}_1 \frac{\vec{v}_1 \vec{r}_1}{r_1^2},$$

is then used to determine the interval:

$$\vec{r}_2 \vec{v}_{1,n} \begin{cases} > 0: & \vartheta \in [0, \pi) \\ \leq 0: & \vartheta \in [\pi, 2\pi) \end{cases}.$$

The second step is to determine the unknown  $\varphi_1$  (which fixes  $\varphi_2$  due to Eq. (3.20)) which will then be used to obtain  $\vec{r}_p$ .

### Determination of $\varphi_1$ .

A Keplerian orbit, which is a conical section, is described at any point by the distance to its focal point  $r$ ,

$$r = \frac{(1 + \varepsilon)r_p}{1 + \varepsilon \cos \varphi}, \quad (3.22)$$

where  $\varepsilon$  is the eccentricity of the orbit,  $r_p$  the distance from the focal point to the periastron,  $r_p = |\vec{r}_p|$ , and  $\varphi$  the angle enclosed by the periastron  $r_p$  and the connecting line to an arbitrary point on the orbit  $r$ .

Because a numerical treatment is limited in accuracy and the orbit of two interacting particles in a  $N$ -body system is (most probably) *not* strictly Keplerian, one has to account for different eccentricities at two different times. However, if the eccentricities are too different, the assumption of a nearly Keplerian orbit is not justified. In the framework of the encounter tracking this has been considered in the form of two limiting criteria: (i) the eccentricities must not deviate by more than 0.5, or (ii) the eccentricities must not deviate by more than 10%. If *both* criteria are not met the orbit is rejected as “non-regular”. Thus, using relation (3.22) for the separations at the two time steps before and after the minimum separation,  $r_1$  and  $r_2$ , and allowing for (slightly) different eccentricities,  $\varepsilon_1$  and  $\varepsilon_2$ , one obtains

$$r_1 = \frac{(1 + \varepsilon_1)r_p}{1 + \varepsilon_1 \cos \varphi_1}, \quad r_2 = \frac{(1 + \varepsilon_2)r_p}{1 + \varepsilon_2 \cos \varphi_2}, \quad (3.23)$$

and hence after elimination of the separation at periastron  $r_p$ ,

$$\begin{aligned} \frac{r_1(1 + \varepsilon_1 \cos \varphi_1)}{1 + \varepsilon_1} &= \frac{r_2(1 + \varepsilon_2 \cos \varphi_2)}{1 + \varepsilon_2} \\ &\stackrel{(3.20)}{=} \frac{r_2(1 + \varepsilon_2 \cos(\vartheta + \varphi_1))}{1 + \varepsilon_2} \\ &= \frac{r_2(1 + \varepsilon_2(\cos \vartheta \cos \varphi_1 - \sin \vartheta \sin \varphi_1))}{1 + \varepsilon_2}. \end{aligned} \quad (3.24)$$

Introducing new variables,

$$\begin{aligned}
 R_1 &= r_1(1 + \varepsilon_2), \\
 R_2 &= r_2(1 + \varepsilon_1), \\
 R &= R_1 - R_2, \\
 E_1 &= \varepsilon_1 R_1, \\
 E_2 &= \varepsilon_2 R_2, \\
 C &= E_2 \cos \vartheta - E_1, \\
 S &= E_2 \sin \vartheta,
 \end{aligned} \tag{3.25}$$

where  $R_1, R_2 > 0$  and  $E_1, E_2 \geq 0$ , one obtains the compact expression

$$R = C \cos \varphi_1 - S \sin \varphi_1. \tag{3.26}$$

The solution of Eq. (3.26) for the angle  $\varphi_1$  requires a case differentiation of either  $C$  or  $S$ , which will be done here for  $S$ :

1. In case of  $S = 0$ :

$$S = 0 \quad \Leftrightarrow \quad \vartheta = m\pi, \quad m \in \mathbb{Z} \quad \vee \quad E_2 = 0 \tag{3.27}$$

$$\stackrel{\Leftrightarrow}{r_1 \neq r_2} \quad \vartheta = \pi \quad \vee \quad \varepsilon_2 = 0 \tag{3.28}$$

where the last equivalency follows from Eqs. (3.21) and (3.25). Another case differentiation for the two variables is necessary:

a) In case of  $\varepsilon_2 = 0$ :

$$R = r_1 - r_2(1 + \varepsilon_1) \stackrel{(3.26)}{=} C \cos \varphi_1 = -E_1 \cos \varphi_1 = -\varepsilon_1 r_1 \cos \varphi_1.$$

Before solving, one has to consider that  $\varepsilon_1$  can be zero.

i. In case of  $\varepsilon_1 = 0$ :  $R = 0 \Rightarrow r_{\text{peri}} = r_1 = r_2$ .

This is the case of a circular orbit which was excluded at the beginning.

ii. In case of  $\varepsilon_1 \neq 0$ :  $\varphi_1 = \arccos \left( \frac{r_2(1 + \varepsilon_1) - r_1}{r_1 \varepsilon_1} \right)$ .

b) In case of  $\vartheta = \pi$ :  $C = -(E_1 + E_2) \Rightarrow R = -(E_1 + E_2) \cos \varphi_1$ .

Excluding ( $\varepsilon_1 = 0 \wedge \varepsilon_2 = 0$ ), because this case has been already treated,

$E_1 + E_2 \neq 0$  and one obtains

$$\varphi_1 = \arccos\left(-\frac{R}{E_1 + E_2}\right).$$

2. In case of  $S \neq 0$ :

The solution can be obtained directly via quadrature,

$$\cos \varphi_1 = \frac{RC}{E} \pm \sqrt{\frac{R^2 C^2}{E^2} + \frac{S^2 - R^2}{E}}, \quad (3.29)$$

where  $E = C^2 + S^2$ . The sign determines whether  $\varphi_1$  is in the interval  $[0, \pi/2)$  or  $[\pi/2, \pi)$ , i.e. whether the separation vector  $\vec{r}_1$  lies in the quadrant above or below the semi-latus rectum according to Fig. 3.4. This can be decided by comparing the angle  $\psi_1$  enclosed by the separation and the velocity vector at time  $t_1$ ,  $\vec{r}_1$  and  $\vec{v}_1$ , with its value at the semi-latus rectum,  $\psi_{\text{slr}} = \arcsin(e^2 + 1)^{-1/2}$  (see Eq. (A.4)). One finds

$$\varphi_1 = \begin{cases} \arccos\left(\frac{RC}{E} + \sqrt{\frac{R^2 C^2}{E^2} + \frac{S^2 - R^2}{E}}\right) & \text{if } \sin\left[\arccos\left(\frac{\vec{r}_1 \vec{v}_1}{r_1 v_1}\right)\right] > (e^2 + 1)^{-1/2} \\ \arccos\left(\frac{RC}{E} - \sqrt{\frac{R^2 C^2}{E^2} + \frac{S^2 - R^2}{E}}\right) & \text{if } \sin\left[\arccos\left(\frac{\vec{r}_1 \vec{v}_1}{r_1 v_1}\right)\right] \leq (e^2 + 1)^{-1/2} \end{cases}.$$

### Determination of $r_p$ .

The estimated  $\varphi_1$  and the corresponding  $r_1$  and  $\varepsilon_1$  then determine the distance at periastron  $r_p$  via (3.22):

$$r_p = \frac{r_1(1 + \varepsilon_1 \cos \varphi_1)}{1 + \varepsilon_1}.$$

The vector  $\vec{r}_p$  can be obtained simply by linear combination,

$$\vec{r}_p = a\vec{r}_1 + b\vec{r}_2,$$

where

$$a = \frac{r_p(\cos \varphi_1 - \cos \varphi_2 \cos \vartheta)}{r_1(1 - \cos^2 \vartheta)},$$

$$b = \frac{r_p \cos \varphi_2 - ar_1 \cos \vartheta}{r_2}.$$

### Orbital Time of Encounter

The interpolation of the periastron involves as well an interpolation of the time when the interaction at periastron occurred. This is solved via the derivation of a relation for the time difference of two points on a Keplerian orbit as presented below. The problem will be formulated in polar coordinates  $\{r, \theta\}$ .

Consider a test particle of mass  $m$  in free flight in the gravitational field of a body with mass  $M$ . The total system energy is

$$E = -\frac{GMm}{r} + \frac{1}{2}mv^2 = -\frac{GMm}{|\vec{r}|} + \frac{1}{2}m\dot{\vec{r}}^2, \quad (3.30)$$

where

$$\vec{r} = (r \cos \theta, r \sin \theta, 0)$$

is the position vector in polar coordinates.

The solution for the orbital motion requires the first and second derivative of  $\vec{r}$ ,

$$\begin{aligned} \dot{\vec{r}} &= \dot{r}(\cos \theta, \sin \theta, 0) + r\dot{\theta}(-\sin \theta, \cos \theta, 0), \\ \ddot{\vec{r}} &= (\ddot{r} - r\dot{\theta}^2)(\cos \theta, \sin \theta, 0) + (2\dot{r}\dot{\theta} + r\ddot{\theta})(-\sin \theta, \cos \theta, 0). \end{aligned}$$

Because the gravitational force is radial there is no change in the angular momentum of the test particle and the (specific) angular momentum  $l$  is constant,

$$l = r^2\dot{\theta}. \quad (3.31)$$

This corresponds to Kepler's 2nd law. Due to the conservation of the angular momentum,

$$0 = \dot{l} = \frac{d}{dt}(r^2\dot{\theta}) = 2r\dot{r}\dot{\theta} + r^2\ddot{\theta} = r(2\dot{r}\dot{\theta} + r\ddot{\theta}),$$

the second derivative of  $\vec{r}$  reduces to

$$\ddot{\vec{r}} = (\ddot{r} - r\dot{\theta}^2)(\cos \theta, \sin \theta, 0).$$

Derivation of (3.30) leads to the equation of motion,

$$\begin{aligned} \dot{E} &= \frac{d}{dt} \left( -\frac{GMm}{|\vec{r}|} + \frac{1}{2}m\dot{\vec{r}}^2 \right) = \frac{GMm}{|\vec{r}|^2} \dot{r} + m\dot{\vec{r}}\ddot{\vec{r}} = \frac{GMm}{r^2} \dot{r} + m\dot{r}(\ddot{r} - r\dot{\theta}^2) = 0 \\ \implies \ddot{r} &= -\frac{GM}{r^2} + r\dot{\theta}^2. \end{aligned} \quad (3.32)$$

Switching to new variables and derivatives,

$$u := \frac{1}{r}, \quad \frac{d}{dt} = \frac{l}{r^2} \frac{d}{d\theta},$$

Eq. (3.32) then takes the following form:

$$\begin{aligned} \frac{l}{r^2} \frac{d}{d\theta} \left( \frac{l}{r^2} \frac{d}{d\theta} \right) &= \frac{l^2}{r^3} - \frac{GMm}{r^2} \\ \implies \frac{d^2 u}{d\theta^2} + u &= \frac{GM}{l^2} \end{aligned} \quad (3.33)$$

The solution of (3.33) is obtained from the general ansatz

$$u = A \cos \theta + B \sin \theta + \frac{GM}{l^2}. \quad (3.34)$$

Two restrictions specify the solution:

The reference for the angle  $\theta$  is the periastron  $\vec{r}_p$ ,

$$r|_{\theta=0} = r_p \implies u|_{\theta=0} = \frac{1}{r_p}.$$

The radial velocity at periastron is zero,

$$\vec{r} \cdot \dot{\vec{r}}|_{\theta=0} = 0 \implies \dot{r}|_{\theta=0} = 0 \implies \left. \frac{du}{d\theta} \right|_{\theta=0} = -\left. \frac{\dot{r}}{l} \right|_{\theta=0} = 0.$$

Thus Eq. (3.34) reduces to

$$u = \left( \frac{1}{r_p} - \frac{GM}{l^2} \right) \cos \theta + \frac{GM}{l^2},$$

and one obtains the conic sections as the general solution of the orbital motion,

$$r = \frac{r_p(1 + \varepsilon)}{(1 + \varepsilon \cos \theta)}, \quad (3.35)$$

with the numerical eccentricity

$$\varepsilon := \frac{l^2}{GM r_p} - 1.$$

Instead of determining the distance as a function of the orbit angle  $\theta$  (also called the “true anomaly”), one might be interested in the time,  $t_0$ , an object needs to traverse a given orbit element. The orbit element is referenced to periastron, so  $\theta|_{t=0} = 0$ ,  $\theta|_{t=t_0} = \theta_0$ . The solution

is found via separation of variables. Combination of (3.31) and (3.35) gives

$$\begin{aligned}\dot{\theta} &= \frac{l}{r_p^2(1+\varepsilon)^2} (1+\varepsilon \cos \theta)^2 \\ \Rightarrow dt &= \frac{r_p^2(1+\varepsilon)^2}{l} \frac{d\theta}{(1+\varepsilon \cos \theta)^2} \\ \Rightarrow t_0 &= \int_0^{\theta_0} dt = \frac{r_p^2(1+\varepsilon)^2}{l} \int_0^{\theta_0} \frac{1}{(1+\varepsilon \cos \theta)^2} d\theta.\end{aligned}$$

The result of the integration depends on the eccentricity  $\varepsilon$ ,

$$t_0 = \frac{r_p^2(1+\varepsilon)^2}{l} \begin{cases} \left[ \frac{\varepsilon \sin \theta}{(\varepsilon^2-1)(1+\varepsilon \cos \theta)} - \frac{1}{\varepsilon^2-1} \frac{2}{\sqrt{1-\varepsilon^2}} \tan^{-1} \frac{(1-\varepsilon) \tan \frac{\theta}{2}}{\sqrt{1-\varepsilon^2}} \right] & \text{if } \varepsilon < 1, \\ \left[ \frac{1}{2} \tan \frac{\theta}{2} + \frac{1}{6} \tan^3 \frac{\theta}{2} \right] & \text{if } \varepsilon = 1, \\ \left[ \frac{\varepsilon \sin \theta}{(\varepsilon^2-1)(1+\varepsilon \cos \theta)} - \frac{1}{\varepsilon^2-1} \frac{1}{\sqrt{\varepsilon^2-1}} \ln \frac{(\varepsilon-1) \tan \frac{\theta}{2} + \sqrt{\varepsilon^2-1}}{(\varepsilon-1) \tan \frac{\theta}{2} - \sqrt{\varepsilon^2-1}} \right] & \text{if } \varepsilon > 1. \end{cases} \quad (3.36)$$

The time for a complete orbit (elliptical case) is found by substituting  $\theta = \pi$  and doubling,

$$T = 2\pi \frac{r_p^2}{l} \frac{(1+\varepsilon)^{1/2}}{(1-\varepsilon)^{3/2}}.$$

### 3.3.5. Time-Variable External Potential

The simulation of a star cluster embedded in an external Plummer potential  $\phi$  of mass  $M$ , radius  $r$ , and characteristic size  $a$  (Plummer, 1911),

$$\phi = -\frac{GM}{(r^2 + a^2)^{1/2}}, \quad (3.37)$$

related to the half-mass radius by  $R_{\text{hm}} \simeq 1.3a$ , is supported by NBODY6++. However, the standard implementation contains only a static potential, whereas simulations of young star clusters require a time-varying potential that accounts for the mass-loss due to gas expulsion in the early cluster evolution (see Section 2.3.1). Extending the integration scheme towards a time-dependent external potential is straightforward and involves a modification of the – now time-dependent – parameters  $M = M(t)$  and  $r = r(t)$  at each integration step  $dt$  by some  $dM(t)$  and  $dr(t)$ . Because the applied scheme is not self-consistent, the correction of the total system energy is strictly required. This has been realised by building the difference of the potential energy of each particle due to the Plummer potential before and after the evolution

of the potential at each time step. This difference is then added to the total system energy as a correction term.

## 4. Environmental Effect on Discs in the Orion Nebula Cluster (ONC)

In this section the impact of stellar encounters on the destruction of protoplanetary discs and dynamics in young star clusters is investigated using a prototype young stellar association: the Orion Nebula Cluster (ONC).

The specific choice of the ONC as a model case was motivated by the following:

- The ONC is thought to be a typical environment for star-formation, so results from this work can be applied to the majority of such environments and so to the fate of most stars;
- it is one of the best-studied regions in the Galaxy which constrains significantly the modelling parameters;
- its high density suggests that stellar encounters might be relevant for the evolution of circumstellar discs.

The relevance of encounters on the destruction of protoplanetary discs in the ONC is investigated by combining two different types of numerical simulation. First, star-cluster simulations of a stellar dynamical model of the ONC provide information about the frequency of encounters, the mass ratio and separation of the stars involved, and the eccentricity of the encounter orbits. Second, the results of a parameter study of star-disc encounters are used to determine the upper limits of the mass loss of the discs in encounters (Pfalzner *et al.*, 2005b; Olczak *et al.*, 2006).

After a summary of the observed parameters of the ONC, the construction of a dynamical model of the ONC is discussed in detail. Fundamental results from numerical simulations of the dynamical model are presented hereafter, followed by a discussion.

### 4.1. Structure and Dynamics of the ONC

The ONC is a rich stellar cluster with about 4000 stellar members with masses  $M \gtrsim 0.08 M_{\odot}$  in a volume  $\sim 5$  pc across. Most of the objects are T Tauri stars, but there is also strong

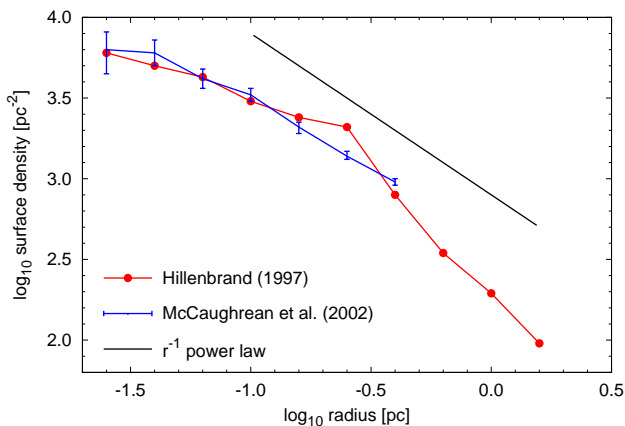


Figure 4.1.: Projected density profiles of the ONC from a observational data of McCaughrean *et al.* (2002) (blue line) and Hillenbrand (1997) (red line). The black line depicts the  $r^{-1}$  power law that corresponds to the projected density profile of the isothermal sphere.

evidence for the existence of several protostars (see Section 2.2.2 for a description of stellar evolutionary stages). The mean stellar mass is  $\bar{m} \approx 0.5 M_{\odot}$  and the half-mass radius  $R_{\text{hm}} \approx 1$  pc (Hillenbrand & Hartmann, 1998; Hillenbrand & Carpenter, 2000). Recent studies on the stellar mass distribution (Hillenbrand & Carpenter, 2000; Luhman *et al.*, 2000; Muench *et al.*, 2002; Slesnick *et al.*, 2004) reveal no significant deviation from the canonical stellar IMF given by Eq. (2.17).

The shape of the system is not perfectly spherical, but elongated in the north-south direction (with an ellipticity of  $\varepsilon \approx 0.3$ ; Hillenbrand & Hartmann, 1998). The probable reason for this asymmetry is the gravitational potential of a massive molecular ridge in the background of the cluster, OMC 1, which is part of the much larger complex of the Orion molecular cloud (Hillenbrand & Hartmann, 1998). The mean age of the whole cluster has been estimated to be  $t_{\text{ONC}} \approx 1$  Myr, although a significant age spread of the individual stars is evident (Hillenbrand, 1997; Palla & Stahler, 2000). Today, star formation is no longer occurring in the cluster itself, only in the background molecular cloud.

After a short period of intense star formation, the ONC has expelled most of the residual gas, so that now only a few solar masses of ionised gas are present in the inner  $\sim 1$  pc (Wilson *et al.*, 1997). The density and velocity distribution of the ONC resembles an isothermal sphere (see Fig. 4.1): From the outer edge the number of stars falls linearly with decreasing radius  $r$  down to 0.1 pc; inside this cluster core, the distribution function becomes flatter (Jones & Walker, 1988; McCaughrean & Stauffer, 1994; Hillenbrand, 1997; Hillenbrand & Hartmann, 1998; McCaughrean *et al.*, 2002). The central number density  $\rho_{\text{core}}$  in the inner

0.053 pc reaches  $4.7 \cdot 10^4 \text{ pc}^{-3}$  (McCaughrean & Stauffer, 1994; McCaughrean *et al.*, 2002) and makes the ONC the densest nearby ( $<1 \text{ kpc}$ ) young stellar cluster. The dense inner part of the ONC, also known as the Trapezium Cluster (TC), is characterised by  $R_{\text{TC}} \lesssim 0.3 \text{ pc}$  and  $N_{\text{TC}} \approx 750$ , or  $\rho_{\text{TC}} \approx 10^3 \text{ pc}^{-3}$ .

In their proper motion study of the ONC, Jones & Walker (1988) found the velocity dispersion to be nearly constant at all cluster radii and obtained a one-dimensional velocity dispersion  $\sigma_{\text{1D}}^{\text{JW}} = 2.5 \text{ km s}^{-1}$ . This translates into a three-dimensional velocity dispersion of  $\sigma_{\text{3D}}^{\text{JW}} = \sqrt{3}\sigma_{\text{1D}}^{\text{JW}} = 4.3 \text{ km s}^{-1}$ . Recently, Fűrész *et al.* (2008) obtained a somewhat higher one-dimensional velocity dispersion of  $\sigma_{\text{1D}}^{\text{F+}} = 3.1 \text{ km s}^{-1}$  from radial velocity measurements. However, they caution that their velocity distribution of ONC stars has a peak that is too low compared to the expected Gaussian distribution with dispersion  $\sigma_{\text{1D}}^{\text{F+}}$ , so the result of Jones & Walker (1988) will be adopted here.

This velocity dispersion translates into a crossing time of

$$t_{\text{cr}} = 2R_{\text{hm}}/\sigma \approx 0.5 \text{ Myr}, \quad (4.1)$$

and the virial ratio  $Q_{\text{vir}}$  of the ONC becomes

$$Q_{\text{vir}} = \frac{R_{\text{hm}} (\sigma_{\text{3D}}^{\text{JW}})^2}{2GM} \approx 1.5, \quad (4.2)$$

where  $M = \bar{m}N \approx 2000 M_{\odot}$ . This indicates that the ONC is not only far from virial equilibrium, but even seems to be gravitationally unbound ( $Q_{\text{vir}} > 1$ , see Section 2.1). However, this statement has to be treated with care because errors in the observational parameters can easily account for an error of over 50 % in this calculation (Sclally *et al.*, 2005). Besides, the estimated total mass of the ONC of  $2000 M_{\odot}$  is only a lower limit, since a substantial amount of mass could be present in undetected low-mass binary companions (Kroupa *et al.*, 2001). Furthermore, the contribution of the OMC 1 to the overall gravitational potential is still unknown, and the elongated shape of the cluster indicates that it is not negligible. Huff & Stahler (2006) suggest that the molecular cloud that formed the ONC contained about  $6000 M_{\odot}$ . Hillenbrand *et al.* (1998) estimated that the remaining part of it in the cluster background still has a mass of about  $2000 M_{\odot}$ . Combining these numbers, it seems that the ONC could be well in virial equilibrium, even after the expulsion of most of its natal gas. Thus one can probably exclude the case of a global contraction or expansion of the cluster.

Like many other stellar aggregations, the ONC shows mass segregation, with the most massive stars being confined to the inner cluster parts. The Trapezium cluster, a subgroup of about 1000 stars in a volume  $0.6 \text{ pc}$  across, represents the denser core of the ONC. It contains four luminous O and B stars at the very centre, designated as the ‘‘Trapezium’’ (e.g. Hillenbrand & Hartmann, 1998). Its most prominent member,  $\theta^1\text{C Ori}$ , has been classified

in the past as a very young, variable massive star of  $\sim 50 M_{\odot}$  and spectral type O4-6V at an age of only about  $2 \cdot 10^5$  yr (Hillenbrand, 1997; Donati *et al.*, 2002; Simón-Díaz *et al.*, 2006). After the detection of its binary nature by Weigelt *et al.* (1999), recently Kraus *et al.* (2007) determined the properties of the two components,  $\theta^1$ C Ori 1 (O5.5,  $M = 34.0 M_{\odot}$ ,  $T_{\text{eff}} = 39900$  K) and  $\theta^1$ C Ori 2 (O9.5,  $M = 15.5 M_{\odot}$ ,  $T_{\text{eff}} = 31900$  K), resulting in a system mass of  $\sim 50 M_{\odot}$ . The general binary properties of the ONC population will be addressed in a subsequent section.

Apart from its high density and young age, the evidence for protoplanetary discs around many stars in this cluster makes the ONC the ideal candidate for the present investigation. Whereas the first identification of “peculiar stellar objects” in the ONC dates back to Laques & Vidal (1979), it took more than a decade to recognise them as circumstellar discs that are ionised by the intense radiation of the Trapezium stars. O’Dell *et al.* (1993) designated these bright objects as “proplyds”, an acronym for **protoplanetary discs**. At greater distances from the cluster centre they also detected their dark counterparts: discs in silhouette, which are visible due to the bright nebular background. Thus far, about 200 bright proplyds and 15 silhouette discs have been revealed in several Hubble Space Telescope (HST) studies of the ONC (O’Dell *et al.*, 1993; O’Dell & Wong, 1996; Bally *et al.*, 1998, 2000).

In the most recent study on circumstellar discs in the Trapezium Lada *et al.* (2000) used the  $L$ -band excess as a detection criterion. They analysed 391 stars and found a fraction of 80-85 % to be surrounded by discs. This is in agreement with an earlier investigation of the larger ONC for which Hillenbrand (1997) gives a disc fraction of 50-90 % (though relying only on  $I_C - K$  colors) and justifies the assumption of a 100 % primordial disc fraction.

The disc sizes established so far vary between 50 and 1000 AU, with a typical value of 200 AU for low-mass stars (Vicente & Alves, 2005). The inferred disc masses are only accurate to an order of magnitude, but seem not to exceed a few percent of the central stellar mass, which classifies them as low-mass discs (Bally *et al.*, 1998; Williams *et al.*, 2005).

## 4.2. Construction of a Numerical Model of the ONC

The construction of a numerical model of the cluster dynamics involves the finding of the appropriate initial conditions that reproduce the observational properties of the ONC after a numerical evolution time similar to the estimated age of the ONC. Here the work of Scally & Clarke (2001) and Scally *et al.* (2005) provided vital support.

Due to the young age of the ONC, the chosen initial parameters are probably not too far from the observed ones, presented in Table 4.1.

The virial ratio  $Q_{\text{vir}}$  is the most crucial quantity for the dynamics of a cluster. It determines whether the cluster starts from contraction  $Q_{\text{vir}} < 0.5$ , equilibrium  $Q_{\text{vir}} = 0.5$ , or expansion

$N$	$R_{\text{init}}$ [pc]	$\rho(r)$ [pc <sup>-3</sup> ]	$\xi(m)$	$Q_{\text{vir}}$
4000	2.5	Eq. (4.5)	Eq. (2.17)	0.5

Table 4.1.: Initial parameters adopted for the numerical model of the Orion Nebula Cluster (ONC).

$Q_{\text{vir}} > 0.5$ . Observational data of the ONC are in good agreement with a virial equilibrium state. Because Scally *et al.* (2005) and Olczak *et al.* (2006) found from numerical modelling that the best agreement in terms of dynamics is achieved when assuming a stellar system initially in virial equilibrium, a value of  $Q_{\text{vir}} = 0.5$  is adopted for the present investigation.

Besides the initial virial ratio, the amount of gas initially contained in the cluster and later transformed into stars or expelled by stellar winds and radiation affects cluster dynamics significantly because it determines the temporal evolution of the virial ratio. As described in Section 3.3, its contribution is represented in the code by an additional (time-variable) Plummer potential. A detailed description of the setup is given in Section 5.3. However, simulations referred to in the present chapter have been performed *without* considering the potential of the surrounding Orion Molecular Cloud OMC 1. This accounts for the aim to investigate the influence of encounters on the disc-mass loss in a realistic but as simple stellar dynamical system as possible. Introducing additional parameters (four more parameters – the cloud mass and size and their time derivatives – would be required for the numerical setup of a cloud potential), that affect cluster dynamics, could probably mask the elementary stellar dynamical effects on discs, making an interpretation of the results more difficult.

For the initial velocity distribution a Maxwellian distribution was chosen. This corresponds to the expected distribution of a virialised system as assumed here and is consistent with the observed distribution (e.g. Jones & Walker, 1988). It is valid as long as the cluster can be approximated by an isolated system where stellar dynamics dominate (e.g. Binney & Tremaine, 1987). Since the numerical simulation sets in when most of the gas ought to be expelled from the cluster, the assumption is justified.

The number of initial bodies has to be chosen to at least the observational value,  $N = 4000$ , because of two reasons. Obviously, the observed number of cluster members states a lower limit on the true population of the ONC due to detection limits of faint stars and binary companions. The dynamical evolution of a star cluster causes stars to escape its gravitational potential – the cluster evaporates over time, as described in Section 2.1. In the case of a single star model, an initial number of stars of  $N = 4000$  is justified since the stellar population is observationally well sampled down to the brown dwarf limit ( $M = 0.08 M_{\odot}$ ), which is the lowest mass used in the model. Moreover, evaporation of stars during the first 1 Myr was

found to amount to less than 10 % for a system initially in virial equilibrium as assumed here. In the case of a primordial binary population,  $N = 4000$  states the initial number of “centre-of-mass particles”, i.e. the number of single stars and binaries, accounting for undetected binary companions. This approach is in agreement with Kroupa (2000). The details of the setup of a primordial binary population are described in Section 5.2.1.

The choice of the initial extension of the cluster model is mostly affected by the initial virial ratio  $Q_{\text{vir}}$ . Stellar systems in virial equilibrium do not change significantly in size over a few dynamical time scales since they are close to a relaxed state (as discussed in Section 2.1). Consequently, given the dynamical age of the ONC of just  $2t_{\text{cr}}$  (see Eq. (4.1)), an initial cluster radius of  $R_{\text{init}} = 2.5 \text{ pc}$  was chosen.

For the reasons discussed in Section 2.4 and the observational estimates for the ONC, the chosen (single star) initial mass function is that of Kroupa (2001) with a mass range between  $0.08 M_{\odot}$  and  $50 M_{\odot}$ .  $\theta^1\text{C Ori}$ , though a binary system, is treated as a single particle in the present investigation. This is because its separation,  $a \approx 10 \text{ AU}$ , is small compared to the adopted disc radius of  $150 \text{ AU}$ , causing gravitational perturbations as would arise from a single particle of the mass of the binary system. The maximum stellar mass is thus chosen to be equal to the *system mass* of  $\theta^1\text{C Ori}$ . Considering recent studies on the substellar mass function in the Trapezium (Slesnick *et al.*, 2004; Hillenbrand & Carpenter, 2000; Muench *et al.*, 2001), it would be possible to adapt a model IMF extending below the hydrogen-burning limit. However, since the focus is on the evolution of circumstellar discs of *stellar* objects and the contribution of substellar objects in terms of gravitational perturbations is expected to be minor, while the extension of the IMF would increase the computational effort, there is no reason to do so. Due to the random nature of the generation process a star with a mass of  $50 M_{\odot}$ , which corresponds to the system mass of  $\theta^1\text{C Ori}$ , is rarely produced; more commonly the generated IMF peaks at  $20\text{-}30 M_{\odot}$ . Thus the numerically generated mass distribution is artificially modified by assigning the maximum mass of  $50 M_{\odot}$  to the most massive particle after the generation process.

Another important parameter for the cluster setup is the initial density distribution. Finding a good estimate of the initial configuration by means of density is somewhat tricky because the evolution of the density distribution is not easily predictable, in particular in the dense cluster part, where dynamics are dominated by the interaction of just a small number of stars. Moreover, the fact that observational data contain only two-dimensional information of the stellar distribution poses another challenge for the three dimensional model. However, under the assumption of spherical symmetry, which is a simplification and not strictly consistent with the slightly elongated shape of the ONC as described in the previous section, the relation between a three-dimensional density distribution,  $\rho(r) \propto r^{-\alpha}$ , and its two-dimensional projection,  $\Sigma(r) \propto r^{-\beta}$ , is simply  $\alpha = \beta + 1$ . Because from observations a slope of the pro-

jected density distribution of -1 is derived nearly over the entire cluster (see Fig. 4.1), to first order the isothermal sphere,  $\rho(r) \propto r^{-2}$ , represents the density distribution of the ONC. Considering further the flattening in the core,  $\Sigma(r) \propto r^{-0.5}$ ,  $0 < r \leq 0.2$  pc, the *current* density distribution can be well represented via

$$\Sigma(r) = \begin{cases} \Sigma (r/r_{\text{core}}^{2\text{D}})^{-0.5} \arctan \sqrt{(r_{\text{cluster}}/r)^2 - 1} & \text{if } 0 < r \leq r_{\text{core}}^{2\text{D}} \\ \Sigma (r/r_{\text{core}}^{2\text{D}})^{-1.0} \arctan \sqrt{(r_{\text{cluster}}/r)^2 - 1} & \text{if } r_{\text{core}}^{2\text{D}} < r \leq r_{\text{cluster}} \\ 0 & \text{if } r_{\text{cluster}} < r \end{cases}, \quad (4.3)$$

$$\rho(r) = \begin{cases} \rho (r/r_{\text{core}}^{3\text{D}})^{-1.5} & \text{if } 0 < r \leq r_{\text{core}}^{3\text{D}} \\ \rho (r/r_{\text{core}}^{3\text{D}})^{-2.0} & \text{if } r_{\text{core}}^{3\text{D}} < r \leq r_{\text{cluster}} \\ 0 & \text{if } r_{\text{cluster}} < r \end{cases}, \quad (4.4)$$

where

$$\begin{aligned} r_{\text{cluster}} &= 2.5 \text{ pc}, \\ N &= 4000, \\ \Sigma &= 2.6 \cdot 10^3 \text{ stars pc}^{-2}, \\ r_{\text{core}}^{2\text{D}} &= 0.10 \text{ pc}, \\ \rho &= 1.0 \cdot 10^4 \text{ stars pc}^{-3}, \\ r_{\text{core}}^{3\text{D}} &= 0.16 \text{ pc}. \end{aligned}$$

Validating the initial setup by means of the best reproduction of the *current* density distribution after a simulation time of 1 Myr, the evaluation of numerous initial configurations led to the following best estimate of the *initial* (three-dimensional) density distribution:

$$\rho_0(r) = \begin{cases} \rho_0 (r/r_{\text{core},0}^{3\text{D}})^{-2.3} & \text{if } 0 < r \leq r_{\text{core},0}^{3\text{D}} \\ \rho_0 (r/r_{\text{core},0}^{3\text{D}})^{-2.0} & \text{if } r_{\text{core},0}^{3\text{D}} < r \leq r_{\text{cluster},0} \\ 0 & \text{if } r_{\text{cluster},0} < r \end{cases}, \quad (4.5)$$

where

$$\begin{aligned} r_{\text{cluster},0} &= 2.5 \text{ pc}, \\ N_0 &= 4000, \\ \rho_0 &= 3.1 \cdot 10^3 \text{ stars pc}^{-3}, \\ r_{\text{core},0}^{3\text{D}} &= 0.20 \text{ pc}. \end{aligned}$$

Fig. 4.2 shows the averaged projected density profile at two different times of a set of 40 simulations of the single star dynamical model compared to observational data of Hillenbrand (1997) and McCaughrean *et al.* (2002). The initial density profile (blue line), described by

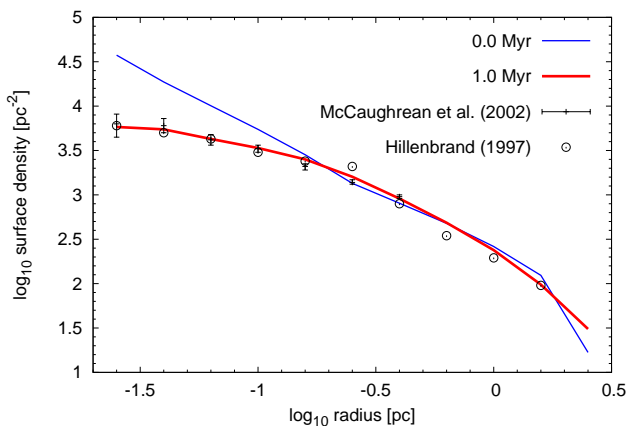


Figure 4.2.: Projected density profiles from simulations compared to observational data. The initial profile (blue line) and the profile at a simulation time of 1 Myr (red line) are shown. The observational data are from a compilation of McCaughrean *et al.* (2002) and include also the values given by Hillenbrand (1997).

Eq. (4.5), evolves in 1 Myr mainly in the inner cluster part,  $r \lesssim \log(-0.8) \text{ pc} \approx 0.16 \text{ pc}$ , where the slope flattens roughly from  $-2.3$  to  $-1.5$ . In the mid cluster part, up to  $r \approx \log(0.2) \text{ pc} \approx 1.6 \text{ pc}$ , the slope stays nearly constant, while outwards it becomes flatter again due to the escape of stars from the outer cluster part. It is evident that at 1 Myr, the adopted age of the ONC, the projected density profile (red line) matches the observational data very well and thus justifies the numerical model of the ONC used in the present investigation.

Apart from the four most massive stars, representing the Trapezium constellation, positions are assigned randomly according to the given initial density distribution, Eq. (4.5), as described in Section 3.3. The special treatment of the central stars accounts for the results of Bonnell & Davies (1998) on mass segregation in young stellar clusters from numerical simulations. The authors conclude that considering the young age of the Trapezium the massive stars did not have enough time to sink into the cluster centre due to dynamical mass segregation which occurs in approximately the cluster's relaxation time,  $t_{rh} \approx 10t_{\text{ONC}}$ . They state the most probable scenario for the initial configuration of the stellar positions is one in which the Trapezium stars are initially mass segregated, placed interior to  $0.6R_{\text{hm}}$  of the Trapezium cluster or approximately  $0.3 \text{ pc}$  for a cluster in virial equilibrium. Thus in the present investigation initially the most massive star,  $\theta^1 \text{C Ori}$ , is placed at the cluster centre and the other three Trapezium stars are placed randomly in a sphere of radius  $0.3 \text{ pc}$ .

One should be aware that the setup of a stellar system as an isothermal sphere with a cutoff at a certain radius, as found here to be a satisfying model of the ONC, ultimately leads to a non-equilibrium state. This is because the system exerts a pressure which has no opposing

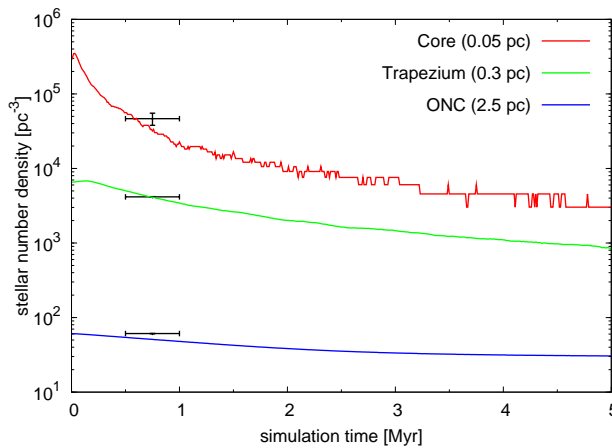


Figure 4.3.: Time evolution of stellar densities in the ONC (blue line),  $R_{\text{ONC}} = 2.5$  pc, the Trapezium Cluster (green line),  $R_{\text{TC}} = 0.3$  pc, and the cluster core (red line),  $R_{\text{core}} = 0.05$  pc, respectively. The black error bars mark the corresponding observational estimates.

external force to confine the cluster in its initial volume. Thus, independently of the chosen virial ratio, the system will expand, typically with a velocity that is on the order of 0.1 of the cluster velocity dispersion. The lower the virial ratio, the larger the fraction of stars that will form a bound system, slowing down the outward motion (see Section 2.1).

The initial configuration as described above has been adopted in the present investigation as the numerical model of the ONC. Numerical simulations were run for 5 Myr, which corresponds roughly to the life-time of a  $20 M_{\odot}$  star. By this time only the most massive star is expected to have terminated its evolution in a supernova, while the other stars still remain in the cluster (as long as they have not been expelled due to dynamical interactions). Hence, though no stellar evolution is included in the simulations and also the effect of a supernova on the circumstellar discs has not been modelled, it is expected that up to this time the effect of the stellar evolution process on the results of this investigation is negligible.

### 4.3. Dynamical Evolution of the Numerical Cluster Model

Here the pure single star model is discussed exemplary in detail. Results for models with additional components, a background potential and/or primordial binaries, are presented whenever there occur significant differences. Fig. 4.3 illustrates the temporal evolution of the particle densities in the ONC in three spherical regions of predefined size. The volume radii correspond to the total cluster extension,  $R_{\text{ONC}} = 2.5$  pc, the size of the inner Trapezium Cluster,  $R_{\text{TC}} = 0.3$  pc, and the innermost core,  $R_{\text{core}} = 0.05$  pc. The densities in the three volumes

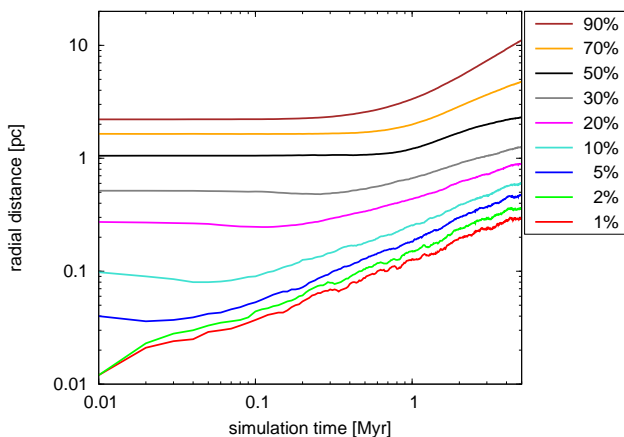


Figure 4.4.: Time evolution of Lagrangian radii for mass fractions of 1 %, 2 %, 5 %, 10 %, 20 %, 30 %, 50 %, 70 %, and 90 %, from bottom to top, respectively.

decrease over the simulation time of 5 Myr. The discontinuous distribution of the density in the core at later times is due to a small number of residual particles in that volume. However, on very short time scales after the simulation start, roughly corresponding to the crossing time of these subsystems, the density in the two smaller volumes first increases. This slight contraction of the inner cluster parts is due to the dynamical non-equilibrium state of the stellar population, caused by the initial setup of a two-part density profile with a steeper slope in the inner cluster region. Because the velocities of all stars are sampled from a Maxwellian distribution with a dispersion that accounts for a cluster in virial equilibrium, the initially steeper density profile and thus larger concentration of mass in the inner region is not balanced by the too low velocity dispersion of the stars – it is in a subvirial state. Consequently, the subsystem contracts until it is heated up sufficiently to sustain the pressure from the surrounding stars.

This is evident from a plot of the Lagrangian radii, representing volumes of constant mass fractions. Fig. 4.4 shows that the initial contraction is most prominent for Lagrangian radii of mass fractions between 5 % and 20 %, the latter value corresponding roughly to the mass fraction contained initially in the inner cluster region with the steeper density profile. The onset of contraction occurs from the inside out: the 5 % Lagrangian radius decreases ab initio and reaches a minimum at  $\sim 0.02$  Myr, while the 20 % Lagrangian radius starts to decrease at  $\sim 0.04$  Myr until a minimum at  $\sim 0.1$  Myr. This inside-out evolution is attributed to the shorter dynamical time scale of a smaller cluster volume and causes both – a faster response to the non-equilibrium state but as well a faster establishment of equilibrium at smaller radii – and produces an outward propagating density wave. However, the results of the present investigation are believed to be insensitive to this initial inner contraction because it is only

weakly pronounced and does not lead to artificially high densities over a significant period of time.

The Lagrangian radii of the larger mass fractions in Fig. 4.4 seem to show the formation of a bound subsystem at  $\sim 2$  Myr until the end of the simulation. While a significant fraction of the mass in the outer cluster region, represented by the 90 % and 70 % Lagrangian radii, is moving outwards with roughly constant velocity in this period, the expansion of half of the cluster mass slows down continuously, represented by the increasingly shallow slope of the 50 % Lagrangian radius.

Having discussed the global dynamical evolution of the cluster model, in the next section the individual stellar interactions will be addressed. The leading problem is the effect of the mutual perturbations of gravitational interactions in a cluster environment like the ONC on a star's circumstellar disc.

## 4.4. Disc-Mass Loss Induced by Star-Disc Encounters

In this section results of a previous work in the framework of a diploma thesis (Olczak *et al.*, 2006) and more recent results will be presented. The discussion of the previous results in the first three sections shall provide a compact overview of the methodology that underlies the present investigation of the disc-mass loss in star-disc encounters.

### 4.4.1. Introduction

In previous attempts to estimate the impact of stellar encounters on the disc mass it was found that only in penetrating encounters can a significant amount of mass be stripped from the disc (e.g. Clarke & Pringle, 1993; Scally & Clarke, 2001). Thus the influence of the cluster environment on the evolution of young discs by this mechanism was estimated to be low: assuming a typical disc size of 200 AU, and considering only encounters with separations of less than 100 AU, Scally & Clarke (2001) found that just 3-4 % of all discs have the potential to be destroyed by encounters. However, there are three main assumptions underlying this estimate which tend to underestimate the gravitational perturbation:

- (i) the evaluation of star-disc encounters only between equal mass stars,
- (ii) the record of just one single encounter per star,
- (iii) the evaluation of the closest instead of the most forceful encounter.

This finding gave rise to a detailed investigation of the encounter-induced disc-mass loss in an ONC-like cluster environment, where these assumptions have been dropped. Because at

present it is not possible to perform numerical particle simulations, where the stars including their surrounding discs are sufficiently resolved to determine the effect of encounters on the discs quantitatively, the dynamics of the stars and star-disc encounters have been treated in separate investigations and the results combined to determine the disc destruction rate in the cluster.

#### 4.4.2. Isolated Star-Disc Encounters

Before investigating the cumulative effect of encounters on stellar discs in a cluster model of the ONC, first the effect of such an encounter can be investigated by considering it to be isolated from the rest of the cluster. For this purpose a parameter study of encounters between stars of different masses according to the cluster mass spectrum was performed (Pfalzner *et al.*, 2005b; Olczak *et al.*, 2006). This method involves the assumption that preferentially two-body encounters occur in a cluster environment and that higher order encounters are negligible (cf. Scally & Clarke, 2001).

In the following, the term “star-disc encounters” refers to encounters in which only one of the stars is surrounded by a disc, in contrast to disc-disc encounters, which denominate encounters in which both stars are surrounded by discs. In order to determine the disc destruction rate, a number of assumptions have been made:

1. The disc-mass loss is deduced from parameter studies of star-disc encounters.
2. Only two stars are involved in an encounter event, and three- (or even more) body events are so rare that they can be neglected.
3. The discs are of low mass, i.e.  $M_d \ll 0.1M_*$ .
4. The discs around the stars do not alter the stellar dynamics in any significant way (Umbreit, 2001).
5. Viscosity and self-gravitation are negligible for the disc dynamics.
6. The encounters are assumed to be coplanar and prograde.
7. The most forceful encounter is the most destructive one.
8. Repeated encounters cause an equal *relative* disc-mass loss.

The observational evidence that most discs in the ONC are of low mass  $M_d$ , i.e.  $M_d \ll 0.1M_*$ , reduces the complexity of the numerical approach in several ways. Umbreit (2001) showed that in encounters low-mass discs do not significantly influence the encounter orbit, so that the results of the cluster simulations are applicable here. The low mass of the disc also

allows self-gravitation and viscosity to be neglected (Pfalzner, 2004). In addition, the results are scalable to other star masses. According to studies on inclined and retrograde star-disc encounters (Heller, 1993; Clarke & Pringle, 1993; Ostriker, 1994; Heller, 1995; Hall *et al.*, 1996; Pfalzner *et al.*, 2005b), the approximation towards coplanar and prograde encounters can only be interpreted as an upper limit for the disc-mass loss.

This part of the investigation is mainly based on the earlier work by Pfalzner *et al.* (2005b), who performed a parameter study of star-disc encounters where a star of mass  $M_1 = 1 M_\odot$  surrounded by a disc is perturbed by the flyby of a second star of mass  $M_2$ . The disc is assumed to extend to  $r_d = 100$  AU and the surface density to have a  $r^{-1}$ -dependence initially. This study has been extended in terms of mass ratio and separation of the encounter partners by Olczak *et al.* (2006) (see their Table 3 for the parameter range) to account for the parameter range of encounters in the ONC model.

One major result of Olczak *et al.* (2006) was the finding that the relative disc-mass loss can be fitted over the entire simulated parameter range to within 3 % by the complex function

$$\frac{\Delta M_d}{M_d} = \sqrt{\frac{M_2}{M_2 + 0.5M_1}} \log \left[ 2.8 \left( \frac{r_p}{r_d} \right)^{0.1} \right] \exp \left\{ -\sqrt{\frac{M_1}{M_2 + 0.5M_1}} \left[ \left( \frac{r_p}{r_d} \right)^{3/2} - 0.5 \right] \right\}, \quad (4.6)$$

where  $M_1$  and  $M_2$  denote the mass of the perturbed star and the perturber,  $r_p$  the separation at the periastron, and  $r_d$  the size of the disc. Two striking features of the disc-mass loss in encounters should be noted: First, the maximum mass removed in a single encounter can exceed 90% of the total disc mass. Thus in the case of a massive perturber the disc may be disrupted heavily due to only one single encounter. Second, even at distances of several disc radii massive companions have the potential to remove a significant fraction of the disc mass. For example, an encounter with a  $M_2 = 5M_\odot$  star can still lead to more than 10% disc-mass loss at a distance of three disc radii. Apart from the case of a single penetrating encounter, a disc may also be destroyed on a longer time scale via a series of distant encounters by a massive perturber.

As the cluster consists of a wide spectrum of star masses, the simulation results for  $M_1 = 1 M_\odot$  are generalised by scaling the disc radius according to

$$r_d = 150 \text{ AU} \sqrt{M_1 [M_\odot]} \quad (4.7)$$

which is equivalent to the assumption of a fixed force at the disc boundary for variable central mass. Scaling the disc size with the star mass seems intuitively right, but observational results do not give such a clear picture: Although Vicente & Alves (2005) derive a clear correlation between disc diameters and stellar masses using a sample of proplyds from Luhman *et al.* (2000), they see no indication for such a dependence when referring to data from Hillenbrand

(1997). However, as Vicente & Alves (2005) pointed out, the present Trapezium is probably not in its primordial state as various disc destruction processes have most likely altered the disc sizes considerably. Nonetheless the simulation results are also investigated under the assumption of a fixed disc radius,  $r_d = 150$  AU, uncorrelated to the mass of the star.

Eq. (4.6) is for coplanar, prograde encounters. According to studies on inclined and retrograde star-disc encounters (Heller, 1993; Clarke & Pringle, 1993; Ostriker, 1994; Heller, 1995; Hall *et al.*, 1996; Pfalzner *et al.*, 2005b), this approximation can only be interpreted as an upper limit for the disc-mass loss. However, the degree to which it overestimates the disc-mass loss should be the same independent of the mass of the star, so that the quantitative numbers could be reduced, but this should not change the qualitative results presented here. This will be discussed in more detail in Section 4.4.5.

### 4.4.3. Disc-Mass Loss in a Cluster Environment

This section contains the main results of the diploma thesis (see Olczak *et al.*, 2006). It serves as an overview of the effect that encounters have on discs in the light of the less restrictive assumptions as compared to previous studies and presented in the introduction. Combining the results of the previous Section 4.4.2 and Section 4.3, the relative disc-mass loss for each disc was obtained as a function of the simulation time. The parameters of each stellar encounter were taken from encounter lists generated during the simulation (see Section 3.3.4 for the numerical realisation). The calculation of the disc-mass loss due to encounters was performed for 20 single runs and then averaged over all simulations.

According to the fit function (4.6), the relative mass loss of a stellar disc was obtained from the disc size of the central star (scaled due to the stellar mass by using Eq. (4.7)), the relative perturber mass,  $M_2/M_1$ , and the relative periastron,  $r_p/r_d$ . The errors of the estimated relative disc-mass loss due to each encounter  $i$ ,  $\Delta^i = \Delta^i(r_p/r_d)$ , were assumed to be  $\Delta^i = 0.03$  for  $r_p/r_d \geq 1$ ,  $\Delta^i = 0.05$  for  $1 > r_p/r_d \geq 0.1$  and  $\Delta^i = 0.1$  if  $r_p/r_d < 0.1$ , according to the statistical errors of the encounter simulations. The error estimate provides the definition of an encounter: only perturbing events, for which the fit function Eq. (4.6) predicts a disc-mass loss of at least 3 % are considered as “encounters”. In other words, an encounter is defined as an event that definitely causes a disc-mass loss (in the frame of the applied prescription).

Olczak *et al.* (2006) showed that an improved encounter treatment which overcomes the three restrictions of Scally & Clarke (2001) (as presented in the introduction) is important because (i) the majority of the perturbed stars in the model clusters undergo more than one encounter, (ii) a large fraction of the perturbed stars interact with a much more massive perturber, and (iii) the largest perturbation of a disc is caused by the gravitationally most dominating body and **not** by the closest companion.

The improvement (i) has a large effect and is demonstrated in Fig. 4.5a: roughly half of all

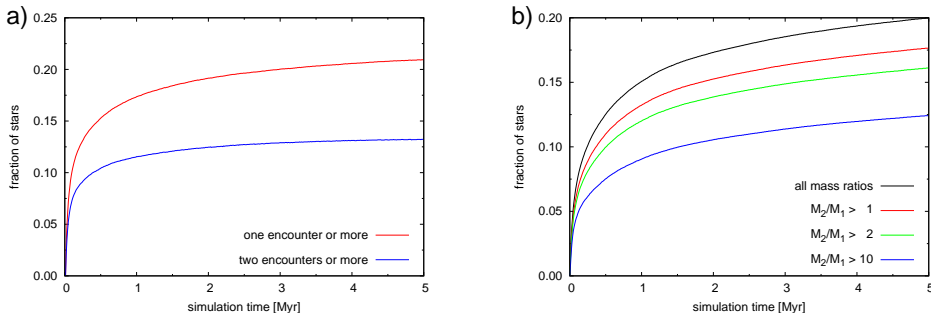


Figure 4.5.: Encounter statistics of stars. **a)** The upper panel illustrates the fraction of all perturbed stars (red line) and the fraction of all repeatedly perturbed stars as a function of time. **b)** The lower panel shows the fraction of perturbed stars as a function of time for three different minimum relative perturber masses:  $M_2/M_1 > 10$  (blue line),  $M_2/M_1 > 2$  (green line),  $M_2/M_1 > 1$  (red line). For comparison the fraction of all perturbed stars is depicted as well (black line).

discs that have been perturbed have been done so repeatedly. Thus, a realistic investigation of stellar encounters in young clusters and their effect on protoplanetary discs cannot be performed without considering the entire encounter history of each star.

In Fig. 4.5b the effect of (ii) is shown by plotting the fraction of perturbed stars for different mass ratios of the perturber and the perturbed star,  $M_2/M_1$ . If this quantity is significantly higher than unity, then even non-penetrating stellar encounters have the potential to remove the majority of a disc's mass. It is evident from Fig. 4.5b that roughly half of all perturbed stars (black line) was subject to an encounter with an at least 2 times more massive perturber (green line). The fraction of perturbed stars that were involved only in encounters with less massive stars is small and on the order of  $\sim 10\%$  of all perturbed stars, given by the difference of the black and red line. Hence the mass function of a stellar population is an important ingredient for the effect of encounters on circumstellar discs and causes encounters of equal-mass stars to represent a minority of perturbing events.

The effect of the improvements (i), (ii), and (iii) on the resulting disc-mass loss is presented in Fig. 4.6. Here the fraction of stars with discs is plotted as function of time for the entire ONC and its dense central region, the Trapezium Cluster (see Section 4.1). A star is considered disc-less if the disc mass has been reduced (due to encounters) by more than 90%. It is evident that the disc-destructive effect of encounters is most prominent in the early cluster evolution, when densities are high (see Fig. 4.3), causing roughly 20% of the stars in the Trapezium Cluster to lose their discs in about 0.1 Myr. With increasing time the fraction of remaining discs decreases further and reaches nearly an asymptotic value at the end of the simulation, which implies that star-disc encounters in a dense system like the Trapezium

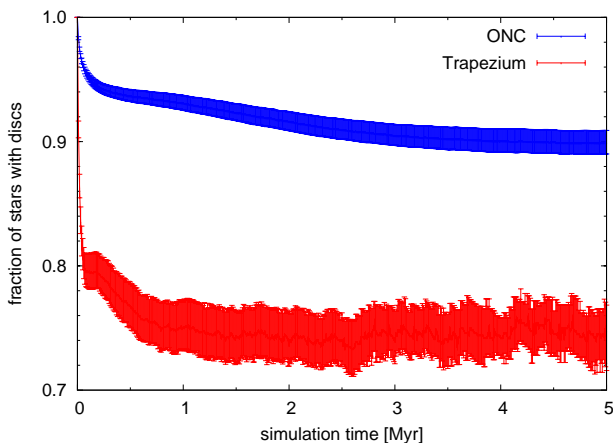


Figure 4.6.: Time evolution of the fraction of stars that possess a circumstellar disc, for a region of the size of the ONC (blue),  $R = 2.5$  pc, and the Trapezium Cluster (red),  $R = 0.3$  pc.

Cluster could even destroy up to  $\sim 25\%$  of all discs. A comparison of the resulting fraction of remaining discs in the Trapezium with the observations of Lada *et al.* (2000) shows that their derived disc fraction of 80-85% is in agreement with the numerically obtained fraction. However, one has to stress that several simplifying assumptions enter into the simulations (as discussed in Section 4.4.2) and thus a quantitative comparison has to be interpreted with caution.

Having investigated the disc-mass loss of cluster stars due to encounters in general and found that massive stars play an important role in this mechanism, it is worth to have a detailed look on how discs are influenced by encounters in dependence of their host star's mass.

#### 4.4.4. Disc-Mass Loss and Stellar Mass

The dynamical model of the ONC adopted for this part of the investigation contains only single stars without the potential of the background molecular cloud OMC 1. To minimise statistical variations, 100 simulations of the initial setup with different random number seeds have been performed. Of the final simulations, 40 fulfilled the criteria of a valid representation of the ONC and have been used for the analysis presented here.

Applying Eq. (4.6) to the results of the encounter tracking in the cluster simulations, the average disc-mass loss of stellar mass groups as a function of time is obtained. The mass ranges of the three groups have been established by requiring equal sized mass bins in logarithmic space, weighted by the slope of the IMF in the corresponding mass range (analogous to the

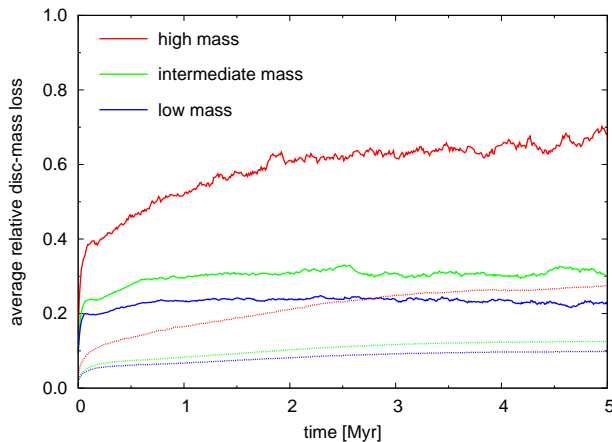


Figure 4.7.: Temporal dependence of the average relative disc-mass loss of three different stellar mass groups: low-mass stars,  $0.08 M_{\odot} \leq M_{\star} < 0.35 M_{\odot}$  (blue line), intermediate-mass stars,  $0.35 M_{\odot} \leq M_{\star} < 3.7 M_{\odot}$  (green line), and high-mass stars,  $3.7 M_{\odot} \leq M_{\star} < 50 M_{\odot}$  (red line). The solid lines mark the results for the Trapezium Cluster, the dotted lines those for the entire ONC.

derivation in Appendix D.1). The weighting is crucial because otherwise the steep slope at high masses ( $\alpha = -2.3$ , see Section 2.4) would reduce the number of stars in the high-mass range, leading to poor statistics. Looking at the temporal development of the disc mass of low-mass stars ( $0.08 M_{\odot} \leq M_{\star} < 0.35 M_{\odot}$ ), intermediate-mass stars ( $0.35 M_{\odot} \leq M_{\star} < 3.7 M_{\odot}$ ) and massive stars ( $3.7 M_{\odot} \leq M_{\star} < 50 M_{\odot}$ ) separately, Fig. 4.7 shows that massive stars have a much higher disc-mass loss than stars of lower mass, which manifests itself very early on in the cluster development. This is valid for the entire ONC but even more so for the central Trapezium Cluster.

Taking a snapshot at 2 Myr (the ONC age is estimated to be 1-2 Myr and the age of the young cluster IC 348 is roughly 2-3 Myr), the red bars in Fig. 4.8 show the average relative disc-mass loss as a function of the mass of the star for the Trapezium region. At 2 Myr the disc-mass loss is  $\sim 30\%$  for intermediate-mass stars whereas for stars with  $M_{\star} = 20 M_{\odot}$  it is  $\sim 60\%$  and for higher mass stars close to  $100\%$ . This last value has to be taken with some care because of the poor mass loss statistics in this case.

Scaling the disc size with the star mass as given by Eq. (4.7) seems intuitively right, but observational results do not give such a clear picture: Although Vicente & Alves (2005) derive a clear correlation between disc diameters and stellar masses using a sample of proplyds from Luhman *et al.* (2000), they see no indication for such a dependence in the data of Hillenbrand (1997). However, as Vicente & Alves (2005) pointed out, the present Trapezium is probably not in its primordial state and various disc destruction processes have most likely altered the

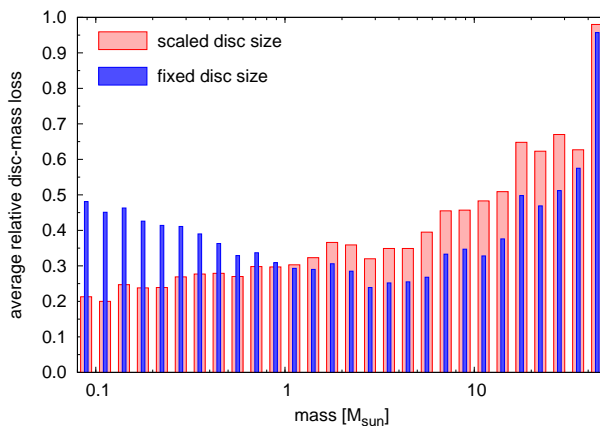


Figure 4.8.: The average relative disc-mass loss at 2 Myr for the Trapezium Cluster as a function of the stellar mass. The red bars show the results assuming the disc radius to scale as in Eq. (4.7) whereas the blue bars indicate the data for a fixed disc radius of 150 AU.

disc sizes considerably.

If one assumes that the disc size does not depend on the stellar mass as in Eq. (4.7) but is instead 150 AU for all stars, this results in a somewhat smaller relative disc-mass loss for the massive stars and an increase for the low-mass stars (see blue bars in Fig. 4.8). Nevertheless, it still holds that the disc-mass loss is considerably larger for massive stars than for intermediate-mass stars. By contrast, for the low-mass the relative disc-mass loss is now higher than for intermediate-mass stars, leaving the stars with masses in the range  $\sim 1\text{--}10 M_{\odot}$  as the ones with the lowest disc-mass loss in the cluster at 2 Myr. This corresponds to the observational results of Lada *et al.* (2006) of the young cluster IC 348.

To illustrate the underlying reason for this difference in relative disc-mass loss, Fig. 4.9 shows the average number of encounters and the average relative disc-mass loss per encounter as a function of the stellar mass. It can be seen that the number of encounters is nearly constant for low- and intermediate-mass stars but increases considerably for high-mass stars. In contrast, the average disc-mass loss per encounter is a few times higher for low- and intermediate-mass stars, but declines steeply for higher masses.

Consequently, the dynamical background of the disc-mass loss of high-mass stars and lower mass stars is quite different: the mass loss of lower-mass stars occurs through few strong encounter events, whereas the disc of high-mass stars is removed via a steady nibbling by many encounters with stars of lower mass.

Fig. 4.10 shows the average relative disc-mass loss as a function of the distance from the cluster centre for low-, intermediate- and high-mass stars. The disc-mass loss for massive

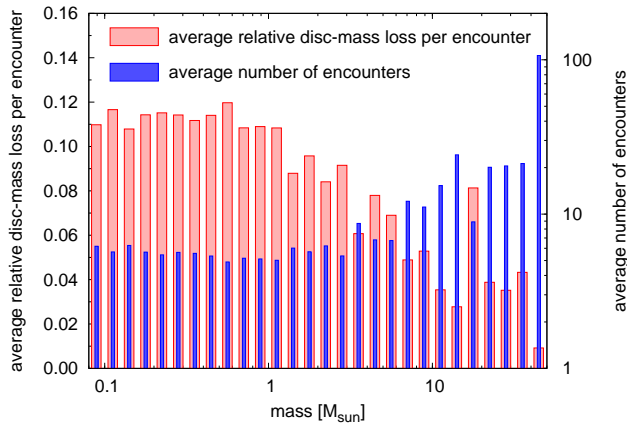


Figure 4.9.: The average number of encounters per star up to 1 Myr in logarithmic mass bins is represented as blue bars for the Trapezium Cluster. The red bars show the average relative disc-mass loss per encounter for the case of fixed size discs.

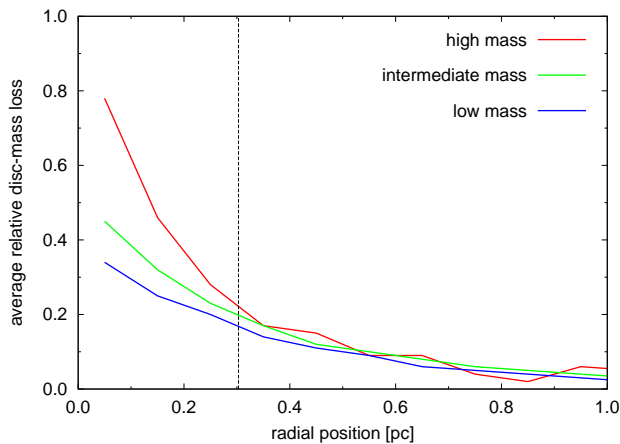


Figure 4.10.: The average relative disc-mass loss as a function of the radial distance from the cluster centre for low-mass,  $0.08 M_{\odot} \leq M_{\star} < 0.35 M_{\odot}$  (blue line), intermediate-mass,  $0.35 M_{\odot} \leq M_{\star} < 3.7 M_{\odot}$  (green line), and massive stars,  $3.7 M_{\odot} \leq M_{\star} < 50 M_{\odot}$  (red line). Here the disc size was assumed to be scaled with the stellar mass. The vertical black dashed line marks the radial extension of the Trapezium Cluster.

stars is significantly larger in the inner cluster region but this is no longer obvious for distances larger than  $\sim 0.3$  pc. The radial distribution of the mass loss can be explained as follows: First, the frequency of encounters in the cluster centre is highest due to the peak stellar density, and second, the larger fraction of high-mass stars in the cluster centre (as a consequence of mass

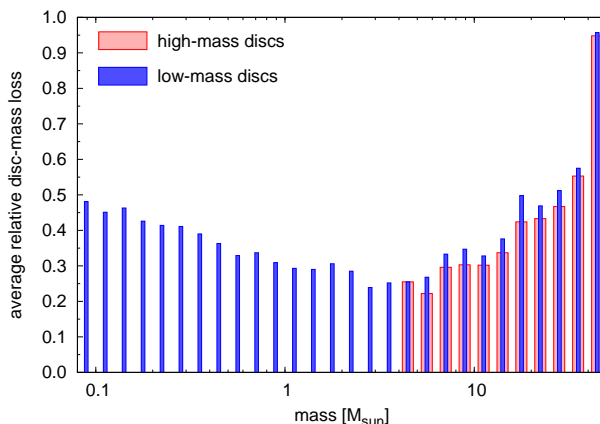


Figure 4.11.: Average relative disc-mass loss as a function of the stellar mass assuming constant disc radius. The blue bars represent stars with low-mass discs,  $M_d \ll 0.1M_*$ , whereas the red bars show the results for high-mass discs,  $M_d \gtrsim 0.1M_*$ , assumed here to surround stars of  $M_* \geq 5M_{\odot}$ .

segregation) increases the probability for massive stars to be perturbed by other high-mass stars, resulting in a higher disc-mass loss.

During the last few years a number of massive stars surrounded by high-mass discs ( $M_d > 0.1M_*$ ) have been detected (Zhang, 2005, and references therein). The question is how would the above results change if all massive stars had initially massive discs? As the interaction dynamics of high-mass discs is much less understood than for low-mass discs, only an estimate can be given here. This will be done by placing an upper limit and assuming a disc to have the same mass as its massive host star,  $M_d = M_*$ . Numerically this has been realised by simply assuming that the disc particles are all twice as strongly bound to their host star. This is obviously a strong simplification of the effect of high-mass discs and more detailed investigations would be necessary in future. However, Fig. 4.11 shows that although the stronger binding naturally leads to a smaller disc-mass loss for the massive stars than before, the effect is only weak. Still the high-mass stars lose a significantly higher proportion of their disc mass than intermediate-mass stars.

#### 4.4.5. Discussion

In the previous sections it was stated that the results represent an upper limit for the destruction of discs by encounters in the ONC. In the following the underlying assumptions will be discussed in more detail and estimates for lower limits of the mass loss given.

The situation described above contains, like previous work, a contradiction – it was as-

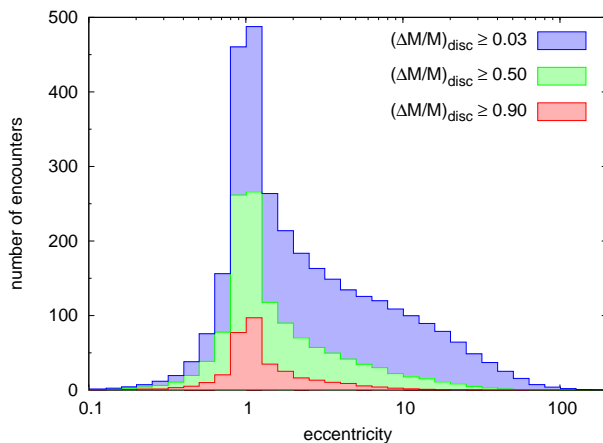


Figure 4.12.: Number of encounters as a function of the eccentricity (logarithmic bins), plotted for three different groups by means of disc-mass loss per encounter. The blue surface represents all encounters (see Section 4.4.2 for the definition of an encounter), the green those that removed at least 50 % of the disc-mass, while the red stands for the most destructive encounters that caused a disc-mass loss of at least 90 %.

sumed that each star is initially surrounded by a disc while at the same time the disc-mass loss was attributed to the perturbation of a disc-less star. For consistency the interaction should be calculated with both stars being surrounded by a disc. However, the reason not to do so is twofold: (i) encounters where both stars are surrounded by discs are less well investigated, and (ii) Pfalzner *et al.* (2005a) showed that the star-disc results can be generalised to disc-disc encounters as long as there is no mass exchange between the discs. In the case of a mass exchange, i.e. close encounters between star-disc systems, the discs can be replenished to some extent, which means that the disc-mass loss will be overestimated for the most perturbing events.

The effect of restricting all encounters to parabolic cases,  $\epsilon = 1$ , as done by using Eq. (4.6), is not as severe for an ONC-like cluster as could be assumed. Formation of persistent binaries ( $\epsilon < 1$ ) can be neglected as in this study it happens in less than 0.5 % of all encounters. However, transient binary systems (cf. Pfalzner & Olczak, 2007b), i.e. formation of bound states over a small number of orbits, does occur in 1/4 of all encounters. But most of these configurations are very eccentric, with only 10 % of all encounters having  $\epsilon < 0.8$ . The situation is more complicated for hyperbolic encounters,  $\epsilon > 1$ , where the disc-mass loss is lower due to the shorter interaction time of perturber and star-disc system. However, most encounters in the cluster simulations are parabolic or only mildly hyperbolic. This is shown in Fig. 4.12, where the number of encounters as a function of eccentricity is plotted for three different groups by means of disc-mass loss per encounter. Considering in the following

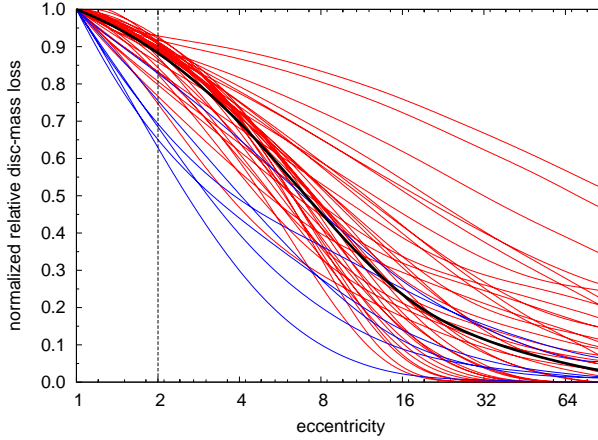


Figure 4.13.: Relative disc-mass loss normalised to the strict parabolic case ( $\epsilon = 1$ ) as a function of eccentricity for all star-disc simulations that have been performed (see Section 4.4.2 for the adopted parameter space). Blue lines mark simulations of relative perturber masses  $M_2/M_1 < 1$ , whereas red lines represent encounters with more massive perturbers,  $M_2/M_1 \geq 1$ . The median of the curves is represented by the thick solid black line. The vertical black dashed line marks  $\epsilon = 2$ , the upper range of the here adopted “pseudo-parabolic” encounter regime.

encounters with  $0.8 \leq \epsilon \leq 2.0$  as “pseudo-parabolic”, i.e. with a perturbing effect that is well described by Eq. (4.6),  $\sim 45\%$  of all encounters (the group with  $\Delta M_d/M_d \geq 0.03$ ) are pseudo-parabolic. In the case of strongly perturbing encounters,  $\sim 60\%$  are pseudo-parabolic for disc-mass losses larger than  $50\%$ , and even  $\sim 70\%$  for disc-mass losses above  $90\%$ .

The decision to extend the regime of “parabolic” encounters to  $\epsilon = 2$  is justified by Fig. 4.13. Here the relative disc-mass loss has been normalised to the strict parabolic case ( $\epsilon = 1$ ) as a function of eccentricity for all star-disc simulations that have been performed (see Section 4.4.2 for the adopted parameter space). One finds that encounters with  $\epsilon = 2$  in most cases remove at least  $80\%$  of the relative disc-mass loss that is removed in the strict parabolic case. Only for smaller relative perturber masses,  $M_2/M_1 < 1$ , the relative disc-mass loss for  $\epsilon = 2$  can decrease to  $60\%$  of the value at  $\epsilon = 1$ . The consequence of assuming only strict parabolic encounters in the present investigation has thus most probably a minor effect on the presented results for the low- and intermediate mass stars, that are mostly subject to few strong encounters causing substantial mass removal. However, in the case of high-mass stars there might be a significant overestimation, because here mainly the cumulative effect of many weak encounters (with perturbers of lower mass) acts destructive on the disc.

Another assumption addresses the alignment of discs. It is still an open question whether discs in clusters are in any way aligned and whether there is a preference for coplanar or

prograde encounters due to the common formation history of the stars and discs involved. If the coplanar, prograde encounters considered here are in any way favoured, the strong perturbations assumed in the present investigation would be common in an ONC-like cluster. However, in a cluster that is not highly flattened it seems rather unlikely that the encounter planes are aligned to a high degree. Therefore one would expect most encounters to be non-coplanar. However, Pfalzner *et al.* (2005b) showed that, as long as the inclination is not larger than  $45^\circ$ , the mass loss in the encounter is only slightly reduced in comparison to a coplanar encounter. Thus, if there is any preferred rotational axis in a cluster, as could be expected due to its rotation, a random distribution of inclinations would be excluded. Otherwise, if the orientation would be completely random, the disc-mass loss could be significantly overestimated in 3/4 of cases and would account for only about 1/4 of the encounter events in the cluster.

In this investigation it was assumed that in repeated encounters the relative disc-mass loss is the same. Though this seems to be in contrast to the prevailing view that an encounter “hardens” a disc, so that consecutive encounters become less effective in removing disc material, Pfalzner (2004) found that for equal mass perturbers the relative disc-mass loss in a second encounter was the same as in the first. It is important to note that the calculations of Pfalzner (2004) are ballistic particle simulations, neglecting the effects of viscosity. Some authors have shown that viscosity can have a large impact on disc evolution (e.g. Clarke & Pringle, 1993). However, Pfalzner *et al.* (2005a) have as well investigated the effect of viscosity on different disc parameters and found no significant differences neither in the mass loss nor in the density distribution.

Inevitably, three simplifications had to be applied which underestimate the disc-mass loss due to encounters. First, it was assumed that all encounters can be described as two-body processes. As would be expected, Umbreit (2005) found from three-body encounter simulations that the resulting discs are flatter and less massive than after similar two-body encounters with the same minimum encounter distance. However, since the calculation of the mass loss was obtained in each case with the gravitationally dominant perturber and the scenario of two nearly equally perturbing objects is very unlikely, additional contributions from lower-order perturbers should be minor. Second, the IMF has been generated with a cut-off at substellar masses ( $M \leq 0.08 M_\odot$ ), which means that potential low-mass perturbers have not been included in the simulations. However, this simplification should be as well uncritical because the disc-mass loss falls below 10% for mass ratios below 0.1, so the contribution from low-mass perturbers for intermediate to massive stars is negligible as long as they are not penetrating the disc. Finally, it has not been considered that a considerable proportion of the stars in the ONC are not single stars but binary systems. This third simplification is much harder to quantify and most probably has a non-negligible effect. Further studies would be

needed to see if binary systems would lead to a different disc destruction rate.

#### 4.4.6. Conclusion

The present investigation of the ONC, combining cluster simulations with encounter investigations, shows that potentially up to 20-25 % of the discs in the Trapezium Cluster could have been destroyed by encounters. The more sophisticated treatment of the disc-mass loss expected from repeated stellar encounters with massive perturbers implies that it is plausible that the 15-20% of discless stars observed in the Trapezium Cluster (Lada *et al.*, 2000) may, in a large fraction of cases, result from star-disc collisions. This is in contrast to earlier investigations, and the difference results from a much broader encounter data set for the disc-mass loss including massive perturbers and the evaluation of the *entire* encounter history of each star in the cluster. The central result of this study is that it is probably premature to dismiss encounters as an important destruction mechanism for discs in clusters.

It is found that the most massive bodies dominate the disc-mass loss, with significant interaction even beyond a separation of ten disc radii for a ONC-like entity. This is particularly so for the Trapezium Cluster, where some dozen massive stars are surrounded by hundreds of lighter bodies. Consequently, it is the upper end of a cluster's mass distribution that to a large degree determines the fate of the circumstellar discs in its vicinity and thus there are in principle two quantities that are mainly regulating the effect of stellar encounters on the mass-loss from protoplanetary discs: namely the local stellar density which determines the encounter probability, and the upper limit of the mass range, which affects the maximum strength of the perturbing force.

Consequently, it is shown that the relative disc-mass loss for intermediate-mass stars is less than for massive stars. If one assumes that the disc size scales with the stellar mass, the relative disc-mass loss is even lower for low-mass stars. However, if the disc size is independent of the stellar mass then low-mass stars have as well a higher relative disc-mass loss than intermediate-mass stars in accordance with Lada *et al.* (2006). In this case stars with  $3M_{\odot} \lesssim M_{\star} \lesssim 10M_{\odot}$  suffer the least disc-mass loss.

The reason for greater disc-mass loss of massive stars is twofold: First, high-mass stars are found preferentially in the cluster core (due to dynamical mass segregation) where the stellar density and thus encounter frequency is higher, and second, even in the same cluster region do the more massive stars suffer greater disc-mass loss than low-mass stars, a result that can be traced to the larger number of encounters suffered by these more massive stars. The gravitational focusing of low-mass stellar orbits by massive stars enhances the encounter rate between the massive star and other cluster members for any particular periastron separation. So not only for the ONC investigated here, but generally there should be more intermediate-mass stars than massive stars surrounded by discs in the inner regions of high-density clusters, pro-

vided they contain a sufficient number of massive stars. This prediction is vitally supported by observations of IC 348 (Lada *et al.*, 2006), NGC 2362 (Dahm & Hillenbrand, 2007), or the massive cluster NGC 6611 (Oliveira *et al.*, 2005), finding a larger fraction of discs around intermediate-mass stars than around more massive stars.

Interestingly, as the number of massive members in a stellar group seems to be correlated to its initial density (see Testi *et al.*, 1997; Bonnell *et al.*, 2004) and the IMF appears to be uniform for all Galactic environments of star-formation (e.g Kroupa *et al.*, 1993; Muench *et al.*, 2000; Kroupa, 2001), the dependency of the disc-mass loss due to encounters seems to be mainly reduced to one parameter, namely the density distribution of the considered stellar system. Whether the density of a stellar system is indeed the decisive parameter in terms of the effect of star-disc encounters will be addressed in Chapter 6.



# 5. Dynamical Imprints of Star-Disc Encounters in the ONC

## 5.1. Introduction

The main focus of this chapter is the question of whether there is direct *observational* evidence for encounters among star-disc systems in young clusters and for disc-mass loss due to encounters. It is difficult to distinguish observationally whether photoevaporation or gravitational interaction are responsible for the loss of (outer) discs. The reason is that in both cases interaction with a massive star is the most destructive process. Thus the observation of a decreased disc frequency in the cluster core, as derived in the previous section, does not allow one to favour either of the two mechanisms. The difficulty of tracing stellar encounters directly by observations is their short duration. However, an unambiguous imprint of an encounter among stars is the high velocity of a star which has been expelled in a close gravitational interaction, mostly as a result of a three-body encounter (see Heggie, 1975). Thus an analysis of the velocity distribution of a cluster is the key to finding candidates of close encounters between young stars.

In Section 5.2 results from a search for candidate stars of close encounters in the publicly available observational data of the ONC are presented. For this purpose the investigations of Jones & Walker (1988), Hillenbrand (1997), and Hillenbrand *et al.* (1998) have been reanalysed for stellar velocities and infrared excess. The basic properties of the ONC used for the numerical model have been described in Section 4.1. Based on these, theoretical estimates and observational data related to binary populations and encounters in the ONC are discussed in Sections 5.2.1 and Section 5.2.2. Afterwards, results from a numerical approach to this problem are presented (Section 5.3). Observational and numerical results are summarised and discussed in Section 5.4.

## 5.2. Observations

The search for candidate stars of close encounters from observational data concentrates on velocity surveys of Orion. There exists only one large data set of the ONC that provides veloc-

ity information for several hundred stars, the proper motion survey of Jones & Walker (1988). Fortunately, the same stars have been analysed by Hillenbrand *et al.* (1998) for infrared excess emission as an indicator of circumstellar material. They defined a quantity measuring the magnitude of the near-infrared excess,  $\Delta(I_C - K)$ ,

$$\Delta(I_C - K) = (I_C - K)_{\text{observed}} - 0.5A_V - (I_C - K)_{\text{photosphere}}, \quad (5.1)$$

where the first term is the observed  $I_C - K$  colour, the second term the contribution of reddening calculated from the extinction values derived from  $V - I_C$  colours as in Hillenbrand (1997), and the third term the contribution of the underlying stellar photosphere. This measure of the near-infrared excess,  $\Delta(I_C - K)$ , traces only the innermost ( $< 0.1$  AU) part of the circumstellar disc. Hence, the absence of such emission is not to be confused with a complete absence of a protoplanetary disc, yet is dependent on a number of parameters, such as disc accretion rate, inclination, inner hole, and stellar mass and radius (Hillenbrand *et al.*, 1998). However, in the following, stars that lack infrared excess emission will be referred to as “dis-less”, emphasising that these stars may be well surrounded by circumstellar material but do not show the typical infrared excess of a young star-disc system.

In addition, Hillenbrand (1997) has investigated stellar properties like mass and age. The investigation is based on optical photometric and spectroscopic data and covers only about half of the stellar population of the ONC, while the more embedded stars are not accessible at this wavelength. However, Hillenbrand (1997) states that the investigated stellar sample is representative of the entire population of the ONC. Masses and ages were derived from an HR diagram via comparison with theoretical pre-main-sequence evolutionary tracks. This method leaves some uncertainty as to the absolute stellar age ( $\sim 0.5$  dex, see Appendix B.2) and mass calibrations, with mass deviations of about factors of two and age differences of several Myr among different models. Additionally, photometric errors translate into uncertainties of the derived masses, but this is significant only for stars more massive than  $M \approx 1.5 M_{\odot}$ . However, all these sources of uncertainties are less relevant for the present investigation because (i) the stars of interest are of low mass as will be shown later, and (ii) the derived conclusions are based mainly on relative masses and ages.

The data of the three investigations described have been merged and stars for which measurements of proper motion or infrared excess are missing have been excluded, resulting in a database of 655 stars. In order to achieve the most secure distinction possible between stars with infrared excess and pure photospheric emission, the criterion of Sicilia-Aguilar *et al.* (2005b) has been adopted, excluding all stars that have an infrared excess  $\Delta(I_C - K)$  in the range  $0 < \Delta(I_C - K) < 0.5$ . A star is classified as dis-less if  $\Delta(I_C - K) \leq 0$ , or as a star-disc system if  $\Delta(I_C - K) \geq 0.5$ . This additional selection criterion reduces the sample of stars that have been used for this investigation to 405, among them 266 star-disc systems and 139 stars

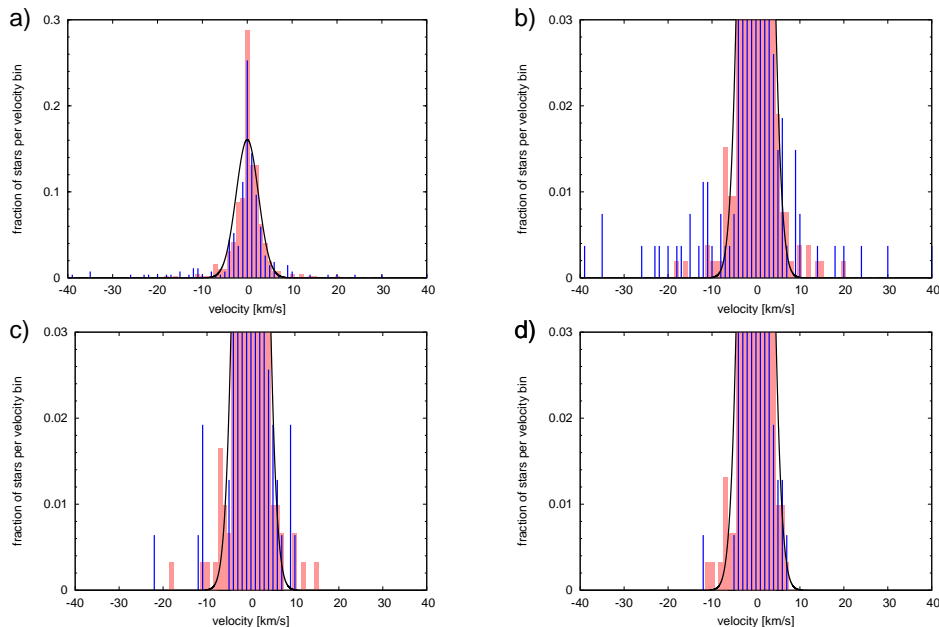


Figure 5.1: Velocity distribution from observational data, adopting a distance of 420 pc to the ONC (cf. Jeffries, 2007; Menten *et al.*, 2007). See text for details of its construction. The bin width is  $0.7 \text{ km s}^{-1}$ . The stars have been divided into two groups according to the disc signature  $\Delta(I_C - K)$  (see text): red boxes represent stars with IR-excess, blue lines represent stars with pure photospheric emission. For comparison a Gaussian with dispersion  $\sigma = \sigma_{\text{ID}}^{\text{JW}} = 2.5 \text{ km s}^{-1}$  (Jones & Walker, 1988) is superposed (black solid line). **a)** Complete sample of stars in the ONC with available proper motions from Jones & Walker (1988) and infrared excess from Hillenbrand *et al.* (1998). **b)** Like a), but zoomed into the lower part. **c)** Like b), but with restricted stellar ages (see text). **d)** Like b), but with restricted stellar ages and velocity errors as described in the text.

lacking any excess emission.

Fig. 5.1 shows the velocity distribution of stars with and without discs, adopting a distance of 420 pc to the ONC (cf. Jeffries, 2007; Menten *et al.*, 2007). The velocity distribution has been built by binning *each component* of the proper motion,  $\mu_x$  and  $\mu_y$ , of each star separately, not its total two-dimensional motion, or in other words by summing the Gaussian velocity distribution of each spacial direction,  $x$  and  $y$ , which again results in a Gaussian. The reason not to bin the total two-dimensional motion is the improvement of statistics due to the twice as large data set. For comparison, a Gaussian with a one-dimensional velocity dispersion  $\sigma = \sigma_{\text{ID}}^{\text{JW}} = 2.5 \text{ km s}^{-1}$ , as determined for the ONC by Jones & Walker (1988), is superimposed (dashed line). The distribution shows the expected features: At velocities  $\mu_{x,y} \lesssim 3\sigma_{\text{ID}}^{\text{JW}}$  the shape is approximately Gaussian, though a distinct peak at zero velocity is present. This

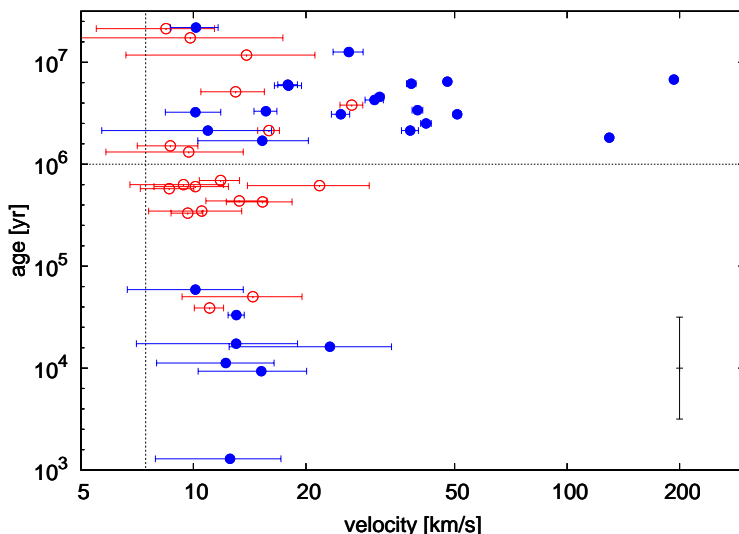


Figure 5.2.: Distribution of age and velocity of the high-velocity stars in the ONC, classified as star-disc systems (red open circles) and discless stars (blue filled circles). The mean age of the ONC,  $t = 1$  Myr, and the minimum one-dimensional velocity of the high-velocity sample,  $3\sigma_{\text{ID}}^{\text{JW}}$ , are indicated by the horizontal and vertical dashed line, respectively. The uncertainty of the determined ages of  $\sim 0.5$  dex (see Appendix B.2 for the derivation) is indicated by the vertical error bar. At high velocities the (horizontal) velocity error bars are smaller than the symbol size.

peak is only prominent for the  $x$ -components of the proper motion but is independent of the applied binning. One may suppose that this is an artifact of the plate reduction technique used by Jones & Walker (1988). At higher velocities,  $\mu_{x,y} \gtrsim 3\sigma_{\text{ID}}^{\text{JW}}$ , there is an overabundance of stars when compared with the theoretically expected Gaussian distribution. In this regime stars are not bound energetically to the cluster (see Binney & Tremaine, 1987, Eq. 8-3). In the following these stars will be referred to as “high-velocity stars”.

The number of high-velocity stars,  $N_{\text{hvs,obs}} = 50$ , is remarkably high, much higher than the theoretically expected  $N_{\text{hvs}} \lesssim 15$  (for a derivation see Section 5.2.2). In fact,  $N_{\text{hvs,obs}}$  should be even lower than the theoretical  $N_{\text{hvs}}$  because only about 1/5 of the ONC stellar population is covered by the observational data. The reason is most likely a contribution from foreground stars, which show large proper motions due to projection effects. In order to exclude probable foreground stars from the sample of ONC stars, the age as a function of the velocity of the high-velocity stars has been plotted in Fig. 5.2, again for the two groups of discless stars and star-disc systems. Two opposite trends are visible: The discless stars with ages  $t > 1$  Myr have a  $\sim 10$  times higher maximum velocity than younger ones ( $\sim 200 \text{ km s}^{-1}$  compared to

$\sim 20 \text{ km s}^{-1}$ ) and a twice as high mean velocity ( $\sim 30 \text{ km s}^{-1}$  compared to  $\sim 13 \text{ km s}^{-1}$ ). This strong correlation is likely due to a large fraction of foreground objects among the stars with ages  $t > 1 \text{ Myr}$ , and since this age boundary is consistent with the mean cluster age, it marks a conservative upper limit to the age of probable cluster members. Conversely, the star-disc systems are similarly distributed in both age groups, with comparable maximum and median velocities ( $\sim 25 \text{ km s}^{-1}$  and  $\sim 11 \text{ km s}^{-1}$ , respectively). However, *all* stars with ages  $t > 1 \text{ Myr}$  have been excluded in the further discussion for three reasons: (i) the age of these stars exceeds the simulated cluster age, so they are dynamically distinct, (ii) at least some of these stars might not be members of the ONC due to their high age (and velocity), and (iii) protoplanetary discs with ages  $t > 1 \text{ Myr}$  may be subject to significant evolution due to internal processes<sup>1</sup>, so that the effect of encounters could not be quantified.

Of the group of high-velocity stars younger than 1 Myr, the “probable high-velocity cluster members”, about half show disc signatures, the rest does not. The fact that stars with velocities of several tens of  $\text{km s}^{-1}$  are not present in this group is in accordance with dynamical estimates: the probability of both the generation and detection of stars with such high velocities is very low due to the need for a very close approach and short traverse of the cluster.

The uncertainties in the estimated ages of stars with and without infrared excess emission do not alter the fact that some of the youngest high-velocity stars lack infrared excess. This is noteworthy because in the early stages of stellar evolution one would expect accretion rates to be high and circumstellar material to be close enough to the star that significant excess emission can be detected. However, because the excess emission measured by  $\Delta(I_C - K)$  originates close to the stellar surface, it is strongly dependent on the geometry and orientation of the disc. A more robust and sensitive indicator of circumstellar discs is the  $K - L$  colour (Meyer *et al.*, 1997; Haisch *et al.*, 2000), tracing material out to radii of  $\sim 0.1 \text{ AU}$  (Haisch *et al.*, 2005). The “discless” stars,  $\Delta(I_C - K) \leq 0$ , have been thus cross-checked for excess emission at longer wavelengths,  $\Delta(K - L)$ . The results are shown in Table 5.1.

Two of the stars previously determined as “discless” do show a typical emission signature of warm circumstellar matter. Four high-velocity stars remain that lack infrared excess. It is not possible to determine whether the pure photospheric colours point to the absence of a circumstellar disc. This possibility will be discussed later.

The positions and velocity vectors of the selected probable high-velocity cluster members have been plotted in Fig. 5.3a. Two features are apparent: (i) Most high-velocity stars are concentrated in the inner tenths of a parsec around the most massive ONC member,  $\theta^1 \text{C Ori}$ ,

<sup>1</sup>According to studies of properties and evolution of protoplanetary discs in young clusters (e.g. Hillenbrand, 2005; Sicilia-Aguilar *et al.*, 2006), it is valid to assume that the protoplanetary discs in the ONC have been only marginally subject to internal disc processes. As such, it is assumed in the following that the effect of external processes on discs, i.e. photoevaporation and encounters, have not been masked by internal processes at the current age of the ONC.

ID <sup>a</sup>	$r^b$ [pc]	$\mu_x^c$ [km s <sup>-1</sup> ]	$\sigma_x$ [km s <sup>-1</sup> ]	$\mu_y$ [km s <sup>-1</sup> ]	$\sigma_y$ [km s <sup>-1</sup> ]	$p^d$ [%]	$j^e$ [mag]	$H$ [mag]	$K$ [mag]	$L$ [mag]	SpT <sup>f</sup>	$m^g$ [km s <sup>-1</sup> ]	log $t^h$ [yr]	exc <sup>i</sup>
JW 19	1.99	-12.2	4.2	0.2	2.2	84	12.98	12.26	11.87		M5.5	0.16	4.05	no
JW 45	1.12	-13.0	0.6	-0.8	0.8	0	8.83	8.28	8.05	7.89	K3	0.94	4.52	no
JW 505	0.10	-4.2	11.4	-22.8	8.8	93	12.33	11.65	11.18	10.65	M2	0.20	4.21	?
JW 510	0.36	-5.0	2.8	8.8	2.4	95	13.01	12.18	11.76	11.16	M5	0.14	4.77	yes
JW 559	0.19	-11.6	3.2	9.8	3.8	99	12.43	11.74	11.30	11.04	M5.5e	0.16	3.97	no
JW 569	0.24	-12.0	3.8	-3.6	3.4	92	12.47	11.58	11.00	10.14	M3.5	0.09	3.11	yes
JW 616	0.30	9.4	5.6	9.0	2.8	95	13.21	12.36	11.91	11.50	M3.5	0.15	4.24	no

<sup>a</sup>Stellar ID from Jones & Walker (1988)

<sup>b</sup>Projected distance from  $\theta^1$  C Ori.

<sup>c</sup>Proper motion and associated error.

<sup>d</sup>Probability of cluster membership.

<sup>e</sup>Apparent magnitude in specified band filter.

<sup>f</sup>Spectral type.

<sup>g</sup>Stellar mass.

<sup>h</sup>Stellar age.

<sup>i</sup>Detection of excess emission from  $K - L$  colour.

Table 5.1.: Properties of discless high-velocity stars in the ONC.

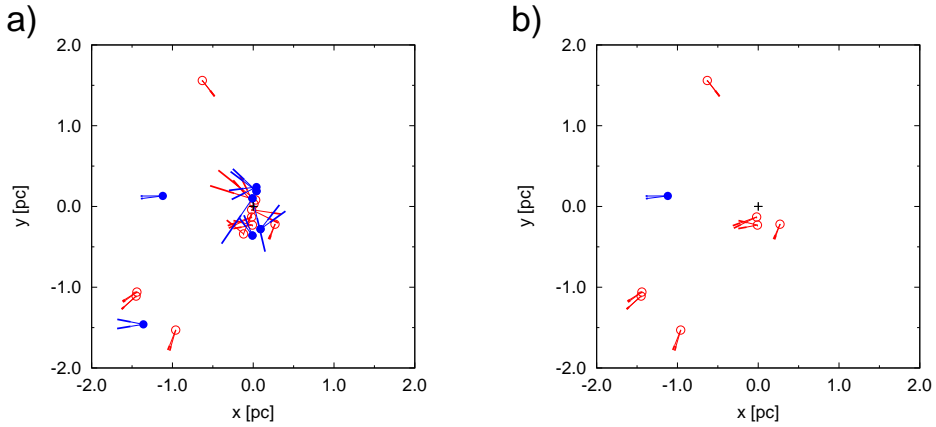


Figure 5.3.: Positions and velocities of high-velocity star-disc systems (red open circles) and discless stars (blue filled circles) in the ONC. The frames are centred on the most massive star,  $\theta^1$  Ori, which is marked by a cross. Thin lines indicate the distance (in pc) a star would have moved in a period of  $2 \cdot 10^4$  yr. Thick lines and the opening angle reflect the error of the magnitude and the direction of the proper motion, respectively. **a)** Sample of all high-velocity stars with ages  $< 1$  Myr. **b)** Restricted sample of high-velocity stars with ages  $< 1$  Myr: only stars fulfilling the constraints on the velocity errors as discussed in the text are shown.

and (ii) “outliers” are located more than 1 pc from the cluster centre with some stars moving in radial directions away from the cluster centre. Although one would expect the former, as most encounters usually happen in the dense cluster centre, there are two unexpected features: (i) The region between the cluster centre and outer cluster parts,  $0.4 \text{ pc} \lesssim r \lesssim 1.0 \text{ pc}$ , is devoid of high-velocity stars, and (ii) the velocity vectors of several stars in the outer cluster parts do not point away from the cluster centre (as if these stars had an encounter in the less dense cluster parts). In order to be confident that the encounter candidate stars are indeed high-velocity stars and not affected by observational uncertainties, the sample of high-velocity stars is restricted to maximum velocity errors of less than 30% or below  $2.0 \text{ km s}^{-1}$ . This reduces the number of high-velocity stars to a total of only eight, among them just one star without infrared excess, JW 45. The corresponding position-velocity diagram is shown in Fig. 5.3b (see also the corresponding velocity distribution in Fig. 5.1d). However, apart from the concentration of high-velocity stars close to the cluster centre, the same features as in Fig. 5.3a are apparent. The reason for the different central concentration is the strong acceleration of stars close to the cluster centre which results in large errors of the derived proper motions. Consequently the velocity error criterion preferentially excludes stars close to the cluster centre. The particular features will be addressed in Section 5.3, where the results

from numerical simulations of the dynamical model of the ONC is presented.

Because binaries can have a strong impact on the evolution of cluster dynamics, the “standard” cluster model of the ONC, as discussed in Section 4.2, is extended here by the treatment of binaries. In the next section a summary of the main properties of the ONC binary population that determine the model setup is given.

### 5.2.1. Binaries in the ONC

In the ONC the binary rate for solar-type stars is  $\sim 50\%$ . From observations alone there is only a very limited knowledge of the distribution of binary periods, eccentricities or mass ratios of the ONC. However, combining observational data and numerical simulations, the initial properties of the primordial binary population in a stellar aggregate have been modelled by Kroupa (1995b) and Kouwenhoven *et al.* (2007). These can be applied to some degree to the ONC.

The investigation of Kroupa (1995b) is based on the properties of the Taurus-Auriga binary population and constructs the primordial population by *inverse dynamical population synthesis* (see Kroupa, 1995a) and *pre-main-sequence eigenevolution*. The resulting distributions are approximately the log-normal period distribution  $f_P(P)$  of Duquennoy & Mayor (1991),

$$f_P(P) \propto \exp \left[ -\frac{(\log P - \mu_P)^2}{2\sigma_P^2} \right], \quad (5.2)$$

with mean  $\mu_P \equiv \overline{\log P} = 4.8$  and standard deviation  $\sigma_P \equiv \sigma_{\log P} = 2.3$ ,  $P$  in days, a thermally relaxed eccentricity distribution  $f_e(e)$ ,

$$f_e(e) = 2e, \quad 0 \leq e < 1, \quad (5.3)$$

and a mass ratio distribution  $f_q(q)$  obtained by random pairing of stars,

$$f_q(q) \propto q^{\gamma_q}, \quad (5.4)$$

where  $q = M_2/M_1$ ,  $M_1$  the primary,  $M_2$  the secondary mass, and  $\gamma_q = \alpha$ ,  $\alpha$  the slope of the mass function of the stellar system.

The log-normal period distribution  $f_P(P)$  results in an approximately log-normal semi-major axis distribution  $f_a(a)$ , the shape of which is slightly dependent on the distribution over binary mass  $M$  (Kouwenhoven *et al.*, 2007):

$$\overline{\log a} = \frac{2}{3} \overline{\log P} - \frac{1}{3} \log \left( \frac{4\pi}{2GM} \right), \quad \sigma_{\log a} = \frac{2}{3} \sigma_{\log P}. \quad (5.5)$$

Kouwenhoven *et al.* (2007) have analysed the current binary population of Scorpius OB2, under the reasonable assumption that it is still close to its primordial state. Accounting for different observational biases by means of comparison with simulated observations of model associations, they recovered a somewhat different primordial binary population than Kroupa (1995b): The semi-major axis distribution of Sco OB2 is most consistent with a flat distribution in logarithmic space, and is equivalent to

$$f_a(a) \propto a^{\gamma_a}, \quad a_{\min} \leq a \leq a_{\max}, \quad (5.6)$$

with  $a_{\min} \approx 5 R_{\odot}$ ,  $a_{\max} \approx 5 \cdot 10^6 R_{\odot}$ , and  $\gamma_a = -1$ , which is also known as Öpik's law (Öpik, 1924). The eccentricity distribution could not be well constrained, but the observations are consistent with a thermal distribution, given by Eq. (5.3). Unlike Kroupa (1995b), Kouwenhoven *et al.* (2007) find a power law dependence of the mass ratio distribution with  $\gamma_q \approx -0.4$ , which is much flatter than  $\gamma_q = \alpha$  (see Section 2.4 and Eq. (2.17)), and favours massive companions for massive stars.

The model of Kouwenhoven *et al.* (2007) seems more applicable for the present investigation, as observational studies of the ONC favour a flat distribution of the semi-major axes (e.g. Padgett *et al.*, 1997; Reipurth *et al.*, 2007). Theoretical considerations based on three-body encounters give similar results (Valtonen, 1997).

A thermal eccentricity distribution is expected from energy equipartition as a result of multiple soft encounters (Heggie, 1975) and is also found from observations, though only for binaries with separations  $a \gtrsim 10\text{-}50$  AU. Very close systems are subject to secularisation due to tidal effects occurring during stellar evolution (Duquennoy & Mayor, 1991; Mathieu, 1994).

The shape of the observed mass ratio distribution is not well constrained by observations. However, to a good approximation the mass ratio distribution can be described by a power law as given by Eq. (5.4) over a wide mass range (e.g. Trimble, 1990; Malkov & Zinnecker, 2001; Rucinski, 2001; Shatsky & Tokovinin, 2002; Valtonen, 2004). A single mass ratio distribution for primordial binaries as given by Eq. (5.4) with  $\gamma_q = -0.4$  as derived by Kouwenhoven *et al.* (2007) is thus favoured for the present investigation.

Binaries have strong effects on the overall cluster dynamics mainly through close interactions with single stars or other multiples. In the following the typical encounters that could generate high-velocity stars are estimated.

### 5.2.2. Three-body encounters in the ONC

As is well known, the non-hierarchical motion of three bodies, known as the three-body problem, has no analytical solution, and the chaotic motion of the members can only be

investigated numerically in a statistical manner (see Valtonen & Mikkola, 1991). In her study of triple systems with negative total energy, Anosova (1986) found that about 95 % of three-body systems decay after a close triple approach of the components. In most cases ( $\sim 80$  %), ejection leads to escape, but can also result in the formation of a hierarchical triple system, with one body in an extended orbit. The lowest mass member has the highest probability of being ejected, about 80 %.

In the following it is assumed that high-velocity stars are typically generated in triple systems with negative total energy. This assumption will be justified later in this section. If the motion has not been significantly perturbed since the encounter, one can draw conclusions about the underlying encounter parameters from the dynamics of the ejected body. In the case of the ONC, it is valid to assume that high-velocity stars with velocities  $v \geq 3\sigma_{3D}^{JW} \approx 13 \text{ km s}^{-1}$  are effectively unperturbed before they escape from the cluster (see Appendix C.1). Then the time to reach the outskirts of the cluster is  $t_{\text{esc}} \approx R/v \lesssim 0.2 \text{ Myr}$ .

For a crude estimate of the compactness of the three-body system (with negative total energy) from which a member is ejected with  $v \geq 3\sigma_{3D}^{JW}$ , the scaling of the median escape speed from Sterzik & Durisen (1995) is evaluated,

$$\langle v_{\text{esc}} \rangle \approx \frac{1}{2} \left( \frac{|E_0|}{\langle m_{\text{esc}} \rangle} \right), \quad (5.7)$$

where  $\langle m_{\text{esc}} \rangle$  denotes a weighted mean of the escaped particle masses,  $|E_0| \propto M_{\text{tot}}^2/R$  is the total system energy, and  $M_{\text{tot}}$  and  $R$  are the total mass and the scale length of the system.

It is assumed that the encounter occurred in the dense Trapezium Cluster where it is most probable (see Fig. 4 of Pfalzner *et al.*, 2006). Due to mass segregation of the cluster, the mass of the most massive component of the three-body system is likely to be several times the mean stellar mass in the ONC;  $M_{\text{tot}} = 4 M_{\odot}$  is thus adopted for the system mass. The mass of the ejected body is assumed to be half the mean stellar mass,  $\langle m_{\text{esc}} \rangle = 0.25 M_{\odot}$ . With these assumptions one obtains  $R \lesssim 100 \text{ AU}$  for the scale length of the system. However, the minimum approach which eventually leads to an ejection will be much closer. Since the disc radius of a low-mass star is about  $r_d \approx 100 \text{ AU}$ , the ejected component can lose more than 90 % of the disc mass (see Table 3 of Olczak *et al.*, 2006).

In the beginning of this section it was assumed that triple systems that generate high-velocity stars have negative total energy. In Appendix C.2 it is shown that this is a valid assumption if the ejected high-velocity stars do not exceed velocities of a few tens of  $\text{km s}^{-1}$ . In fact, all of the high-velocity stars from numerical simulations and observational data do not show higher velocities. A detailed analysis of the numerical simulations shows that in all cases the encounter-generated high-velocity stars are the lowest mass component ejected from a three-body system with a massive tight binary ( $M_{\text{bin}} \gtrsim 20 M_{\odot}$ ,  $a_{\text{bin}} \lesssim 50 \text{ AU}$ ), leaving

on a nearly parabolic orbit relative to one of the binary components. It is thus justified to conclude that the triple systems which generated the observed low-mass high-velocity stars must have been bound as well.

How many such encounters does one expect in the ONC? For simplicity, the three-body interaction is assumed to result from a single-binary encounter, where the binary has a semi-major axis  $a \lesssim 100$  AU. As a volume relevant for close encounters the Trapezium Cluster is considered. Referring to Eq. (C.1) the time scale for a three-body encounter at 100 AU is  $t_{\text{enc},100\text{AU}} \approx 10$  Myr. Since the time the star remains in the cluster volume is  $t_{\text{esc}} \lesssim 0.2$  Myr, the probability of the detection of a high-velocity star is  $P_{\text{hvs}} \approx t_{\text{esc}}/t_{\text{enc},100\text{AU}} \lesssim 0.02$ . Knowing the number of stars located in the Trapezium Cluster,  $N_{\text{TC}} \approx 750$ , one expects  $N_{\text{hvs}} \approx P_{\text{hvs}} N_{\text{TC}} \lesssim 15$  high-velocity stars in the ONC.

In summary, high-velocity stars with velocities  $v \geq 3\sigma_{3\text{D}}^{\text{JW}}$  (or velocity components  $v_{x,y,z} \geq 3\sigma_{1\text{D}}^{\text{JW}}$ ) have most probably experienced exactly one close ( $\lesssim 100$  AU), disruptive encounter in the cluster centre and leave the cluster on a radial trajectory, i.e. with the velocity vector pointing away from the cluster centre, preserving the dynamical information of the encounter. About one dozen such stars in the ONC are expected.

In the following the observational data and theoretical estimates will be compared with numerical simulations of a dynamical model of the ONC.

## 5.3. Numerical Simulations

The basic dynamical model of the ONC used here has been described in Section 4.2. For the present investigation additional effects like a varying background potential and a population of primordial binaries have been included, that will be discussed later on. A set of 20 runs with different random configurations of positions and velocities from the given distributions have been performed to establish a statistically robust database. Unless explicitly declared otherwise the presented results refer to the whole set of runs. The reason to extend the basic model of the ONC is to compare the velocity distribution to the observational data. Both the background potential and primordial binaries have a large impact on the resulting velocity distribution. However, for comparison and analysis of the contribution of the background potential and primordial binaries, also simulations of a single particle model, a single particle model with a background potential, and a cluster with a primordial binary population but without a background potential have been performed.

### 5.3.1. Construction of the Numerical Model

A background potential increases the cluster virial mass and thus results in a higher velocity dispersion (cf. Eq. (2.1)). In the simulations the background potential is represented by a

Plummer sphere,

$$\rho(r) = \frac{3M}{4\pi a^3} \frac{1}{(1 + \frac{r^2}{a^2})^{5/2}}, \quad (5.8)$$

with mass  $M$  and characteristic length scale  $a$ . The Plummer sphere is set up with  $6000 M_{\odot}$  (see Section 4.1 for an estimate of the initial gas mass in the ONC) initially and a mass loss rate  $\dot{M} = 4000 M_{\odot} \text{ Myr}^{-1}$ . Due to the continuous mass loss  $2000 M_{\odot}$  of gas is left after 1 Myr. The exact time scale and time dependency of the mass loss is not crucial, as long as the gas expulsion time scale is of the order of the dynamical time scale of the system,  $t_{\text{exp}} \approx t_{\text{dyn}}$ , which appears to be the case for the ONC (cf. Section 4.1). The length scale is set to  $a = 0.6$  pc to match the observed velocity dispersion at a simulation time of  $t_{\text{sim}} = 1$  Myr.

The effect of primordial binaries is more complicated. The interactions of binaries and single stars or other binaries have the potential to change the velocity distribution much more than a single star model. In particular, three body encounters between singles and binaries usually lead to the expulsion of the lowest mass member from the small  $N$ -body system with a high velocity. This mechanism is especially important for the high-velocity fraction of particles of interest in this study (see Section 5.2.2).

A series of simulations with the models of Kroupa (1995b) and Kouwenhoven *et al.* (2007) has been set up, finding that results do not depend on the choice of one particular model. The initial binary frequency was chosen to be 75%. Although the observed binary frequency in the ONC is  $\sim 50\%$ , it is necessary to start with a higher binary rate as about one third of the binaries are destroyed within the first 1 Myr due to dynamical evolution.

In terms of global cluster dynamics, the new model with a background potential and primordial binaries provides a much better fit to the ONC data than the previous single star model without background potential. This is illustrated by means of the time-evolution of the three-dimensional velocity dispersion of both models in Fig. 5.4. In the previous model there was not enough mass confined in the cluster to reproduce the observed velocity dispersion of the ONC,  $\sigma_{3D}^{\text{JW}} = 4.3 \text{ km s}^{-1}$ , at  $\sim 1$  Myr. The new model gives a much better result. The continuous, steep falloff after  $\sim 0.2$  Myr is due to the response of the stellar system to the gas expulsion. In the following, results of numerical simulations based on the new dynamical model of the ONC will be discussed.

### 5.3.2. Results of the Numerical Simulations

As demonstrated in Olczak *et al.* (2006), Pfalzner *et al.* (2006), and Pfalzner & Olczak (2007a), stellar encounters in dense clusters can lead to significant transport of mass and angular momentum in protoplanetary discs. In the present investigation Eq. (1) from Pfalzner *et al.* (2006) (which corresponds to Eq. (4.6)) has been used to keep track of the disc-mass loss of each star due to encounters. The estimate of the accumulated disc-mass loss is an

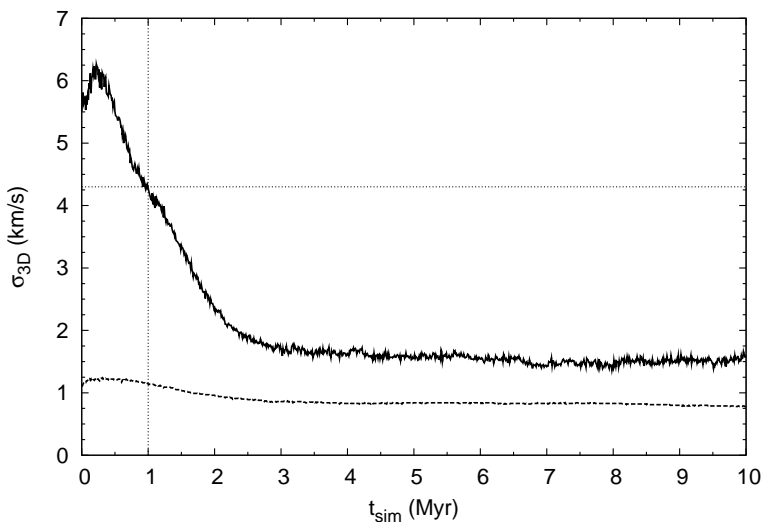


Figure 5.4.: Three-dimensional velocity dispersion as a function of time for the previous pure single star model (dashed line) and the new numerical model of the ONC with time-variable background potential and primordial binaries (solid line). The dotted horizontal line marks the three-dimensional velocity dispersion from Jones & Walker (1988),  $\sigma_{3D}^{JW} = 4.3 \text{ km s}^{-1}$ , the vertical dotted line marks the mean age of the ONC,  $t_{\text{ONC}} = 1 \text{ Myr}$ .

upper limit because the underlying formula is only valid for co-planar, prograde encounters, which are the most perturbing. A simplified prescription assigns stars into one of two distinct groups: if the relative disc-mass loss exceeds 90% of the initial disc mass, stars are marked as “discless”; otherwise they are termed “star-disc systems”. This approach is justified by the interplay of three effects: (i) A disc-mass loss of this order lowers the density in the disc significantly, in particular in the outer parts; the disc size decreases. (ii) The accompanying angular momentum loss enhances accretion of the extant material onto the star (Pfalzner, 2006). This leads temporarily to an increase of the infrared excess but soon fades after a short intense accretion phase (Pfalzner *et al.*, 2008). (iii) The loose distribution of circumstellar matter lowers the shielding of the disc midplane against photoevaporation. The interplay of these effects leads to a fast dispersal of the disc material. From the observational point of view, the corresponding star would show pure photospheric emission on the order of some  $10^3 \text{ yr}$  after the encounter.

In Fig. 5.5 the velocity distribution of cluster stars is shown after 1 Myr of evolution. This is done separately for discless stars and star-disc systems. For comparison with the observational data presented in Fig. 5.1c, separate velocity distributions of two spacial directions (here  $x$  and  $y$ ) have been added to mimic the distribution of proper motion data. Unless in

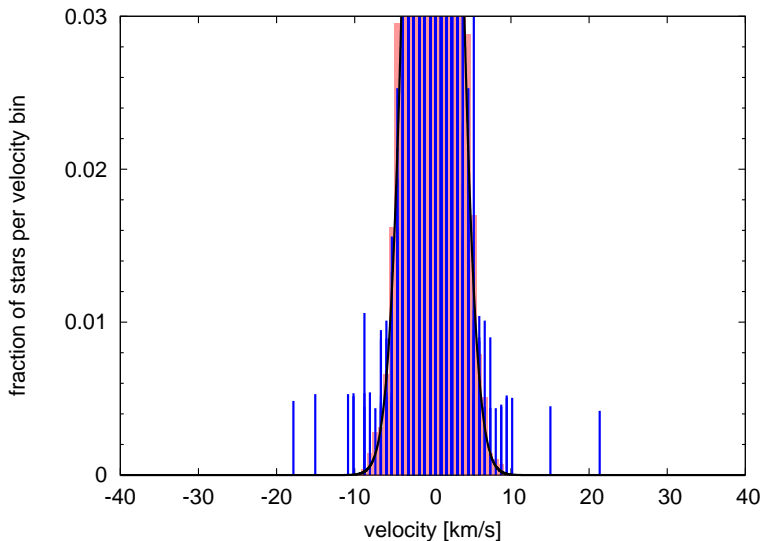


Figure 5.5.: Velocity distribution of cluster stars from simulations. The construction of the distribution is described in the text. The bin width is  $0.7 \text{ km s}^{-1}$ . The stars have been divided into two groups according to their extant disc mass (see text): red boxes represent star-disc systems, blue lines represent discless stars. For comparison a Gaussian with dispersion  $\sigma = \sigma_{\text{ID}}^{\text{JW}} = 2.5 \text{ km s}^{-1}$  is superposed (black solid line).

wide systems, primaries and secondaries could not have been resolved by Jones & Walker (1988) who worked with seeing-limited images. So the presence of binaries in the numerical simulations requires a special treatment of velocities. Accounting for unequal mass components and nebulosity, a minimum separation of 1000 AU (corresponding to  $\sim 2.5''$ ; see Mayne & Naylor, 2008, and references therein) has been adopted for the visual resolution of a binary system. For closer systems, only the primary component is taken into account and the centre-of-mass velocity of the system is assigned. For wider systems, both components are treated as single stars. This prescription is simple and rough but appropriate to avoid the inclusion of large velocity components of tight binaries.

The velocity distribution shows common features with Fig. 5.1c, which was obtained from observational data: the bulk of the stars forms a relaxed system which manifests in the approximate Gaussian velocity distribution with a characteristic velocity dispersion  $\sigma = \sigma_{\text{ID}}^{\text{JW}}$ . Moreover, a small fraction of stars exists with much higher velocities  $v_{x,y} \geq 3\sigma_{\text{ID}}^{\text{JW}}$ , the previously described “high-velocity stars”.

The velocity distributions of stars that have lost their disc due to close encounters and those that have retained their disc differ. The discless population consists of a larger fraction of high-velocity stars, while the width of the Gaussian part is similar. This feature is in

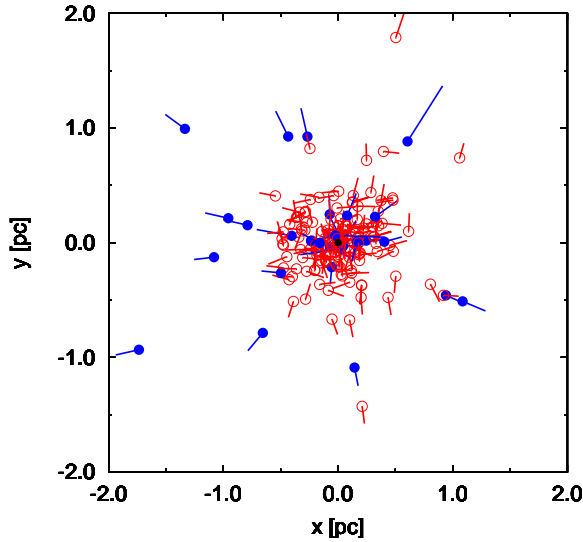


Figure 5.6.: Positions and velocities of high-velocity star-disc systems (red open circles) and discless stars (blue filled circles) from cluster simulations. The frame is centred on the cluster centre. The lines indicate the distance (in pc) a star would have moved in a period of  $2 \cdot 10^4$  yr.

agreement with expectations: High-velocity stars are usually the lowest mass members of temporary few-body systems which are expelled after a close encounter (see Section 5.2.2). The close passage and large mass of the perturber results in a significant removal of disc material (Pfalzner *et al.*, 2006).

In analogy to Fig. 5.3, positions and velocities of high-velocity stars from the numerical simulations are displayed in Fig. 5.6. Here the great advantage of numerical simulations becomes apparent: several runs of the same model can improve statistics far enough to produce prominent features where only weak signatures in observational data are found. The dynamical model of the ONC reproduces the observed features: As expected, most stars are concentrated in the inner tenth parsecs around the cluster centre, while several stars are located in the outer cluster parts, moving in radial directions from the cluster centre. However, the same two unexpected features as in the observations are found, namely that (i) the region between the cluster centre and the outer cluster parts is underpopulated by high-velocity stars, and (ii) the velocity vectors of a fraction of stars in the outer cluster parts do not point away from the cluster centre. High-velocity stars that leave the cluster on a track in radial direction from the cluster centre, i.e. with the velocity vector pointing away from the cluster core with radius  $R_{\text{in}} \approx 0.1$  pc, will be referred to as “radial escapers”, while high-velocity stars that do not match this condition will be called “orbital escapers”. In the following the choice of the

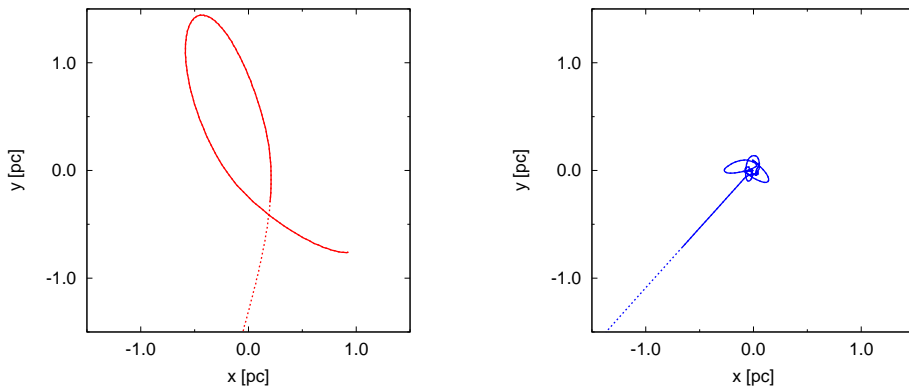


Figure 5.7.: Tracks of two high-velocity stars from simulations. The cross marks the cluster centre. The solid line marks the trajectory up to 1 Myr, the dotted line represents later times. **a)** Star on a wide orbit around the cluster centre, escaping from the cluster after a close passage of the cluster centre. **b)** Star escaping after multiple passages of the cluster centre and a final close encounter.

terminology will be explained.

In contrast to observations it is possible to trace the history of these stars in the simulation; this gives us the opportunity to investigate the reason for this strange configuration. As will be seen, (i) is a consequence of (ii), thus that one will be discussed first. In Fig. 5.7 two exemplary tracks of stars in the outer cluster parts are displayed, those of an orbital (Fig. 5.7a) and a radial escaper (Fig. 5.7b). It is evident that the phase spaces of the two stars are completely different. The radial escaper was originally located close to the cluster centre, experienced several encounters in multiple passages of the cluster centre and was finally expelled in a close three body encounter. After the ejection, it is moving on a track in a radial direction from the cluster centre, i.e. with the velocity vector pointing away from the cluster core. The orbital escaper stems from the outer cluster parts, passed on a non-closed orbit at a minimum distance of some tenths of a parsec around the cluster centre (without significant encounters) and was accelerated sufficiently by the central mass to leave the cluster on a hyperbolic orbit. Most of the time its velocity vector is *not* pointing away from the cluster core. This is most evident at large distances from the cluster centre. Only at the two short periods of cluster centre passage, i.e. when the radius vector is approximately normal to the velocity vector, the determination of the direction of motion is eventually not sufficient to discriminate between a radial and orbital escaper. The fact that the orbital escaper is leaving the cluster although it was initially energetically (but only weakly) bound to the cluster is due to a varying clus-

ter potential on a time scale shorter than its revolution around the cluster centre.<sup>2</sup> The main sources of the potential variation are mass segregation and the evaporation of (preferentially low-mass) cluster stars. Consequently the orbital escaper is accelerated more strongly after the second passage of the cluster centre and is less decelerated in the outer parts due to the lower total cluster mass and more extended cluster potential.

The existence of two different classes of tracks explains why the region between the cluster centre and the outer cluster parts is devoid of high-velocity stars. Radial escapers leave the cluster on a very short time scale, while orbital escapers reside for much longer in the vicinity of the cluster centre due to their wide non-closed orbits. Hence the disjoint spacial groupings of stars after 1 Myr of cluster evolution are the consequence of disjoint sets of initial phase space volumes.

From the simulations it is found that the distinct dynamics of the two exemplary high-velocity stars characterise *in general* the dynamics of radial and orbital escapers: they belong to dynamically distinct groups. Moreover, the two groups as well can be separated due to their disc properties: a large fraction of radial escapers is discless, while most orbital escapers are star-disc systems. This *morphological* distinction is a consequence of the dynamical bisection. The morphological bisection translates observationally into a photometrical bisection, i.e. the stars would be divided into two groups according to the presence of excess emission. Such a trend, though only weak, is also present in the observational data.

In Fig. 5.3b, the three isolated stars with excess emission are identified as orbital escapers. The situation is more difficult for the two stars with excess emission immediately below the cluster centre. As mentioned above, stars close to the cluster centre cannot be uniquely identified as radial or orbital escapers from the direction of motion alone. Moreover, only two-dimensional spacial and velocity information is present, so the true distances to the cluster centre and velocities are not known. If the projected distance and true distance to the cluster centre differ only slightly for both stars, then the more distant ( $\sim 0.25$  pc) would be classified as a probable orbital escaper. The reason is that due to its proximity to the cluster centre and relatively low velocity this star will be accelerated and deflected by the central cluster mass and pass on a curved trajectory. When passing the cluster outskirts, its direction of motion would not point away from the cluster core and thus it would be identified as an orbital escaper according to the classification scheme. Of course, one cannot exclude the possibility that this star was ejected in a three-body encounter, although it could not be classified as a radial escaper due to its predicted trajectory. For the other star a classification as a radial escaper seems more appropriate. If, on the contrary, the true distance is much larger than the projected distance for both stars, they would be classified as orbital escapers. However, one can only speculate about the dynamical origin of the two stars. The special case of the two

<sup>2</sup>The time scale of the potential variation is related to the crossing time of the cluster,  $t_{\text{cr}} \approx 0.5$  Myr, while the time scale of revolution is approximately the cluster age,  $t_{\text{ONC}} \approx 1$  Myr, which is about twice as large.

close-by stars with excess emission in the lower left will be discussed below. The only star without excess emission (JW 45) seems to have been expelled very close ( $< 0.13$  pc) to the cluster centre and is thus classified as a radial escaper. If thus, conversely to the previous arguments, the lack of excess emission is interpreted as an indicator of the absence of a disc, then this star provides evidence for encounter-triggered disc destruction. The signature of disc material of the other stars is - as far as a classification is possible - in accordance with the numerical results and thus supports this view.

The two close-by stars at approximately  $(-1.5 \text{ pc}, -1.0 \text{ pc})$  in Fig. 5.3, JW 3 and JW 4, seem to form a binary. Though their separation of about  $10^4$  AU is large, the remarkably similar proper motions and radial velocity ( $v_r^{\text{JW}3} = 29.1 \text{ km s}^{-1}$ ,  $v_r^{\text{JW}4} = 31.6 \text{ km s}^{-1}$ ; Stassun *et al.*, 1999), age, and infrared excess strongly support the assumption of a physical pair - at least in the past. If this pair was expelled as a binary from a four-body encounter, than this must have occurred less than 0.1 Myr ago (accounting for the actual distance from the cluster centre, the velocity and the deceleration by the interior cluster mass). The difference in proper motion of the two stars corresponds to a distance of  $\sim (4 \pm 2) \cdot 10^4$  AU, in good agreement with the observed projected separation. Due to the direction of motion, the two stars are classified as radial escapers. The expulsion of binaries from close four-body encounters in the simulations, though a rare event (9 events from the 20 runs), usually does not lead to a significant disc-mass loss of the individual stars. This again is in good agreement with the observational data. Thus the excess emission of the binary radial escaper does not contradict the correlation of the dynamical and the photometric classification, which in the case of single stars shows that in most cases radial escapers are discless and orbital escapers are found preferentially among star-disc systems.

The general difference of the orbits of discless stars and star-disc systems is represented in Fig. 5.8. The minimum distance of star-disc systems to the cluster centre,  $d_{\text{min}}$ , is clearly a linear function of the initial specific angular momentum,  $l_0$  (relative to the cluster centre). A linear least squares fit results in a slope  $\alpha$  with a small standard error  $\Delta\alpha$ ,  $\alpha = (0.902 \pm 0.044) \text{ s km}^{-1}$  ( $\Delta\alpha/\alpha = 0.048$ ). This means that  $l_0$  is conserved - a consequence of the wide orbit around the cluster centre without strong, abrupt perturbations from single stars. On the contrary, discless stars show a much wider, not clearly correlated distribution of  $d_{\text{min}}$  due to angular momentum exchange in close encounters in the cluster centre. Here the slope  $\beta$  of the linear best-fit has a large standard error  $\Delta\beta$ ,  $\beta = (0.571 \pm 0.127) \text{ s km}^{-1}$  ( $\Delta\beta/\beta = 0.222$ ). Those star-disc systems with lower  $l_0$  and  $d_{\text{min}}$  populating the discless regime are components of binaries.

The distinct dynamics are even more evident from Fig. 5.9: here the ratio of the actual (at 1 Myr) and initial specific angular momentum,  $l_{\text{now}}/l_0$ , as a function of the initial specific angular momentum,  $l_0$ , is shown. Star-disc systems are concentrated nearly symmetrically

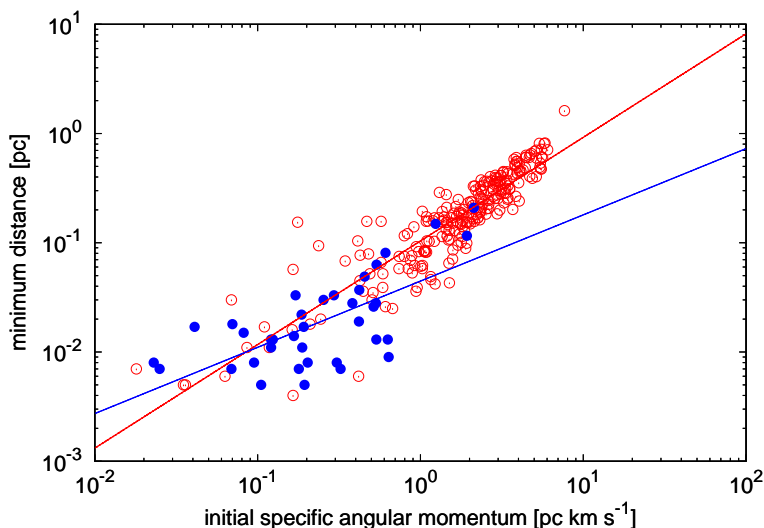


Figure 5.8.: Minimum distance of the high-velocity stars to the cluster centre,  $d_{\min}$ , as a function of the initial specific angular momentum,  $l_0$  (relative to the cluster centre). Star-disc systems are marked by red open, discless stars by blue filled circles. Linear best-fits of both populations, star-disc systems (red line) and discless stars (blue line), have been included (quantitative results are discussed in the text).

around  $l_{\text{now}}/l_0 = 1$ , while for most discless stars  $l_{\text{now}}/l_0 > 1$ , and even up to several tens. The increase of angular momentum of the discless stars *in relation to the cluster centre* can be explained as follows: Single stars gain a large amount of angular momentum in a close triple encounter (Valtonen *et al.*, 2005), and leave on straight radial tracks after breakup. Since these encounters occur preferentially close to the cluster centre, on average the angular momentum relative to the cluster centre is also highly increased. The raise of  $l_{\text{now}}/l_0$  with lower  $l_0$  is given by the fact that close encounters are more probable for stars with lower  $l_0$ , which in turn lead to a higher gain in angular momentum.

The additional components in the numerical model of the ONC - a background potential and primordial binaries - have different effects on the sample of high-velocity stars. By comparing with results of the simulations without either one or both additional components, it is found that (i) the inclusion of primordial binaries has the effect of increasing the number of discless stars (due to a larger number of encounters) and to increase the maximum velocity of the high-velocity stars (due to a higher probability of closer encounters), (ii) a background potential reduces the number of discless stars and reduces the maximum velocity of the high-velocity stars, because the higher velocity dispersion of the stars reduces the probability of close encounters. The combination of both as in the present model does not cancel out the

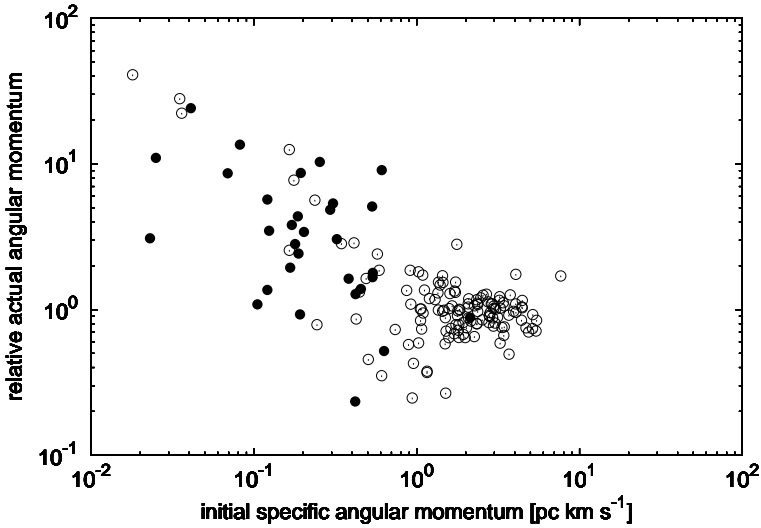


Figure 5.9.: Relative actual angular momentum of the high-velocity stars,  $I_{\text{now}}/I_0$ , as a function of the initial specific angular momentum  $l_0$  (relative to the cluster centre). Star-disc systems are marked by open, discless stars by filled circles.

positive effect of the binaries and thus results in a *higher* number of discless stars and a higher maximum velocity of the high-velocity stars than would result from a single star model.

## 5.4. Confronting Observations and Simulations

Combining observational data and numerical simulations, it has been shown that even after 1 Myr of dynamical evolution a cluster of the size and density of the ONC is still dynamically active. Young stars, preferentially of low-mass, are expelled in close  $N$ -body encounters, losing a large fraction of their circumstellar matter.

The encounters are in most cases interactions with massive stars in the cluster centre. This finding highlights the significant effect that encounters in (massive) young stellar clusters can have on the evolution of protoplanetary discs. This is even more evident if one addresses not only the effect on the mass, but the even stronger effect on the angular momentum of the disc as shown in previous investigations (Pfalzner, 2006; Pfalzner & Olczak, 2007a).

Using the observational data from Jones & Walker (1988) it is shown (Fig. 5.1c) that in the ONC there is a small population of stars with proper motions  $\mu_{x,y}$  larger than three times the one-dimensional velocity dispersion of the cluster,  $\mu_{x,y} \gtrsim 7.5 \text{ km s}^{-1}$ .

From numerical simulations it is found that the so-called “high-velocity stars” form two

dynamically disjoint groups. One group is composed of stars expelled in a close encounter, moving on radial tracks directly outward from the cluster centre, termed “radial escapers”. The other contains unperturbed stars running on wide, non-closed orbits around the cluster centre (on average with lower velocities), termed “orbital escapers”. The dynamical state of the stars has its origin in their initial phase space location: radial escapers are initially located close to the cluster centre ( $r \lesssim 0.3$  pc) and characterised by a low angular momentum (relative to the cluster centre). In contrast, orbital escapers were formed in the outer cluster with large angular momentum relative to the cluster centre.

The different dynamics of the high-velocity stars implies a signature in their circumstellar characteristics: stars being subject to close encounters are expected to lose their disc material faster and to a higher degree (Pfalzner *et al.*, 2006). Using the prescription of disc-mass loss in stellar encounters, indeed a clear correlation from numerical simulations is found: radial escapers, initially located close to the cluster centre and later expelled in a close encounter, lose more than 90 % of their disc material in 1 Myr of dynamical evolution, while orbital escapers, initially distant stars, moving on wide orbits around the cluster centre, do not experience strong perturbations and keep most of their disc material.

The numerical results are compared with infrared observations from Hillenbrand (1997), Muench *et al.* (2002), and Lada *et al.* (2004), tracing the (inner) circumstellar material. Though strict conclusions are not possible due to the small observational sample and some stars that cannot be classified according to the described scheme, the same trend is observed: stars that have been classified as orbital escapers do show near-infrared excess emission, indicative of circumstellar matter, while those classified as radial escapers show pure photospheric colours, lacking evidence of (inner) circumstellar discs.

This view is strongly supported by the work of Tan (2004) on the dynamics of  $\theta^1$ C Ori. The most massive star in the ONC,  $\theta^1$ C Ori, has a proper motion several times greater than the dispersion of bright ONC stars and much larger than the velocity expected if it were in equipartition with the other cluster stars (van Altena *et al.*, 1988). Tan (2004) showed that the direction of  $\theta^1$ C Ori’s motion is consistent with being exactly opposite to that of a B-type star embedded in the background molecular cloud, the so-called BN object, and concludes that it is most probably a runaway star originating from the Trapezium ejected about 4000 years ago after a close encounter with  $\theta^1$ C Ori. This supports the idea that stellar encounters may be likely events in such dense regions as the ONC, or at least in their cores. The evidence that the most massive stellar object was involved in a close encounter with another massive star is in best accordance with the work of Moeckel & Bally (2007a) and Pfalzner & Olczak (2007b).

Considering the dynamical age of the ONC of several crossing times, encounters must have had much stronger impacts on stellar discs at an early age of the cluster, when densities

were much higher but massive stars already had formed. Indeed, the simulations confirm this expectation, giving rise to an era of strong and frequent interactions among star-disc systems at the onset of massive star formation.

In even denser clusters such as the Arches cluster, high-velocity stars should be even more frequent than in the ONC. In such systems the current spatial and velocity distribution of the high-velocity stars should give strong indications of how the cluster developed in former times.

# 6. The ONC Revisited - A Family of Numerical Siblings

## 6.1. Introduction

The numerical results that have been obtained so far are based on a dynamical model of the Orion Nebula Cluster (ONC) – one of the observationally most intensively studied young star cluster. It was demonstrated that in the ONC stellar encounters can have a significant impact on the evolution of the young stars and their surrounding discs. However, investigating one model star cluster is not sufficient to draw general conclusions on other such objects. In fact, from the insights of the previous chapters one could not answer the following questions: How would things change in a *denser* cluster? Would a higher density inevitably imply that stellar encounters play a more important role in the star and planet formation process? And what would be the situation in more *massive* clusters? Would the larger number of stars play a role? What influence would the larger number of massive stars have? And finally: Is there a threshold in density and/or mass of the cluster where encounters start to play a significant role?

Due to the complexity of star cluster dynamics a conclusive answer to these questions demands further numerical investigations. It is thus vital to a deeper understanding of the present subject to extend the simulations of the ONC presented in the previous chapters and investigate a reasonable parameter space of cluster parameters. This has been realised by modelling scaled versions of the standard ONC model – clusters with varying stellar numbers and densities – that will be presented in this chapter.

The construction of the scaled models will be discussed in the next section, followed by an investigation of their dynamics. Afterwards results from the combination of the star cluster simulations and the star-disc encounters will be presented and compared to the outcome of the simulations of the ONC model cluster. A discussion of the results and a conclusion mark the last section of this chapter.

## 6.2. Construction of the Numerical Models

The cluster models are based on the same setup procedure as the standard ONC model described in Section 4.2. However, one construction step has been modified, that is, the generation of the high-mass end of the mass function. In the case of the ONC the upper mass limit was chosen to be  $50 M_{\odot}$  because this value corresponds to the mass of the most massive stellar system in the ONC, treated as a single particle in the simulation due to its compactness. However, adopting the same limit for the scaled models would seem to be an inappropriate constraint because stars with larger masses are expected to be formed in particular in more massive clusters, as discussed in Section 2.4. Thus in the framework of this numerical investigation the upper mass limit has been set to the current accepted fundamental upper mass limit,  $m_{\max} = 150 M_{\odot}$  (cf. Section 2.4). Due to the adopted shape of the mass function (see Eq. (2.17)) the most massive stars are generated in the most populated clusters.

One might wonder why the upper mass limit was not chosen according to the prescription of Weidner & Kroupa (2006), who showed that there exists a well-defined relation between the most massive star in a cluster and the cluster mass, consistent with their “sorted sampling” algorithm (see Section 2.4). The main reason not to do so was the aim to cover the largest parameter space possible, avoiding biased results due to selection effects. Moreover, the applied method allows for the highest flexibility: because each cluster has been simulated repeatedly with a different random sampling of masses, positions and velocities, there is the freedom to chose a subset of simulations that are in agreement with the results of Weidner & Kroupa (2006) (or any other specific model) and to investigate the effect of the adopted prescription for the generation of the maximum stellar mass in a cluster.

However, in Table 6.1 it is shown that – at least in a statistical sense – the exact prescription for the generation of the maximum stellar mass in a cluster is not as important as it might seem. In the last three columns the median of the maximum stellar mass in each simulation,  $m_{\max}^{\text{med}}$ , is compared to the mean maximum stellar mass for sorted sampling,  $m_{\max}^{\text{sort}}$ , and observational data,  $m_{\max}^{\text{obs}}$ , both estimated from Fig. 7 of Weidner & Kroupa (2006). It is evident that the values obtained by random sampling are only slightly larger than those from sorted sampling.

In total, nine cluster models have been set up according to the above discussion. One model is identical to the standard ONC model with the exception of the adopted higher stellar upper mass limit. Eight cluster models have been set up as scaled representations of ONC-like clusters. They form two parametric groups, the “density-scaled” and the “size-scaled” group, both containing four clusters with stellar numbers of 1000, 2000, 8000, and 16000, respectively.

It has to be noted that these “artificial” stellar systems are not just theoretical models but have as well counterparts in the observational catalogues of star clusters: the young star clus-

ter NGC 2024 (e.g. Haisch *et al.*, 2000; Bik *et al.*, 2003; Liu *et al.*, 2003) is well represented by the 1000 particle model, whereas the 16000 particle model has its counterpart in the massive cluster NGC 3603 (e.g. de Pree *et al.*, 1999; Stolte *et al.*, 2004, 2006).

### Density-scaled cluster models

Four cluster models have been simulated with the same initial size as the ONC ( $R = 2.5$  pc, see Section 4.1). Due to the adopted number density distribution, roughly represented by  $\rho(r) = \rho_0 r^{-2}$  (but see Section 4.2 for the detailed numerical model of the ONC), the density of the cluster models scales as the stellar number in comparison to the ONC model,

$$N = \int_0^R \rho(r) r^2 dr d\Omega \propto \rho_0 R, \quad (6.1)$$

though for an exact treatment one would have to consider the steeper density profile of the core,  $\rho_{\text{core}}(r) = \rho_{\text{core},0} r^{-2.3}$ ,

$$N_{\text{core}} = \int_0^{R_{\text{core}}} \rho_{\text{core}}(r) r^2 dr d\Omega \propto \rho_{\text{core},0} R_{\text{core}}^{0.7}. \quad (6.2)$$

However, since the core population is not dominant in terms of number, the four clusters are characterised in good approximation by densities that are 1/4, 1/2, 2, and 4 times the density of the ONC (at any radius), respectively (see Table 6.1). These models are used to study the importance of the density for the effect of star-disc encounters in a cluster environment. However, because the varying cluster densities are a result of the varying size of the initial stellar population, besides the density it is also the number of stars that might potentially influence the results. Thus another set of cluster models is required to study the pure effect of the size of the stellar population.

### Size-scaled cluster models

For this purpose four more cluster models have been simulated with the same initial density as the ONC (see Section 4.1 for details). In analogy to the previous models and due to the relation (6.1), the initial size of the clusters scales as the stellar number and was set up with 1/4, 1/2, 2, and 4 times the initial size of the ONC, respectively. These models are used to study the influence on the effect of star-disc encounters by the size of the stellar population of a cluster and to quantify the effect of the cluster density by combining the results with the density-scaled models.

One might wonder why the influence of the cluster density was not investigated by simply setting up more compact or extended versions of the ONC cluster model without modifying

the particle number (i.e. the cluster mass). The reason for this more extensive approach is twofold. First, in the present investigation one has to deal with three cluster parameters, namely the mass, size and dynamical time scale, of which each two are independent and determine the remaining one. An investigation of the influence of one quantity, in the present case the cluster density, thus requires *two* numerical studies, each with different two free and one fixed parameter. Second, observations show that while the radii of young star clusters are quite similar ( $\sim 0.5 - 5$  pc), their masses vary by about 5 orders of magnitude (e.g. Kroupa, 2005). In other words this means that cluster densities scale roughly with their mass, not their extension, and thus justifies the approach discussed.

As in the case of the numerical model of the ONC, of each cluster model a set of simulations has been performed with varying random configurations of positions, velocities, and masses, according to the given distributions (see Section 4.2 for details), to lower the effect of statistical uncertainties. For the clusters with 1000, 2000, 4000, 8000, and 16000 particles, a number of 200, 100, 100, 50, and 20 simulations seemed appropriate to provide sufficiently robust results.

Once more, a difference in the treatment of the cluster simulations has to be stressed. The simulations of the standard ONC model were post-processed by a validation scheme which ruled out clusters that did not match the observed projected density distribution or in which the most massive member escaped during the first Myr. This validation scheme has been dropped for the scaled models presented here because of two reasons. First, the scaled models are artificial configurations that can not be compared to observational data. Second, at least for the clusters more massive than the ONC, interactions between massive stars are more common, leading to a more frequent expulsion of massive members. Restricting the investigation only to those clusters that did not lose their most massive member prior to 1 Myr would thus impose an unjustified restriction.

The initial parameters of the cluster models, for each model averaged over all configurations, are presented in Table 6.1. Here the number density in the Trapezium Cluster is taken as a reference value for all simulations. As expected, the density scales with the number of stars for the density-scaled models, while it is rather constant for the size-scaled models. The velocity dispersion, that satisfies the relation

$$\sigma = \sqrt{\frac{2GM}{R}} \propto \sqrt{\frac{N}{R}}, \quad (6.3)$$

shows the expected scaling of  $\sqrt{N}$  for the density scaled models, and is again roughly constant for the size-scaled models, as expected from  $N \propto R$  (Eq. (6.1)) and the above relation. The reason for the slight increase of the velocity dispersion with decreasing stellar number for the size-scaled models is the steeper density profile in the cluster core, which becomes more dom-

inant in terms of stellar number with decreasing cluster size. Combining  $N_{\text{core}} \propto R^{0.7}$  from Eq. (6.2) and the above relation gives roughly  $\sigma_{\text{core}} \propto N^{-0.3}$  and thus explains the correlation.

In the next section analytical estimates for and numerical results of the cluster simulations will be presented in terms of cluster dynamics characterising the two families of models.

### 6.3. Dynamical Evolution of the Numerical Cluster Models

Before the numerical results will be presented, it is instructive first to estimate analytically the dynamical effects that can be expected in the two families of models. The basic quantities that play here a major role are the virial ratio,  $Q_{\text{vir}}$ , and the density distribution,  $\rho(r)$ .

The virial ratio has the interesting property to describe the global motion of the cluster volume: a hot cluster will expand, a cold cluster will contract, until virial equilibrium is reached (Eq. (2.1)). Clusters that are characterised by the same virial ratio do show – roughly – the same global inward or outward motion on comparable time scales, independent of their mass, size or velocity dispersion. This fact might appear counterintuitive, but it follows directly from the definition of the virial ratio: for a given virial ratio  $Q_{\text{vir}}$  the velocity dispersion  $\sigma$  of a cluster is determined by its potential  $V = GM/R$ , i.e. its mass and size; however, the cluster potential sets as well the magnitude of the deceleration of a particle. In other words: any particle that has travelled the same relative distance outwards (in terms of fraction of the cluster radius) has lost the same fraction of its kinetic energy. How does this affect the evolution of the density of the family of cluster models?

In the present case all clusters start from virial equilibrium and are thus expected to show (qualitatively) roughly the same temporal evolution of the density. However, because of the slight variation of the velocity dispersion of the size-scaled clusters, as discussed above, the dynamical time scale of the smaller cluster populations is smaller, leading to a faster evolution. Thus, the two models with 1000 and 2000 particles are expected to expand faster and to show a larger decrease of density with time.

The virial ratio of the clusters is expected to increase with time due to the escape of stars, preferentially from the outer cluster regions. The density-scaled cluster models are expected to show approximately the same distribution as a function of time because the fraction of escapers is not expected to differ significantly. Assuming that the number of stars,  $\Delta N_{\text{esc}}(R)$ , that escape from a shell of width  $\Delta R$  at a radius  $R$  is proportional to the number of stars in that shell,  $\Delta N(R)$ , one finds from Eq. (6.1):

$$\Delta N_{\text{esc}}(R) \propto \Delta N(R) \propto \rho_0 \Delta R \propto N \Delta R. \quad (6.4)$$

Hence the fraction of escapers,  $\Delta N_{\text{esc}}/N$  is constant in this case. In contrast, due to the

family of models	density-scaled			size-scaled					
	$R$ [pc]	$\rho_{\text{Trap}}$ [ $10^3 \text{ pc}^{-3}$ ]	$\sigma_{3D}$ [ $\text{km s}^{-1}$ ]	$R$ [pc]	$\rho_{\text{Trap}}$ [ $10^3 \text{ pc}^{-3}$ ]	$\sigma_{3D}$ [ $\text{km s}^{-1}$ ]	$m_{\text{max}}^{\text{med}}$ [ $M_{\odot}$ ]	$m_{\text{max}}^{\text{sort}}$ [ $M_{\odot}$ ]	$m_{\text{max}}^{\text{obs}}$ [ $M_{\odot}$ ]
$N$									
1000	2.50	1.3	1.15	0.63	4.8	2.42	36	32	$25 \pm 15$
2000	2.50	2.7	1.64	1.25	5.1	2.37	52	45	$25 \pm 15$
4000	2.50	5.3	2.26	2.50	5.3	2.26	79	63	$55 \pm 25$
8000	2.50	10.5	3.11	5.00	5.3	2.13	94	80	$75 \pm 25$
16000	2.50	21.1	4.34	10.00	5.3	2.11	125	112	$95 \pm 35$

Table 6.1.: Averaged initial parameters of the cluster models, divided among the families of density-scaled and size-scaled models. The first column contains the number of stars,  $N$ , the next six columns contain the cluster size,  $R$ , the number density in a sphere of radius 0.3 pc,  $\rho_{\text{Trap}}$  (equivalent to the Trapezium Cluster in the ONC, see Section 4.1), and the three-dimensional velocity dispersion,  $\sigma_{3D}$ , for the density-scaled and size-scaled models, respectively. The last three columns denote the median of the maximum stellar mass in each simulation,  $m_{\text{max}}^{\text{med}}$ , the mean maximum stellar mass for sorted sampling,  $m_{\text{max}}^{\text{sort}}$ , and estimates from observational data,  $m_{\text{max}}^{\text{obs}}$ , both taken from Fig. 7 of Weidner & Kroupa (2006).

constant density  $\rho_0$  of the size-scaled clusters,

$$\Delta N_{\text{esc}}(R) \propto \Delta N(R) \propto \rho_0 \Delta R \propto \Delta R. \quad (6.5)$$

and thus the fraction of escapers,  $\Delta N_{\text{esc}}/N \propto 1/N$ , decreases with the particle number. Hence the larger the population of the size scaled clusters, the less will the virial ratio increase with time. It is important to note that this “expansion” of the cluster population due to the escape of stars shall not be confused with the global cluster expansion that is set by the virial ratio. The former is driven by a small fraction of stars that reach a velocity that exceeds the cluster escape speed and become *unbound* from the cluster. In contrast, the latter reflects the bulk motion of the (mostly) *bound* cluster population, determined by a statistical quantity, the velocity dispersion, not the velocities of individual stars. In particular, the finding that the global expansion is independent of the stellar number of a cluster still holds.

In the next section the results from the numerical integration of the family of cluster models will be presented and compared to the derived analytical predictions.

### 6.3.1. Density-Scaled Cluster Models

In Fig. 6.1 and 6.2 the evolution of the density and the projected density distribution of the five density-scaled models is shown. The shape of the distributions is in all cases very similar. The discontinuities in the distribution of the core density in Fig. 6.1 are caused by the fluctuation of a small number of residual particles due to the dynamical evolution of the cluster. However, some differences, in particular between the two models with lowest and highest particle numbers, are evident. In the case of the volume densities in Fig. 6.1 the density of the larger volume, which corresponds to the initial size of the ONC, remains constant after about 2 Myr for the 16000 particle model, and after roughly 3 Myr for the 8000 particle model. This evolution marks the formation of a (at least temporary) bound subsystem of the entire cluster, as will be shown later. However, at earlier times, in particular until the assumed age of the ONC,  $t_{\text{ONC}} = 1$  Myr, all the cluster models evolve very homogeneously, as expected from the analytical estimates. This is clearly shown in Fig. 6.2 by plotting the projected density distributions at initial time (blue lines) and after 1 Myr (red lines). The evolved distributions have nearly identical shapes and are separated by vertical intervals of 0.3 in log-space, which corresponds to the difference of the initial densities by a factor 2. Only in the innermost cluster regions slight deviations between the evolved distributions are apparent. These are attributed to the poorer random sampling of the initial particle distribution due to the very steep density profile,  $\rho(r) \propto r^{-2.3}$ , as is evident from the larger scatter among the blue lines. However, after 1 Myr these deviations are smoothed out to a large degree.

As mentioned above, the cluster models show differences in the dynamical evolution at

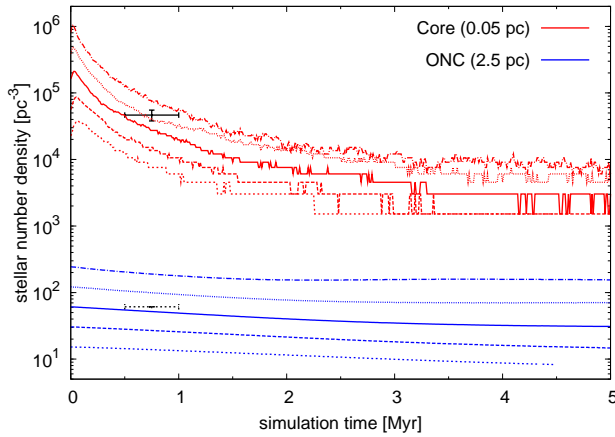


Figure 6.1.: Time evolution of stellar densities of all density-scaled cluster models in a volume of  $R = 2.5$  pc (“ONC”, blue line), and  $R_{\text{core}} = 0.05$  pc (“core”, red line), respectively. From bottom to top in each colour regime the cluster model with 1000, 2000, 4000, 8000, and 16000 particles is marked by a short-dashed, long-dashed, solid, dotted, and dot-dashed line, respectively. The black error bars mark the corresponding observational estimates of the ONC for comparison. This figure corresponds to Fig. 4.3, but does not contain the density of the volume representing the Trapezium Cluster to avoid confusion.

simulation times beyond  $\sim 2$  Myr, which is attributed to the formation of a larger bound fraction of the stellar population with increasing initial particle number. Exemplary this is shown for the two most extreme models with 1000 and 16000 particles in Fig. 6.3, respectively. The Lagrangian radii of the cluster with 1000 particles increase steadily over the whole simulation time, indicating the smooth expansion of the cluster. Only at very early times,  $\sim 0.1$  Myr, a slight decrease of the 10 % and 20 % Lagrangian radii is apparent. As discussed in Section 4.3, this feature marks a moderate contraction of the inner cluster region due to the initially steeper slope of the density distribution. In contrast, in the cluster with 16000 particles expansion stops at roughly 2 Myr, illustrated by the flattened slopes of the Lagrangian radii of mass fractions up to 50 %. While the 90 % Lagrangian radius increases steadily, tracking the fraction of escaping particles, the 70 % Lagrangian radius even starts to decrease after a maximum of 3 pc, which means that at this distance more stars begin to fall back into the cluster than do escape. Hence, after 3 Myr of evolution, a bound system with 70 % of the initial cluster mass and a radius of about 3-4 pc has formed.

Consequently, the virial ratio and velocity dispersion of the two cluster models in Fig. 6.4 show a different evolution. The steady expanding motion of the cluster with 1000 particles translates into a linear increase of the virial ratio with time, which exceeds the value for a bound system ( $Q_{\text{vir}} \leq 1$ ) after 4 Myr. The low-amplitude periodic oscillations are the signa-

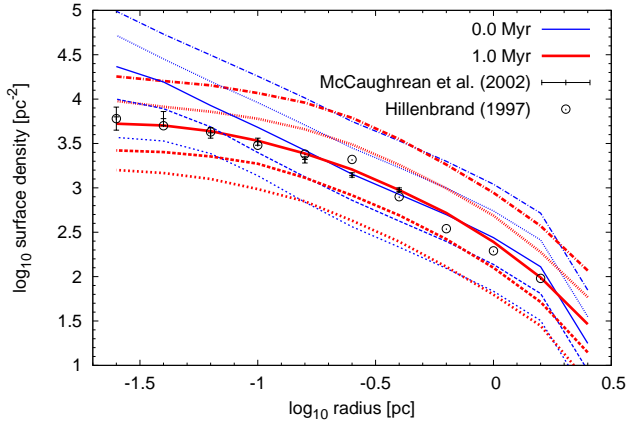


Figure 6.2.: Projected density profiles of the five density-scaled models compared to observational data. The initial profile (blue line) and the profile at a simulation time of 1 Myr (red line) are shown. From bottom to top in each colour regime the cluster model with 1000, 2000, 4000, 8000, and 16000 particles is marked by a short-dashed, long-dashed, solid, dotted, and dot-dashed line, respectively. The observational data are from a compilation of McCaughrean *et al.* (2002) and include also the values given by Hillenbrand (1997). This figure corresponds to Fig. 4.2 of the numerical model of the ONC.

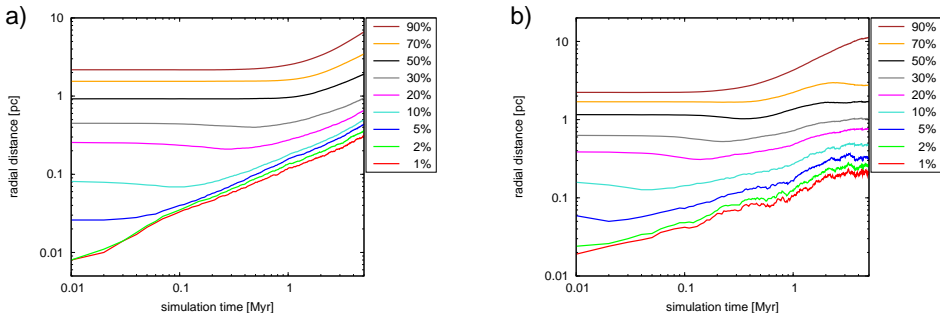


Figure 6.3.: Time evolution of Lagrangian radii exemplary for the density-scaled cluster model with **a)** 1000 and **b)** 16000 particles. The plotted Lagrangian radii correspond to mass fractions of 1 % (red), 2 % (green), 5 % (blue), 10 % (pink), 20 % (magenta), 30 % (black), 50 % (brown), 70 % (orange), and 90 % (yellow), from bottom to top, respectively. This figure corresponds to Fig. 4.4 of the numerical model of the ONC.

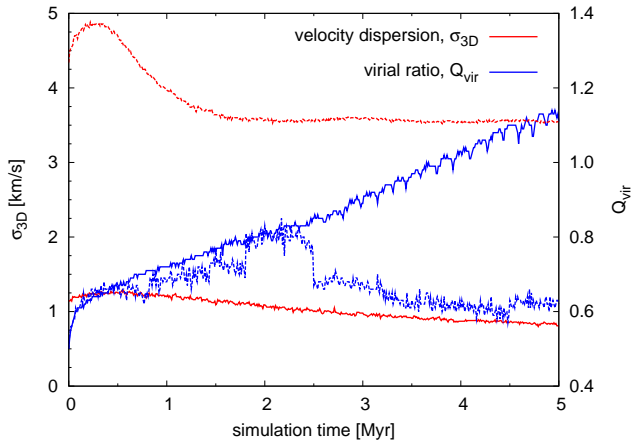


Figure 6.4.: Time evolution of the velocity dispersion (red) and the virial ratio (blue) exemplary for the density-scaled cluster model with 1000 (solid line) and 16000 particles (dashed line).

tures of the motion of wide massive binaries, typically with a semi-major axis on the order of  $10^4$  AU and a mass of  $10^2 M_{\odot}$ . The very moderate decrease of the velocity dispersion shows as well that the cluster remains kinematically too hot to form a substantially bound subsystem. In contrast, the virial ratio of the 16000 particle cluster is significantly below the value of an unbound system ( $Q_{\text{vir}} > 1$ ) during the whole simulation time and comes even close to the value of virial equilibrium ( $Q_{\text{vir}} = 0.5$ ) at times exceeding  $\sim 2.5$  Myr. The large amplitudes, in particular prominent at times  $\sim 2$  Myr, are caused by stars that are expelled from the cluster with very high velocities. The fact that escaping stars do transport a large fraction of kinetic energy outwards, cooling effectively the cluster, is apparent in the substantial decrease of the velocity dispersion by more than 20%. The roughly constant value of the velocity dispersion from 2 Myr on shows again that a bound stellar (sub-)system has formed that is approximately in dynamical equilibrium. However, one should note that at times earlier than 2 Myr, both cluster models show a very similar evolution of the virial ratio. This is in agreement with the analytical estimates and the previous finding that during this period all four density-scaled cluster models are dynamically equivalent to the standard cluster model of the ONC.

In summary, due to the nearly exact qualitative *and* scaled quantitative evolution of the density scaled cluster models, it is justified to ascribe differences of the effects of star-disc encounters on the stellar population mainly to one parameter, namely the initial density of the cluster models. Nevertheless, as mentioned above, the influence of the particle number has to be considered, too. This aspect will be addressed subsequently.

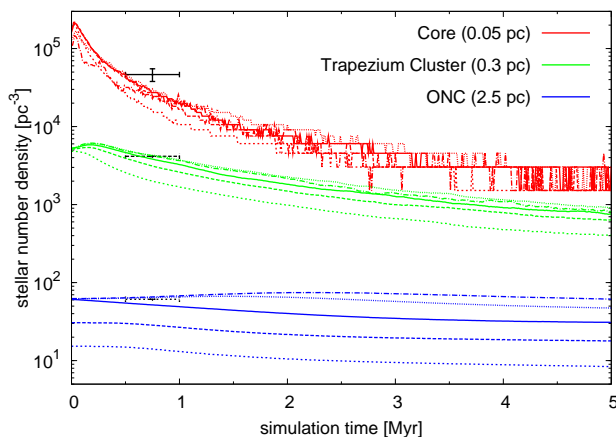


Figure 6.5.: Time evolution of stellar densities of all size-scaled cluster models in a volume of  $R = 2.5$  pc (“ONC”, blue line),  $R = 0.3$  pc (“Trapezium Cluster”, green line), and  $R_{\text{core}} = 0.05$  pc (“core”, red line), respectively. From bottom to top in each colour regime the cluster model with 1000, 2000, 4000, 8000, and 16000 particles is marked by a short-dashed, long-dashed, solid, dotted, and dot-dashed line, respectively. The black error bars mark the corresponding observational estimates of the ONC for comparison. This figure corresponds to Fig. 4.3.

### 6.3.2. Size-Scaled Cluster Models

The size-scaled cluster models show a different dynamical evolution compared to the density-scaled models discussed above and roughly in agreement with the analytical results.

Initially, the size-scaled clusters have roughly the same densities at corresponding cluster radii (that are smaller than the initial size of the smallest cluster with 1000 particles,  $r < 0.625$  pc). The initially lower densities of the two cluster models with 1000 and 2000 particles at a radius of 2.5 pc correspond to their lower initial size of  $1/4$  and  $1/2$  the size of the ONC.

The temporal evolution of the densities in Fig. 6.5 demonstrates that the clusters evolve on slightly different time scales, where the density declines faster for the less populated clusters. However, the densities of the models with 2000 particles and more differ not much, and are consistent with a coeval decline, as expected from the previous analytical estimates. The increase of the densities at 2.5 pc for the 8000 and 16000 particle model is due to an initial contraction, in accordance with the discussion in the previous Section 6.3.1, but stronger pronounced than for the density-scaled models. The different slopes reflect the different dynamical time scales of the stellar systems.

The evolution of the other cluster parameters is as well in good agreement with the analytical estimates, as shown in Fig. 6.6. The virial ratio in the upper panel is clearly a function of the particle number, increasing strongly for smaller populations, qualitatively according to

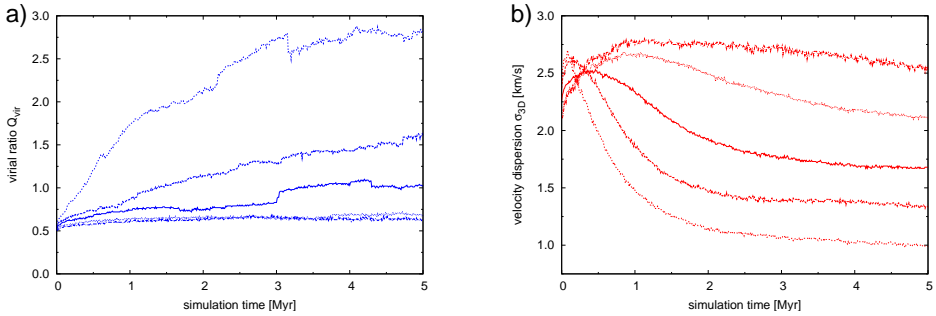


Figure 6.6.: **a)** Virial ratio (blue), and **b)** velocity dispersion (red) as a function of time for the five size-scaled cluster models. In each colour regime the cluster model with 1000, 2000, 4000, 8000, and 16000 particles is marked by a short-dashed, long-dashed, solid, dotted, and dot-dashed line, respectively.

Eq. (6.4). However, the correlation is not described by such a simple function of the particle number as Eq. (6.4). But that would also not be expected to be the case because the assumed analytical model of the particle escape is very rough, and the effect of such an event on the virial ratio depends on the detailed properties of the individual escaper and would thus require much more effort for a correct treatment which is far beyond the scope of the analytical estimate.

That a much larger fraction of escapers is found in the cluster models with smaller populations is demonstrated in the bottom panel of Fig. 6.6: the decline of the velocity dispersion with time is the steepest for the 1000 particle model (dotted line) and becomes very low for the 16000 particle model (dot-dashed line). The different times at which the velocity dispersion reaches its maximum (due to maximum contraction, as discussed in Section 4.3) agrees well with the crossing-time of each cluster model (see Table 6.1), as expected for a  $N$ -body system that adopts dynamically to a quasi-equilibrium state.

However, the main point of the investigation of the dynamics of the size-scaled cluster models is that the evolution of the cluster densities does not – to first order – depend on the number of particles, probably with the exception of the 1000 particle model, that shows moderate deviations. The five size-scaled models are thus well suited to investigate the effect of the number of cluster stars on star-disc encounters and the corresponding induced disc-mass loss. Having demonstrated as well the validity of the density-scaled models for an investigation of the dependence of the disc-mass loss on cluster density, both aspects will be faced in the next section.

## 6.4. Disc-Mass Loss Induced by Star-Disc Encounters

According to the previous section, analytical estimates will be presented prior to the numerical results. The treatment will concentrate on the encounter rates in the different cluster models, helping to obtain a first guess of the influence of the cluster environment on the encounter-induced disc-mass loss. A prescription of the disc-mass loss itself will not be included in the analytical part to keep the basic results as simple and clear as possible.

The treatment of encounters involves one important time scale, the *collision time*  $t_{\text{coll}}$ , expressed by Eq. (C.1). Here the inverse of the collision time will be introduced as the encounter rate,  $f_{\text{enc}} = t_{\text{coll}}^{-1}$ . Dropping the constants in Eq. (C.1) because only the relative quantities are of interest when comparing scaled models, and introducing the escape velocity  $v_*$  from the stellar surface,

$$v_* = \sqrt{\frac{2Gm_*}{r_*}}, \quad (6.6)$$

the encounter rate can be written as

$$f_{\text{enc}} \propto \rho \sigma \left( 1 + \frac{v_*^2}{4\sigma^2} \right), \quad (6.7)$$

where  $G$  denotes the gravitational constant,  $m_*$  and  $r_*$  the stellar mass and radius, and  $\rho$  and  $\sigma$  the density and velocity dispersion of the star cluster. In the following, the stellar radius  $r_*$  will be replaced by the “typical interaction radius”  $r_{\text{enc}}$ , that means the radius at which the star is subject to a significant (but still frequent) perturbation that potentially can remove some fraction of the disc-mass. Eq. (6.7) will be evaluated for three different stellar masses, representing stellar mass groups of low-, intermediate- and high-mass stars. Appropriate typical interaction radii are taken from Table 3 of Olczak *et al.* (2006). The set of masses  $m_*$ , radii  $r_{\text{enc}}$  and resulting “encounter escape speeds”  $v_{\text{enc}}$  is shown in Table 6.2.

Because the 4000 particle model represents the standard ONC model, which has been intensively studied, the calculations will be normalised to this model. All quantities related to the 4000 particle model will be thus denoted by a “0” as subscript. Adopting the initial velocity dispersion of the 4000 particle model,  $\sigma_0 \approx 2.3 \text{ km s}^{-1} \approx 0.5 \text{ AU/yr}$ , using

$$4\sigma^2 = 4\sigma_0^2 \left( \frac{\sigma}{\sigma_0} \right)^2 \approx \left( \frac{\sigma}{\sigma_0} \right)^2 \frac{\text{AU}}{\text{a}}$$

and the numbers given in Table 6.2, Eq. (6.7) can be simplified to

$$f_{\text{enc}} \propto \rho \sigma \left[ 1 + \gamma \left( \frac{\sigma_0}{\sigma} \right)^2 \right]. \quad (6.8)$$

mass groups	$m_*$ [ $M_\odot$ ]	$r_{\text{enc}}$ [AU]	$v_{\text{enc}}$ [AU/yr]	$\gamma_{\text{enc}}$
low mass	0.1	$10^2 - 10^3$	$\sim 0.3 - 0.1$	$10^{-2}$
intermediate mass	1 - 10	$10^2 - 5 \cdot 10^2$	$\sim 3 - 0.5$	1
high mass	100	$10^2$	$\sim 10$	$10^2$

Table 6.2.: Typical parameters adopted for the calculation of the encounter rate of cluster stars. The first column denotes the three mass groups, the second column contains the adopted mass ranges,  $m_*$ , while in the third typical interaction radii,  $r_{\text{enc}}$ , are listed for each mass group. In the last two columns the resulting “encounter escape speeds”,  $v_{\text{enc}}$ , and the “gravitational focusing parameter”,  $\gamma_{\text{enc}}$ , are noted. The gravitational focusing parameter, an approximation parameter, is defined here as the power of ten best representing  $v_{\text{enc}}^2$ .

An even more compact representation is possible when one considers the scaling properties of the two families of models: as can be derived from Eq. (6.1) and (6.3), the scaling relations for the density scaled models are  $\rho \propto N$  and  $\sigma \propto \sqrt{N}$ , while  $\rho = \text{const}$  and  $\sigma = \text{const}$  is found for the size-scaled models. Using these relations and normalising the encounter rate to the 4000 particle model,  $f_{\text{enc}}^{\text{norm}} = f_{\text{enc}}/f_{\text{enc},0}$ , one obtains

$$f_{\text{enc}}^{\text{norm}} = \begin{cases} \left(\frac{\rho}{\rho_0}\right)^{3/2} \left[\frac{1+\gamma_{\text{enc}}\left(\frac{\rho}{\rho_0}\right)^{-1}}{1+\gamma_{\text{enc}}}\right] & \text{density-scaled models,} \\ 1 & \text{size-scaled models.} \end{cases} \quad (6.9)$$

The derived relation for the normalised encounter rate predicts very different scaling relations for the two families of cluster models. Density scaled-models are expected to show large variations of the number of encounters, even with a superlinear dependency on the density for low-mass stars, i.e. when  $\gamma_{\text{enc}} \ll 1$ . In contrast, the encounter rate for the size-scaled models is expected to vary only for the different mass groups, but not among different models. For a better overview of the scaling in terms of numbers, Table 6.3 lists approximated relative encounter rates  $f_{\text{enc}}^{\text{norm}}$ , normalised to the low-mass group of the 4000 particle model. Table 6.3 demonstrates that the gravitational focusing parameter plays an important role for the massive stars. The encounter rates increase dramatically by roughly two orders of magnitude from the low- and intermediate-mass stars to the high-mass stars. This finding agrees well with the number of encounters of the ONC model presented in Fig. 4.9.

In summary, what one would expect from the numerical simulations of the density-scaled models is a steep increase of the number of encounters with cluster density with a power of 3/2 in case of the low-mass stars and a considerably shallower dependency with a power of 1/2 for the high-mass stars. However, due to the roughly two orders of magnitude larger number

family of models	density-scaled					size-scaled
	1000	2000	4000	8000	16000	
particle number						all
low mass	1/8	1/3	1	3	8	1
intermediate mass	5/8	1	2	4	10	2
high mass	50	70	100	140	200	100

Table 6.3.: Approximate relative encounter rates  $f_{\text{enc}}^{\text{norm}}$  from Eq. (6.9) of the five density-scaled and size-scaled models, normalized to the low-mass group of the 4000 particle model.

of encounters of massive stars than of low-mass stars in the 4000 particle model, still about one order of magnitude more encounters are expected for the massive stars in case of the 16000 particle model. In contrast, the size-scaled models should produce very similar results in terms of number of encounters, independent of the specific particle model. Analogous to the density-scaled models, the number of encounters of high-mass stars are expected to be about two orders of magnitude higher than for low- and intermediate-mass stars. One should caution that the discussed expectations do only base on statistical mean values of the cluster parameters and do not account for variations of density, velocity dispersion or virial ratio with, for example, stellar mass. Moreover, the parameter ranges of the three mass groups of low-, intermediate- and high-mass stars are rough estimates that are based on the most frequent encounter types, neglecting the very close (and strongly perturbing) encounters. This latter simplification does inevitably rule out the same scaling relation of the disc-mass loss with cluster density or stellar number as was obtained here analytically for the encounter rates. However, a comparison with the numerical results will show in how far the scaling relations are modified by means of disc-mass loss.

Before the effect of star-disc encounters on the disc-mass loss in the density-scaled cluster models will be investigated in detail, it is important to address the effect of one important parameter that has been modified compared to the standard ONC model: the stellar upper mass limit. It has been already discussed in the previous section that the exact generating algorithm of the mass limit probably is not very important. In Fig. 6.7 the average relative disc-mass loss as a function of the stellar mass is compared for the standard ONC model with a stellar upper mass limit of  $50 M_{\odot}$  (blue boxes), as used in the previous chapter, and the same model with an upper mass limit of  $150 M_{\odot}$  (red boxes). For masses below  $50 M_{\odot}$  the two distributions are qualitatively in good agreement, though it is evident that the average disc-mass loss in case of the lower mass limit is  $\sim 5\%$  larger in each mass bin up to  $\sim 2 M_{\odot}$ . This result is in contrast to the expected larger disc-mass loss for a higher stellar mass limit simply due to the fact that a more massive star i) acts as a stronger gravitational focus, ii) induces

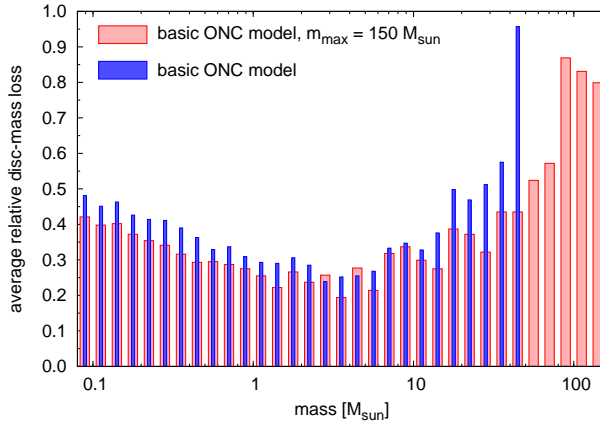


Figure 6.7.: Average relative disc-mass loss at 1 Myr for the Trapezium Cluster as a function of the stellar mass for a fixed disc radius of 150 AU. The standard ONC model with a stellar upper mass limit of  $50 M_{\odot}$  (blue bars) is compared to a simulation of the same model with an upper mass limit of  $150 M_{\odot}$  (red bars).

larger perturbations, and iii) perturbs discs out to larger distances, as shown in Section 4.4.

However, a detailed investigation of this apparent contradiction showed that the differences of the two distributions in Fig. 6.7 can not be explained by the difference of the adopted upper mass limit. For various subsets of the 100 simulations of the 4000 particle model with different ranges of the maximum stellar mass very similar distributions have been found, with much lower differences than that between the 4000 particle model and the standard ONC model. The intermediate and high-mass parts of the two distributions in Fig. 6.7 show no significant deviations. In the intermediate range of  $\sim 2\text{--}10 M_{\odot}$  both distributions agree very well; for more massive stars up to  $50 M_{\odot}$  the average disc-mass loss of the  $50 M_{\odot}$ -limit model is significantly higher. This is expected because stars with masses in the range  $10\text{--}50 M_{\odot}$  can act as additional strong gravitational foci in the presence of a most massive cluster member of  $50 M_{\odot}$ , while their effect is largely reduced if a  $150 M_{\odot}$  star is gravitationally dominating. The most massive stars in the range  $80\text{--}150 M_{\odot}$  show, as expected, the largest average relative disc-mass loss. That it is somewhat lower than that of the most massive star of the  $50 M_{\odot}$ -limit model is in agreement with the stronger gravitational attraction of their disc, leading on average to a reduced disc-mass loss per encounter. However, since the highest mass bin is only populated by 9 stars, any further conclusions about the average relative disc-mass loss of the most massive stars would be highly speculative.

### 6.4.1. Density-Scaled Cluster Models

In this section one fundamental question of the encounter-induced disc-mass loss is addressed: How does the density of the cluster environment influence the effect that star-disc encounters have on circumstellar discs?

Perhaps the best rough estimate of the role of the cluster density would be a comparison of the fraction of completely destroyed discs in each cluster model, as introduced in Section 4.3. The distributions in Fig. 6.8 show the average fraction of stars that are surrounded by disc material and correspond from top to bottom to clusters with increasing density. Compared to Fig. 4.6, the error bars have been removed and the curves have been smoothed with Bezier curves to provide a clearer view. It is evident that for both, the entire ONC region and the more compact region of the Trapezium Cluster, the fraction of destroyed discs increases significantly with increasing cluster density. In particular, the effect becomes much stronger for the clusters with 2 and 4 times the density of the ONC (dotted and dot-dashed line). In the case of the 16000 particle model (dot-dashed line), even up to 60% of the stars in the Trapezium Cluster could have lost their discs after 1 Myr of dynamical evolution. But it is also interesting to note that even in a cluster 4 times less dense than the ONC (short-dashed line), still 10-15% of the stars could lose their surrounding discs due to gravitational interactions with cluster members. However, one has to treat these numbers with care due to the – partially – significant uncertainties that go into the calculations, as discussed in Section 4.4.5. Nonetheless, what is more of importance here – and relies only on the *relative* quantities – is the fact that the distributions in Fig. 6.8 are not equidistant but do show larger differences with increasing particle number. The analytical estimate of the encounter rate, Eq. (6.9), provides an explanation for this trend. Because the encounter rate of low-mass stars scales as  $\rho^{3/2}$ , while that of high-mass stars scales as  $\rho^{1/2}$ , encounters of low-mass stars are expected to become more dominant with increasing cluster density than encounters of high-mass stars, qualitatively in agreement with the trend in Fig. 6.8. Since this trend becomes prominent for the two cluster models with higher densities than the ONC, it seems that the density of the ONC represents a critical value that marks the onset of a much more destructive effect of star-disc encounters in clusters of higher density. This finding has to be investigated in greater detail.

In order to determine the dominant mode of the star-disc interactions, i.e. if there is a preferred mass range of stars that become disproportionately high involved in perturbing encounters with increasing cluster density, in Fig. 6.9 the average relative disc-mass loss as a function of time for three different stellar mass groups has been plotted. The ranges of the mass groups have been determined individually, in dependence of the size of the stellar population, for the models with 1000, 2000, 4000, 8000, and 16000 particles. The method is described in detail in Appendix D.1. Results for three cluster models, with 1000 (short-dashed

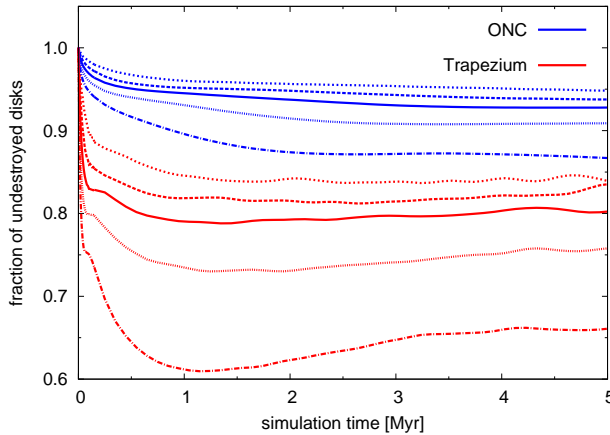


Figure 6.8.: Time evolution of the fraction of stars that possess a circumstellar disc, for a region of the size of the ONC (blue) and the Trapezium Cluster (red). The curves have been smoothed by Bezier curves to avoid intersecting lines. From top to bottom in each colour regime the cluster model with 1000, 2000, 4000, 8000, and 16000 particles is marked by a short-dashed, long-dashed, solid, dotted, and dot-dashed line, respectively.

line), 4000 (solid line), and 16000 (dot-dashed line) particles are illustrated for comparison. It seems that, in terms of disc-mass loss, high-mass stars are not strongly affected by the density of a cluster environment. In particular, the average disc-mass loss of the high-mass stars is not much different in the simulations with 1000, 4000, and 16000 particles. The situation is quite different for the lower mass stars: here the average disc-mass loss of both mass groups increases strongly with cluster density. This is in particular the case for the 16000 particle model, which shows nearly twice as large values as the 4000 particle model. The fact that the highly increased disc-mass loss of the lower mass stars has no corresponding higher disc-mass loss of the high-mass stars is an important finding. One possible explanation would be that the increasing perturbations of the lower mass stars are the outcome of encounters preferentially between low- and intermediate-mass stars – due to closer encounters or a higher frequency of encounters.

Indeed, as is demonstrated by Fig. 6.10 and 6.11, the interaction of low- and intermediate-mass stars between each other becomes more dominant with increasing cluster density. The former shows the number of encounters as a function of stellar mass for the density-scaled models. Besides the fact that, as expected, the total number of encounters rises with cluster density, the outstanding feature is the increasing dominance of encounters of low- and intermediate-mass stars. The two upper panels in Fig. 6.10 demonstrate that this is the case for all types of encounters – weak, medium and strongly perturbing. In contrast, the number of encounters of the high-mass stars in the densest cluster model is much less increased com-

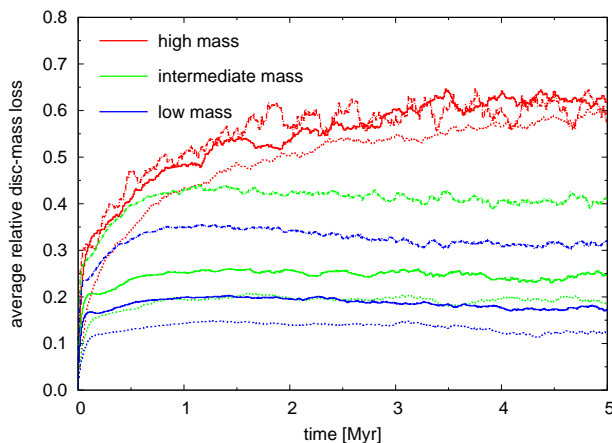


Figure 6.9.: Temporal dependence of the average relative disc-mass loss of three different stellar mass groups (see Appendix D.1 for the width of the mass intervals): low-mass stars (blue line), intermediate-mass stars (green line), and high-mass stars (red line). From bottom to top in each colour regime the cluster model with 1000, 4000, and 16000 particles is marked by a short-dashed, solid, and dot-dashed line, respectively.

pared to the lower density clusters, as shown in the bottom panel. Fig. 6.11 illustrates that the increasing number of encounters of low- and intermediate-mass stars occurs predominantly between stars of similar mass. Here the number of encounters is plotted as a function of the relative perturber mass, i.e. the mass ratio of perturber and perturbed star. The upper range of the relative perturber mass is given by the ratio of the upper and the lower stellar mass limit,  $\mu_{\max} = 150M_{\odot}/0.08M_{\odot} = 1875$ . The lower range is determined by the lowest relative perturber mass that can cause an encounter, i.e. a minimum relative disc-mass loss of 0.03 (see Section 4.4.2), which is typically  $\mu_{\min} \lesssim 0.1$ . While in the low-density cluster models the number of weak, intermediate and strong encounters is roughly equally distributed over the entire range of relative perturber masses, a prominent peak at  $\mu \approx 1$  marks the distribution of all encounters for the high-density cluster models. The transition between these two shapes is marked by the 4000 particle cluster model. Consequently, the group of high-mass stars becomes less important for the encounter-induced disc-mass loss of the low- and intermediate-mass stars in clusters with higher densities than the ONC.

This finding can be compared again with the analytical estimate of the encounter rate. For low densities, corresponding to low particle numbers in the present models, one would expect from Eq. (6.9) that the high-mass stars dominate the encounter rate, favouring a scaling  $f_{\text{enc}}^{\text{nom}} \propto \rho^{1/2}$ . This expectation is in good agreement with the results from the numerical simulations presented in Fig. 6.12, which show that the encounter rates of the cluster models with 1000, 2000, and 4000 particles are scaling roughly as  $N^{1/2}$ , and is attributed to the

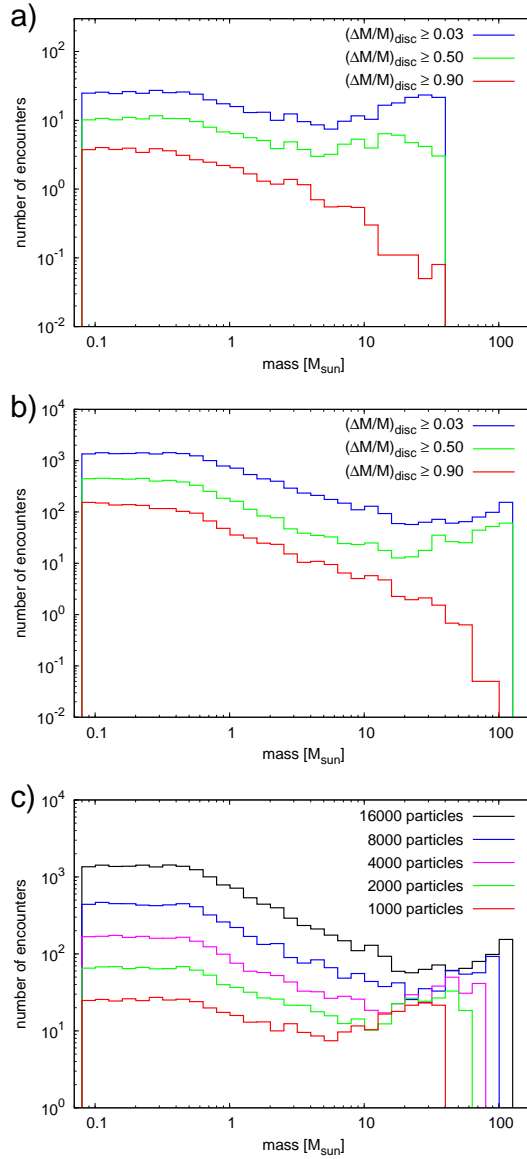


Figure 6.10.: Number of encounters as a function of stellar mass (logarithmic bins). The top and middle panel depict the number of encounters for three different groups by means of disc-mass loss per encounter for the cluster model with **a)** 1000 particles and **b)** 16000 particles, respectively (blue: all encounters (see Section 4.4.2 for the definition of an encounter), green: at least 50 % disc-mass loss, red: at least 90 % disc-mass loss). The bottom panel **c)** shows all encounters for each of the five density-scaled cluster models.

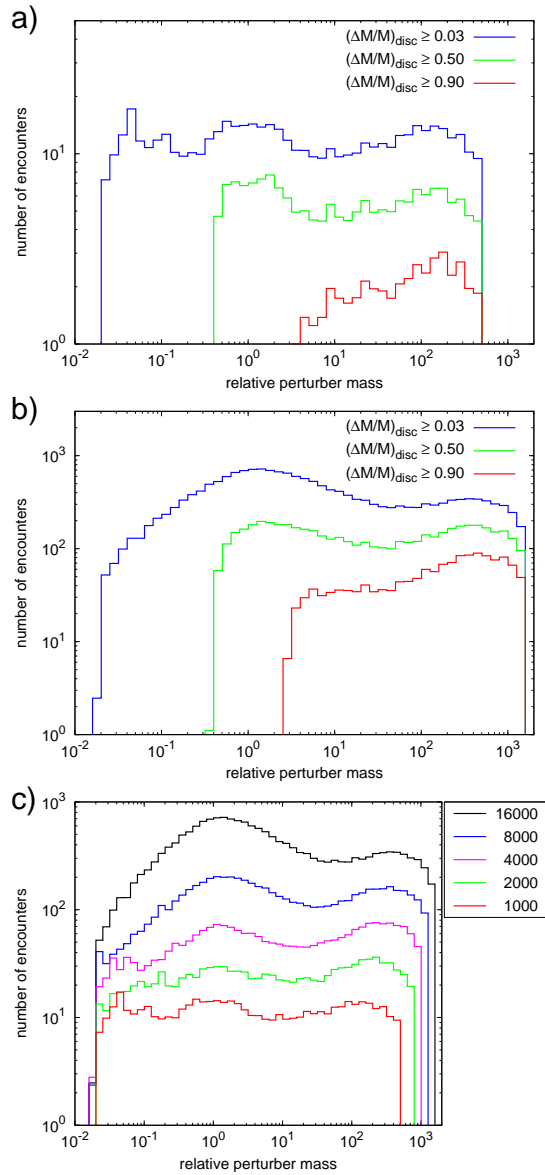


Figure 6.11.: Number of encounters as a function of the relative perturber mass (logarithmic bins). The top and middle panel depict the number of encounters for three different groups by means of disc-mass loss per encounter for the cluster model with **a)** 1000 particles and **b)** 16000 particles, respectively (blue: all encounters (see Section 4.4.2 for the definition of an encounter), green: at least 50 % disc-mass loss, red: at least 90 % disc-mass loss). The bottom panel **c)** shows all encounters for each of the five density-scaled cluster models.

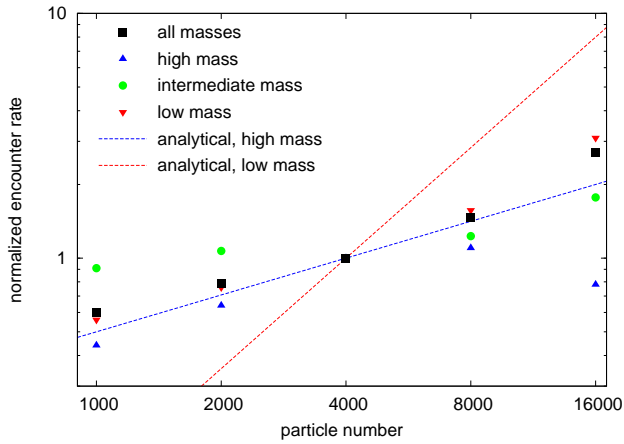


Figure 6.12.: Normalised encounter rate  $f_{\text{enc}}^{\text{norm}}$  of the five density-scaled cluster models in comparison with the analytical estimate given by Eq. (6.9). The black squares represent all stars in the Trapezium Cluster region ( $R = 0.3$  pc), the other symbols stand for predefined mass groups: high-mass,  $m \geq 10M_{\odot}$  (blue triangles), intermediate-mass,  $10M_{\odot} \geq m \geq 1M_{\odot}$  (green circles), and low-mass stars,  $m \leq 1M_{\odot}$  (red downward triangles). The dashed lines depict the analytical estimate of the encounter rate for high-mass (blue line) and low-mass stars (red line). The ranges of the mass groups have been chosen here different from those in previous figures to account for the mass regimes of the encounter rate presented in Table 6.2.

fact that the lower mass stars interact preferentially with massive stars. For higher particle numbers the distribution becomes more complex. Here the high-mass stars show a trend of *decreasing* encounter rate with particle number. This feature accounts for the decreasing importance of the high-mass stars as gravitational foci (for the lower mass stars) and is a consequence of the decreasing ratio of the mass of the most massive star and the cluster mass. Accordingly, the distribution of the encounter rate of the low-mass stars tends towards the analytical limit of  $N^{3/2}$  for low-mass stars, representing the more frequent interaction of low-mass stars with each other.

The above results show that in star clusters with higher densities than the ONC massive stars lose their outstanding role as encounter partners of lower mass stars. Combined with the previous finding that the density of the ONC represents as well a critical value by means of a much more destructive effect of star-disc encounters in clusters of higher density, the higher disc destruction rate in these clusters is largely attributed to encounters of low- and intermediate mass stars with partners of similar mass.

The effect on the disc-mass loss as a function of stellar mass is demonstrated in Fig. 6.13. For low- and intermediate-mass stars, the increase of the average relative disc-mass loss shows the same trend as for the encounter rates: the increase is moderate for the cluster

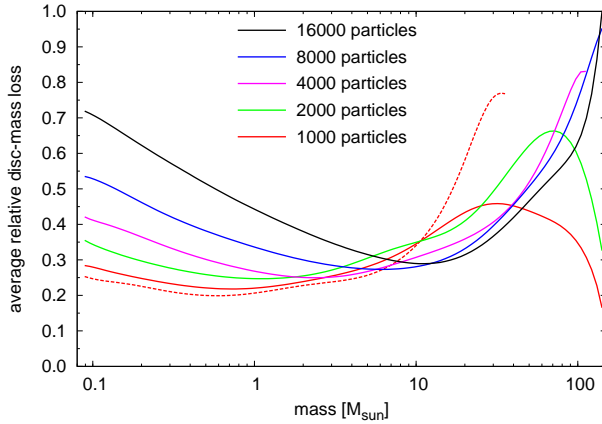


Figure 6.13.: Smoothed average relative disc-mass loss at 1 Myr for the Trapezium Cluster as a function of the stellar mass for a fixed disc radius of 150 AU. The distributions of the five density-scaled cluster models have been smoothed by Bezier curves and are represented by different colours (see legend). The red dashed line represents an average over simulations of the 1000 particle model in which the maximum stellar mass was in the range 20–36  $M_{\odot}$ .

models with 1000 to 4000 particles (red, green, and magenta line), and becomes much larger for the two most massive cluster models (blue and black line). The situation for the high-mass stars appears to be less evident. This is because the sampling of the high-mass stars is very poor for low particle numbers. The very broad and low peak at the high-mass regime of the 1000 particle model is just an effect of the average over simulations with different maximum masses of the sampled stellar populations. However, if one builds a restricted sample in terms of maximum stellar mass, as has been done here exemplary for a mass range of 20–36  $M_{\odot}$  (dashed red line), it becomes apparent that the disc-mass loss in the high mass regime is qualitatively not much different than for the higher density clusters. In all five cluster models the most massive star loses (nearly) its complete disc mass.

In summary, the variation of the disc-mass loss due to encounters for cluster environments of different densities shows two important features: i) low- and intermediate-mass stars lose a larger fraction of their disc material with increasing cluster density, and ii) the discs of the most massive stars are (nearly) completely destroyed, independent of the density of the cluster environment. The important finding for i) is that the correlation is not linear, but shows a much larger increase for the two model clusters with the largest densities (and populations), implying that there exists a critical density that marks the onset of a much more destructive effect of star-disc encounters. This critical density seems to be close to the density of the ONC.

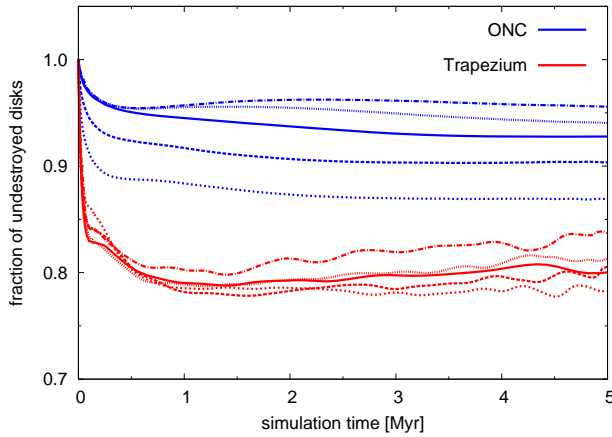


Figure 6.14.: Time evolution of the fraction of stars that possess a circumstellar disc, for a region of the size of the ONC (blue,  $R = 2.5$  pc) and the Trapezium Cluster (red,  $R = 0.3$  pc). The curves have been smoothed by Bezier curves to avoid intersecting lines. Here the disc size was assumed to be fixed. From top to bottom in each colour regime the cluster model with 1000, 2000, 4000, 8000, and 16000 particles is marked by a short-dashed, long-dashed, solid, dotted, and dot-dashed line, respectively.

In the next section it will be examined whether the results of the size-scaled cluster models are as well in agreement with the theoretical estimates and which effect the number of stars in a cluster does have on star-disc encounters.

### 6.4.2. Size-Scaled Cluster Models

In accordance with the previous section, the first quantity to discuss and compare with the distributions of the density-scaled models is the fraction of stars that are surrounded by discs, depicted in Fig. 6.14. It is evident that, in the case of the Trapezium Cluster, the fractions of all five size-scaled cluster models are in very good agreement. The somewhat larger deviation of the 16000 particle model is most probably due to the low statistics: while the stellar number in the Trapezium Cluster is roughly the same for all size-scaled cluster models, only 20 simulations have been performed with 16000 particles, compared to 200 realisations of the 1000 particle model (see also Section 6.2).

The significant difference of the fraction of stars with discs in the entire ONC region among the size-scaled models is due to the initial setup. Both, the 1000 and the 2000 particle model are initially smaller in extension than the adopted ONC radius of 2.5 pc and thus lack a large population of stars in the outer cluster region. Stars in these much less dense regions lose on average a much lower fraction of their disc mass, increasing the fraction of star-disc sys-

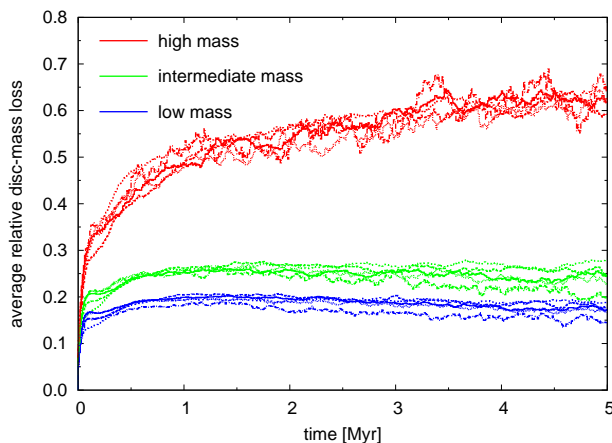


Figure 6.15.: Temporal dependence of the average relative disc-mass loss of three different stellar mass groups (see Appendix D.1 for the width of the mass intervals) in the Trapezium Cluster: low-mass stars (blue line), intermediate-mass stars (green line), and high-mass stars (red line). In each colour regime the cluster model with 1000, 2000, 4000, 8000, and 16000 particles is marked by a short-dashed, long-dashed, solid, dotted, and dot-dashed line, respectively. Here the disc size was assumed to be scaled with the stellar mass.

tems in a cluster. At later simulation times, also differences among the other cluster models become apparent. This evolutionary effect is caused by the initial contraction of the stellar system, which is the more pronounced the higher the particle number, as discussed for Fig. 6.5.

The evolution of the five size-scaled cluster models in terms of disc-mass loss is very similar for the three mass regimes of low-, intermediate- and high-mass stars, demonstrated by Fig. 6.15 for the Trapezium Cluster. Until  $\sim 2$  Myr the distributions of the average relative disc-mass loss are virtually the same. At later times there seems to be a slight trend of a lower average disc-mass loss of the low- and intermediate-mass stars for higher particle numbers. This could be understood as a consequence of the more pronounced contraction with higher particle number, inducing a transport of unperturbed stars from the outer cluster regions into the central region. However, since the differences between the distributions are on the order of the uncertainties of the average disc-mass loss, in particular for the low sampled 16000 particle model, the relevance of the feature should be regarded with caution.

Similar to the temporal distribution, the spacial distribution of the average relative disc-mass loss, presented in Fig. 6.16, shows a common shape among the five size-scaled models for all three groups of low-, intermediate- and high-mass stars. The only exception marks the 10-15% higher disc-mass loss of the high-mass stars in the outer region of the 1000 particle model. This feature is explained by the faster expansion of the initially more compact

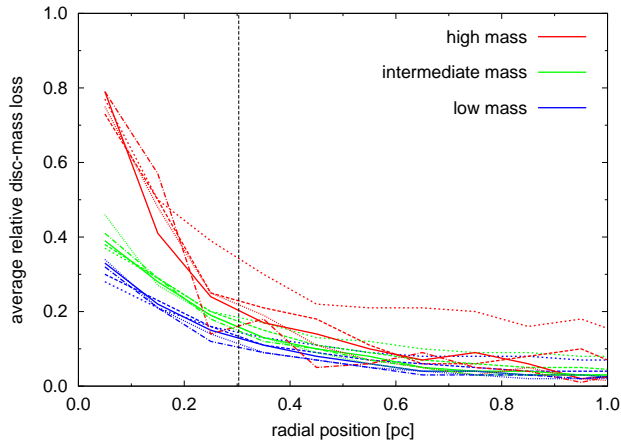


Figure 6.16.: The average relative disc-mass loss as a function of the radial distance from the cluster centre of three different stellar mass groups (see Appendix D.1 for the width of the mass intervals): low- (blue line), intermediate- (green line), and high-mass stars (red line). In each colour regime the cluster model with 1000, 2000, 4000, 8000, and 16000 particles is marked by a short-dashed, long-dashed, solid, dotted, and dot-dashed line, respectively. Here the disc size was assumed to be scaled with the stellar mass. The vertical black dashed line marks the radial extension of the Trapezium Cluster.

configuration compared to the other cluster models. Consequently, the high-mass stars leave the central cluster region earlier and more frequently in the 1000 particle model. In the disc-mass loss distributions of the high-mass group of the individual simulations this effect manifest as more prominent and more frequent single peaks in the outer cluster region. The average of 200 representations shown here tends to smear out the individual features over the entire radial interval and causes an elevated, smooth distribution.

The presented results for the disc-mass loss show that the size-scaled models are equivalent in their environmental effect on protoplanetary discs. Though this seems to be in agreement with the analytical estimate of the encounter rate, given by Eq. (6.9), there is one good reason disfavours such a relation. As was shown in Fig. 6.5, the dynamical evolution of the cluster models is slightly different and the density of the 1000 and 2000 particle models decreases faster than for the more massive clusters, even up to a factor of 2 in case of the 1000 particle model. Thus one would expect a lower encounter rate in these smaller systems and, consequently, on average a lower disc-mass loss. However, this is obviously not the case, but can be explained by Fig. 6.17. In the case of low- and intermediate mass stars the presented encounter rates, normalised to the 4000 particle model, are in good agreement with the analytical estimate, which predicts a constant distribution as a function of particle number for the size-scaled models. In contrast, the normalised encounter rate of the high-mass stars de-

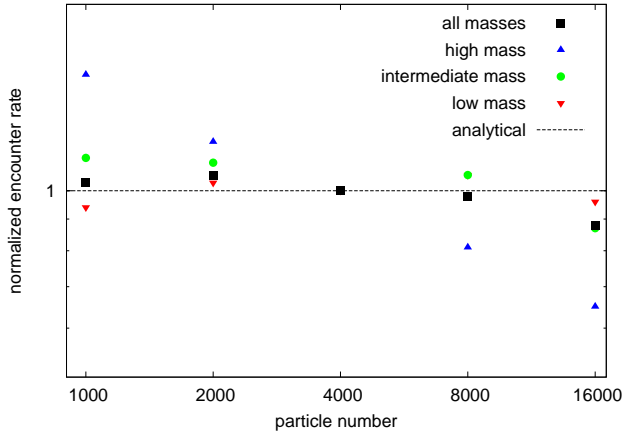


Figure 6.17.: Normalised encounter rate  $f_{\text{enc}}^{\text{norm}}$  of the five size-scaled cluster models in comparison with the analytical estimate given by Eq. (6.9). The black squares represent all stars in the Trapezium Cluster region ( $R = 0.3 \text{ pc}$ ), while the other geometrical symbols stand for predefined mass groups: high-mass stars,  $m \geq 10 M_{\odot}$  (blue triangles), intermediate-mass stars,  $10 M_{\odot} \geq m \geq 1 M_{\odot}$  (green circles), and low-mass stars,  $m \leq 1 M_{\odot}$  (red downward triangles). The dashed black line depicts the analytical estimate of the encounter rate for all stellar masses. The ranges of the mass groups have been chosen here different from those in previous figures to account for the mass regimes of the encounter rate presented in Table 6.2.

creases with increasing particle number. This trend shows that the high-mass stars, similarly to the finding for the density scaled models, become less important as gravitational foci for the low-mass stars in clusters with larger stellar populations. Hence, in terms of encounter statistics, the lower density of the 1000 and 2000 particle models is compensated by the more frequent interactions of the high-mass stars.

That the discussion of the encounter rates is as well representative of the corresponding disc-mass loss is demonstrated in Fig. 6.18. For masses below  $1 M_{\odot}$  the size-scaled models show nearly identical results, while higher stellar masses do suffer a larger disc-mass loss in clusters with smaller populations.

Keeping in mind that the prescription used in the present investigation to determine the encounter-induced disc-mass loss is expected to overestimate this effect in a number of cases (see Section 4.4.5 for a discussion), it is important to estimate the validity of the findings. This is part of the next section.

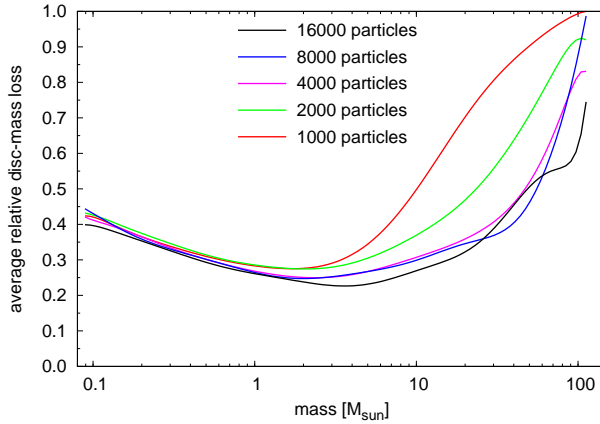


Figure 6.18.: Smoothed average relative disc-mass loss at 1 Myr for the Trapezium Cluster as a function of the stellar mass for a fixed disc radius of 150 AU. The distributions of the five size-scaled cluster models have been smoothed by Bezier curves and are represented by different colours (see legend).

## 6.5. Validity of the Results

To validate the results obtained so far, in the following the encounters will be analysed in terms of their properties – in particular those encounters, that seem to become dominant for cluster densities above the critical density. As shown in the previous sections, these are encounters of low- and intermediate mass stars that occur preferentially between stars of equal mass.

In Fig. 6.19 the number of encounters as a function of eccentricity and in dependence of the disc-mass loss per encounter is presented for the two cluster models with 1000 and 16000 particles. In the low-density cluster model by far the most encounters are pseudo-parabolic (i.e. 57% of all encounters have  $0.8 \leq \epsilon \leq 2.0$ , as defined in Section 4.4.5), whereas the situation is much different for the model with the highest density. While the distributions for all three minimum disc-mass loss fractions peak at the parabolic case, the contribution from hyperbolic encounters is much higher and increases significantly towards encounters with a lower relative disc-mass loss, leading to a broader and marginally lower second peak at  $\epsilon \approx 30$ . Consequently, the type of encounter that has growing importance in the disc destruction process with increasing cluster density is a strongly hyperbolic. This fact might be a critical one because, as was discussed in Section 4.4.5, in hyperbolic encounters the disc-mass loss can be much lower than in parabolic encounters.

To estimate the bias that is introduced by treating all encounters in the calculations of the disc-mass loss as parabolic, the relative disc-mass loss as a function of eccentricity must

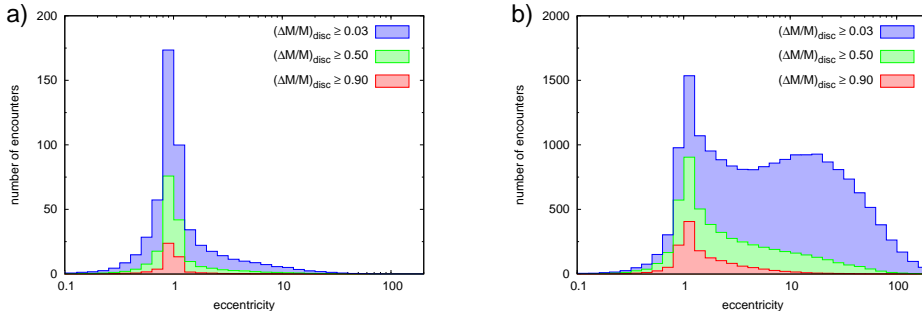


Figure 6.19.: Number of encounters as a function of the eccentricity (logarithmic bins), plotted for three different groups by means of disc-mass loss per encounter. The blue surface represents all encounters (see Section 4.4.2 for the definition of an encounter), the green those that removed at least 50 % of the disc-mass, while the red stands for the most destructive encounters that caused a disc-mass loss of at least 90 %. The two plots show the distributions for the density-scaled cluster models with **a)** 1000 particles and **b)** 16000 particles.

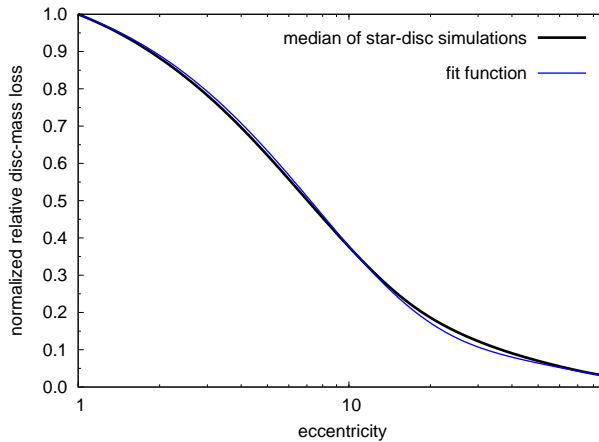


Figure 6.20.: Relative disc-mass loss normalised to the strict parabolic case ( $\varepsilon = 1$ ) as a function of eccentricity for all star-disc simulations that have been performed (see Section 4.4.2 for the adopted parameter space). The black line marks the median of all simulations, the blue line is the fit function from Eq. (6.10).

be determined. Fig. 6.20 shows the median distribution of the relative disc-mass loss as a function of eccentricity, normalised to the parabolic case, for all star-disc simulations that have been performed (see Fig. 4.13 for comparison). The blue curve in the figure depicts the fit function that has been determined for this median distribution,

$$\widehat{\Delta m}(e) = \exp[0.12(e-1)]\{0.83 - 0.015(e-1) + 0.17 \exp[0.1(e-1)]\} \quad (6.10)$$

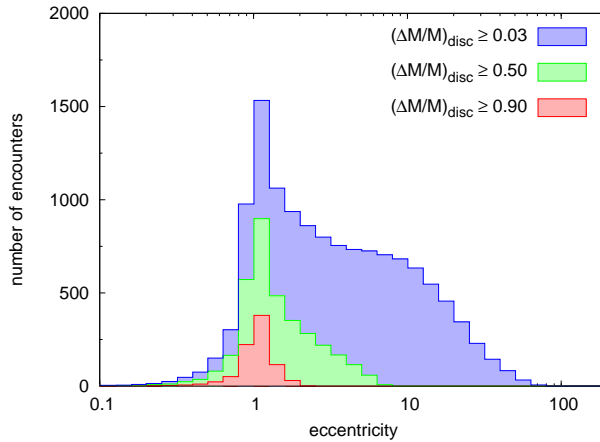


Figure 6.21.: Number of encounters as a function of eccentricity (logarithmic bins), corrected for effects of eccentricity by using Eq. (6.10). Three different groups by means of disc-mass loss per encounter are plotted. The blue surface represents all encounters (see Section 4.4.2 for the definition of an encounter), the green those that removed at least 50% of the disc-mass, while the red stands for the most destructive encounters that caused a disc-mass loss of at least 90%. The plot shows the distribution for the density-scaled cluster model with 16000 particles.

and shows that it is a good representation.

Using this fit function, the previous results have been reevaluated. Fig. 6.21 shows again the distribution of the number of encounters against eccentricity for the density-scaled 16000 particle model. Compared to Fig. 6.19b, the number of hyperbolic encounters with eccentricities  $e \gtrsim 5$  is significantly reduced and the extreme cases with  $e \gtrsim 100$  are completely removed. However, one has to stress that the fit function represents a median distribution, inevitably still overestimating the effect of weak encounters and suppressing the strong encounters too much. Thus the significant reduction of heavily perturbing eccentric encounters, represented by the green and red surfaces, is most probably overestimated.

Nevertheless, the encounters that are characterised by the largest eccentricities and are thus most affected by the implementation of the fit function are the weakly perturbing events. As has been shown previously (see Section 6.4.1), these events are most numerous in the density-scaled 16000 particle model and result preferentially from interactions of low- and intermediate mass stars with equal-mass perturbers. Hence one would expect that the differences of the derived disc-mass loss of the less massive stars among the density-scaled models should be reduced if eccentricities are considered explicitly. In fact, Fig. 6.22 demonstrates that, in comparison to Fig. 6.13, the previous differences of up to 45% for the lowest mass stars are reduced to at most 15%. Continuously reduced, the differences are apparent up to

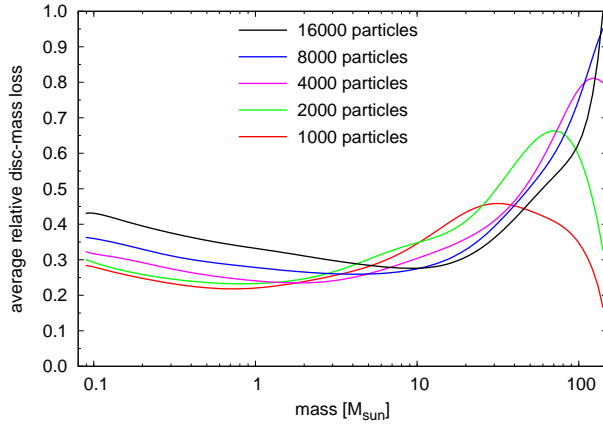


Figure 6.22.: Smoothed average relative disc-mass loss, not restricted to parabolic encounters, at 1 Myr for the Trapezium Cluster as a function of the stellar mass for a fixed disc radius of 150 AU. The calculation was extended by the implementation of a fit function of the form (6.10). The distributions of the five density-scaled cluster models have been smoothed by Bezier curves and are represented by different colours (see legend).

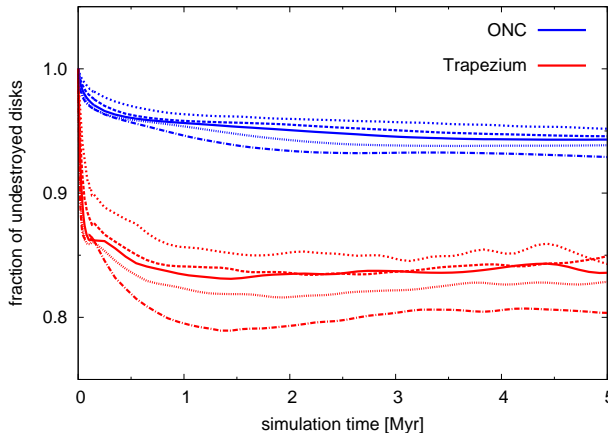


Figure 6.23.: Time evolution of the fraction of stars that possess a circumstellar disc, not restricted to parabolic encounters, for a region of the size of the ONC (blue,  $R = 2.5$  pc) and the Trapezium Cluster (red,  $R = 0.3$  pc). The curves have been smoothed by Bezier curves to avoid intersecting lines. Here the disc size was assumed to be fixed. From top to bottom in each colour regime the cluster model with 1000, 2000, 4000, 8000, and 16000 particles is marked by a short-dashed, long-dashed, solid, dotted, and dot-dashed line, respectively.

masses of  $\sim 5 M_{\odot}$ . The disc-mass loss of the most massive stars remains unaffected by the reevaluation.

Because the low-mass stars in a cluster are dominant in number (as long as the mass function is close to the canonical IMF (2.17)), their reduced disc-mass loss affects the fraction of disc-less stars significantly, as shown in Fig. 6.23. Clearly, the outstanding role of the dense 8000 and 16000 particle models as environments of huge disc destruction, as presented in Fig. 6.8, has to be revised, though it is still considerably larger compared to the ONC model and the sparser clusters. However, one has to consider that this result most probably underestimates the real destructive effect of hyperbolic encounters. This is because, as mentioned above, the applied fit function reduces the disc-mass loss from strong perturbations too much, reducing the potential number of events that can directly remove nearly the complete disc material.

## 7. Discussion

The present work has shown – under the discussed constraints – that the common environment of star formation can act hostile on the discs of its young stellar population. Here the massive stars have been found to play a decisive role, even more so in the less massive clusters. With the finding that disc-destructive encounters leave imprints in the velocity distribution of a star cluster, combining observational data of the velocity distribution and signatures of circumstellar discs presents a future prospect for the observational investigation of the encounter-induced disc-mass loss in different cluster environments. Interrelating the observations with results from numerical simulations, we will come close to answer the question where and when planets find the most promising conditions to form. So far, the presented results imply that intermediate mass stars like our sun in clusters of Orion-type or smaller are most favoured by the planet formation process.

All these effects have been obtained solely by investigating the effect of star-disc encounters. But how would results change if other mechanisms would have been included. In fact, the environmental influences can be manifold: in addition to gravitational interactions with passing stars, winds and radiation from massive stars, or high-velocity shocks from supernovae can have a perturbing effect on a young star's disc or planetary system (e.g. Johnstone *et al.*, 1998; Bonnell *et al.*, 2001b; Ouellette *et al.*, 2007). Because in the present work young star clusters with ages up to 5 Myr are in the focus, only very massive stars could evolve fast enough to end up in a supernova in this short period. Thus more of concern as an external impact on circumstellar discs in the present framework are the two former mechanisms. Naturally, the question arises: on which spatial and temporal scales do these mechanisms act and how far do they interfere with each other?

This question has been only recently addressed by various authors (e.g. Scally & Clarke, 2001; Adams *et al.*, 2004; Moeckel & Bally, 2006). Early simulations have found that the role of encounters is of minor importance and favoured photoevaporation (e.g. Scally & Clarke, 2001). However, more recent investigations show that both mechanisms can play a significant role (Olczak *et al.*, 2006; Adams *et al.*, 2006; Pfalzner *et al.*, 2006; Fatuzzo & Adams, 2008). Whether the two mechanisms might act on different scales is an unsolved problem. Though from numerical simulations it seems that disc destruction due to photoevaporation can occur very fast (Scally & Clarke, 2001; Gorti & Hollenbach, 2008), even on time scales  $< 10^5$  yr,

observations of evaporating discs in young clusters of ages  $\sim 1$  Myr suggest that discs can survive much longer even in strong radiation fields (Bally *et al.*, 1998). The time scales of the destructive effect of encounters depends to a large degree on the radial distance to the cluster centre: in the central region individual discs can be destroyed on time scales as short as  $10^4$  yr, yet due to the statistical nature of this process, even beyond an age of 1 Myr encounter-induced disc destruction has not seized. In both cases, the presence of massive stars seems to play an important role (Pfalzner *et al.*, 2006; Adams *et al.*, 2006). One main difference might be the amount to which a disc may be affected. While it seems that photoevaporation works mainly on the outer parts of discs, but cannot easily destroy the inner discs (Richling & Yorke, 1998; Störzer & Hollenbach, 1999; Balog *et al.*, 2008), stellar encounters can potentially remove all the material from a circumstellar disc in the entire cluster region, though this effect is most pronounced for the most massive stars in the cluster centre (e.g. Olczak *et al.*, 2006; Pfalzner *et al.*, 2006; Moeckel & Bally, 2006).

Hence, it remains unclear whether the effect of star-disc encounters is the main influence that a cluster can exert on its star-disc population for the present investigation of very young stellar systems. However, the comparison of the presented results with observational data has to be taken with care because the applied determination of the encounter-induced disc-mass loss deals with several assumptions. One of these assumptions has been the treatment of all encounters as parabolic flybys. That this simplification does most probably overestimate the disc-destructive effect of encounters has been shown in the investigation of the scaled cluster models in the last chapter (see Section 6.5). Other aspects that have not been included in the simulations, like the relative alignment of discs in an encounter or the effect of repeated encounters, might further reduce the derived disc-mass loss, as has been discussed in Section 4.4.4. However, there are other aspects that imply an opposite trend, among them the fact that all interactions have been assumed to be two-body processes and the treatment of star clusters composed of single stars only.

In the light of these assumptions, how could one improve the method? The effect of hyperbolic encounters could be estimated better by extending the fit function for the disc-mass loss to three parameters, modelling it explicitly as a function of eccentricity. However, this approach has proven to be very difficult and is still under way. As an alternative, tabulated results of the parameter study of star-disc encounters could be used for interpolation. This will be one improvement towards an upcoming investigation. The effect of repeated encounters is already under investigation in the research group and shows indeed a trend towards a – moderately – lower relative disc-mass loss in each additional event. Also, cluster simulations with primordial binary systems are being set up and will show the effect of binary companions on protoplanetary discs in the near future. The treatment of the relative alignment of discs is a very challenging because it involves the extension of the parameter study of star-disc encoun-

ters by two additional parameters. Even more so, the estimate of the disc-mass loss from  $N$ -body encounters with three or more stars involved would require an enormous extension of the parameter space that practically rules out an approach by numerical simulations.

One major step to overcome these difficulties would be the direct simulation of a cluster composed of star-disc systems. However, for a satisfying resolution of the disc-mass loss a circumstellar disc has to be modelled with several thousand particles (cf. Pfalzner, 2003). The integration of a cluster of such systems would require the exact treatment on the order of  $10^6$  particles over several million years and at the same time a time resolution on the order of days. By current standards this is far beyond the scope of a numerical treatment. Nevertheless, first approaches towards hybrid  $N$ -body and tree codes might be capable of managing this challenge in the next years.



## 8. Summary

The present work addresses the question of how far the common star forming environment – star clusters of few to many thousand stars – does affect the evolution of its young star-disc systems. This question is a key aspect of modern astrophysics because it poses constraints on the probability of planet formation which is a fundamental scientific issue.

It was found that encounters of star-disc systems in a young star cluster present an important mechanism that affects young stars and their discs in various modes. Of these, three key results are found:

1. From simulations of a dynamical model of the Orion Nebula Cluster (ONC), based on my previous diploma work, it was shown that disc destruction is dominated by encounters with high-mass stars. These massive cluster members act as gravitational foci for the lower mass stars and are thus subject to repeated encounters in the centre of a stellar cluster. These accumulated perturbations can lead to a total destruction of massive stars' discs and disperse them much more quickly and to a larger degree than for intermediate-mass stars. The consistency with recent observations of IC 348 (Lada *et al.*, 2006), NGC 2362 (Dahm & Hillenbrand, 2007), and the massive cluster NGC 6611 (Oliveira *et al.*, 2005) suggests that this might be a general trend in young massive stellar clusters.
2. The dynamical influence on the hosts of discs, the young stars themselves, has been investigated. It was found from numerical simulations that stars devoid of disc material show unexpectedly high velocities as an outcome of close interactions early on in the cluster development. This feature marks a key observable that could trace the encounter-induced disc-mass loss. Comparison with observations of the ONC confirmed the presence of these so-called “high-velocity stars”, identified as young low-mass stars that partially lack infrared excess emission. The locations of the high-velocity stars form a characteristic pattern that is explained by the numerical simulations, finding a strong correlation between location and disc destruction. Moreover, it was found that the spatial distribution of the high-velocity stars reflects the initial structure and dynamics of the ONC. Eventually, this approach could be generalised to study the evolution of other young dense star clusters, like the Arches cluster, back in time.

3. The influence of different cluster environments on the encounter-induced disc-mass loss has been investigated by scaling the size, density and stellar number of the basic dynamical model of the ONC. It has been found that the disc-mass loss increases with cluster density but remains rather unaffected by the size of the stellar population. However, even in clusters four times sparser than the ONC the effect of encounters is still apparent. The density of the ONC itself marks a threshold: in less dense and less massive clusters it is the massive stars that dominate the encounter-induced disc-mass loss whereas in denser and more massive clusters the low- and intermediate-mass stars play the major role for the removal of disc mass. This finding allows for the extrapolation towards more extreme stellar systems. In case of the Arches cluster one could expect stellar encounters to destroy the discs of most of the low- and high-mass stars in several hundred thousand years.

# Bibliography

- Aarseth, S., 2003, *Gravitational N-body Simulations* (Cambridge, Cambridge University Press, 2003, 430 p.).
- Aarseth, S. J., 1963, MNRAS **126**, 223.
- Aarseth, S. J., 1985, in *IAU Symp. 113: Dynamics of Star Clusters*, pp. 251–258.
- Aarseth, S. J., & M. Lecar, 1975, ARA&A **13**, 1.
- Aarseth, S. J., & K. Zare, 1974, *Celestial Mechanics* **10**, 185.
- Adams, F. C., D. Hollenbach, G. Laughlin, & U. Gorti, 2004, ApJ **611**, 360.
- Adams, F. C., C. J. Lada, & F. H. Shu, 1987, ApJ **312**, 788.
- Adams, F. C., E. M. Proszkow, M. Fatuzzo, & P. C. Myers, 2006, ApJ **641**, 504.
- Ahmad, A., & L. Cohen, 1973, ApJ **179**, 885.
- André, P., S. Basu, & S.-i. Inutsuka, 2008, ArXiv e-prints 0801.4210.
- Andre, P., & T. Montmerle, 1994, ApJ **420**, 837.
- Andrews, S. M., & J. P. Williams, 2005, ApJ **631**, 1134.
- Andrews, S. M., & J. P. Williams, 2007, Ap&SS , 363.
- Anosova, J. P., 1986, Ap&SS **124**, 217.
- Anthony-Twarog, B. J., 1982, AJ **87**, 1213.
- Apai, D., I. Pascucci, J. Bouwman, A. Natta, T. Henning, & C. P. Dullemond, 2005, *Science* **310**, 834.
- Arquilla, R., & P. F. Goldsmith, 1985, ApJ **297**, 436.
- Bally, J., C. R. O'Dell, & M. J. McCaughrean, 2000, AJ **119**, 2919.
- Bally, J., L. Testi, A. Sargent, & J. Carlstrom, 1998, AJ **116**, 854.

- Balog, Z., J. Muzerolle, G. H. Rieke, K. Y. L. Su, & E. T. Young, 2007a, ArXiv Astrophysics e-prints astro-ph/0701741.
- Balog, Z., J. Muzerolle, G. H. Rieke, K. Y. L. Su, E. T. Young, & S. T. Megeath, 2007b, ApJ **660**, 1532.
- Balog, Z., G. H. Rieke, J. Muzerolle, J. Bally, K. Y. L. Su, E. Young, & A. Gaspar, 2008, ArXiv e-prints 0807.3724.
- Bate, M. R., & I. A. Bonnell, 2005, MNRAS **356**, 1201.
- Beckwith, S. V. W., A. I. Sargent, R. S. Chini, & R. Guesten, 1990, AJ **99**, 924.
- Beust, H., R. Reche, & J.-C. Augereau, 2005, in *Protostars and Planets V*, pp. 8092–+.
- Beuther, H., & P. Schilke, 2004, Science **303**, 1167.
- Bik, A., A. Lenorzer, L. Kaper, F. Comerón, L. B. F. M. Waters, A. de Koter, & M. M. Hanson, 2003, A&A **404**, 249.
- Binney, J., & S. Tremaine, 1987, *Galactic dynamics* (Princeton, NJ, Princeton University Press, 1987, 747 p.).
- Boily, C. M., & P. Kroupa, 2003, MNRAS **338**, 673.
- Bonnell, I. A., & M. R. Bate, 2005, MNRAS **362**, 915.
- Bonnell, I. A., M. R. Bate, C. J. Clarke, & J. E. Pringle, 2001a, MNRAS **323**, 785.
- Bonnell, I. A., M. R. Bate, & H. Zinnecker, 1998, MNRAS **298**, 93.
- Bonnell, I. A., & M. B. Davies, 1998, MNRAS **295**, 691.
- Bonnell, I. A., K. W. Smith, M. B. Davies, & K. Horne, 2001b, MNRAS **322**, 859.
- Bonnell, I. A., S. G. Vine, & M. R. Bate, 2004, MNRAS **349**, 735.
- Briceño, C., K. L. Luhman, L. Hartmann, J. R. Stauffer, & J. D. Kirkpatrick, 2002, ApJ **580**, 317.
- Cabrit, S., J. Pety, N. Pesenti, & C. Dougados, 2006, A&A **452**, 897.
- Carpenter, J. M., 2000, AJ **120**, 3139.
- Carpenter, J. M., M. R. Meyer, C. Dougados, S. E. Strom, & L. A. Hillenbrand, 1997, AJ **114**, 198.

- Carpenter, J. M., R. L. Snell, & F. P. Schloerb, 1995, *ApJ* **450**, 201.
- Caselli, P., & P. C. Myers, 1995, *ApJ* **446**, 665.
- Chen, C. H., B. M. Patten, M. W. Werner, C. D. Dowell, K. R. Stapelfeldt, I. Song, J. R. Stauffer, M. Blaylock, K. D. Gordon, & V. Krause, 2005, *ApJ* **634**, 1372.
- Clarke, C. J., I. A. Bonnell, & L. A. Hillenbrand, 2000, *Protostars and Planets IV*, 151.
- Clarke, C. J., & J. E. Pringle, 1991, *MNRAS* **249**, 584.
- Clarke, C. J., & J. E. Pringle, 1993, *MNRAS* **261**, 190.
- Cohn, H., 1979, *ApJ* **234**, 1036.
- Comeron, F., G. H. Rieke, & M. J. Rieke, 1996, *ApJ* **473**, 294.
- Currie, T., S. J. Kenyon, Z. Balog, A. Bragg, & S. Tokarz, 2007, *ApJ* **669**, L33.
- Currie, T., S. J. Kenyon, Z. Balog, G. Rieke, A. Bragg, & B. Bromley, 2008, *ApJ* **672**, 558.
- Dahm, S. E., & L. A. Hillenbrand, 2007, *AJ* **133**, 2072.
- de Pree, C. G., M. C. Nysewander, & W. M. Goss, 1999, *AJ* **117**, 2902.
- de Wit, W. J., L. Testi, F. Palla, & H. Zinnecker, 2005, *A&A* **437**, 247.
- Decin, G., C. Dominik, L. B. F. M. Waters, & C. Waelkens, 2003, *ApJ* **598**, 636.
- Donati, J.-F., J. Babel, T. J. Harries, I. D. Howarth, P. Petit, & M. Semel, 2002, *MNRAS* **333**, 55.
- Duchêne, G., T. Simon, J. Eislöffel, & J. Bouvier, 2001, *A&A* **379**, 147.
- Duquennoy, A., & M. Mayor, 1991, *A&A* **248**, 485.
- Eisner, J. A., & J. M. Carpenter, 2003, *ApJ* **598**, 1341.
- Elmegreen, B. G., & C. J. Lada, 1977, *ApJ* **214**, 725.
- Fall, S. M., R. Chandar, & B. C. Whitmore, 2005, *ApJ* **631**, L133.
- Fatuzzo, M., & F. C. Adams, 2008, *ApJ* **675**, 1361.
- Fűrész, G., L. W. Hartmann, S. T. Megeath, A. H. Szentgyorgyi, & E. T. Hamden, 2008, *ApJ* **676**, 1109.
- Figer, D. F., 2005, *Nature* **434**, 192.

- Gerhard, O., 2000, in *Massive Stellar Clusters*, edited by A. Lançon & C. M. Boily, volume 211 of *Astronomical Society of the Pacific Conference Series*, pp. 12–+.
- Giersz, M., & D. C. Heggie, 1994, *MNRAS* **268**, 257.
- Gómez, M., & S. J. Kenyon, 2001, *AJ* **121**, 974.
- Goodwin, S. P., 1997, *MNRAS* **284**, 785.
- Gorlova, N., G. H. Rieke, J. Muzerolle, J. R. Stauffer, N. Siegler, E. T. Young, & J. H. Stansberry, 2006, *ArXiv Astrophysics e-prints astro-ph/0606039*.
- Gorti, U., & D. Hollenbach, 2008, *ArXiv e-prints 0809.1494*.
- Haisch, K. E., E. A. Lada, & C. J. Lada, 2000, *AJ* **120**, 1396.
- Haisch, K. E., Jr., R. Jayawardhana, & J. Alves, 2005, *ApJ* **627**, L57.
- Haisch, K. E., Jr., E. A. Lada, & C. J. Lada, 2001, *ApJ* **553**, L153.
- Hall, S. M., C. J. Clarke, & J. E. Pringle, 1996, *MNRAS* **278**, 303.
- Harayama, Y., F. Eisenhauer, & F. Martins, 2008, *ApJ* **675**, 1319.
- Hartigan, P., S. Edwards, & L. Ghandour, 1995, *ApJ* **452**, 736.
- Hartmann, L., N. Calvet, E. Gullbring, & P. D’Alessio, 1998, *ApJ* **495**, 385.
- Hartmann, L., P. D’Alessio, N. Calvet, & J. Muzerolle, 2006, *ArXiv Astrophysics e-prints arXiv:astro-ph/0605294*.
- Heggie, D. C., 1974, in *IAU Symp. 62: Stability of the Solar System and of Small Stellar Systems*, edited by Y. Kozai, pp. 225–229.
- Heggie, D. C., 1975, *MNRAS* **173**, 729.
- Heller, C. H., 1993, *ApJ* **408**, 337.
- Heller, C. H., 1995, *ApJ* **455**, 252.
- Henon, M., 1969, *A&A* **2**, 151.
- Hénon, M., 1971, *Ap&SS* **13**, 284.
- Herbst, W., & R. Racine, 1976, *AJ* **81**, 840.
- Hernández, J., L. Hartmann, N. Calvet, R. D. Jeffries, R. Gutermuth, J. Muzerolle, & J. Stauffer, 2008, *ApJ* **686**, 1195.

- Hester, J. J., S. J. Desch, K. R. Healy, & L. A. Leshin, 2004, *Science* **304**, 1116.
- Heyer, M. H., C. Brunt, R. L. Snell, J. Howe, F. P. Schloerb, J. M. Carpenter, M. Normandeau, A. R. Taylor, P. E. Dewdney, Y. Cao, S. Terebey, & C. A. Beichman, 1996, *ApJ* **464**, L175+.
- Hillenbrand, L. A., 1995, Ph.D. Thesis .
- Hillenbrand, L. A., 1997, *AJ* **113**, 1733.
- Hillenbrand, L. A., 2002, ArXiv Astrophysics e-prints astro-ph/0210520.
- Hillenbrand, L. A., 2005, ArXiv Astrophysics e-prints astro-ph/0511083.
- Hillenbrand, L. A., & J. M. Carpenter, 2000, *ApJ* **540**, 236.
- Hillenbrand, L. A., & L. W. Hartmann, 1998, *ApJ* **492**, 540.
- Hillenbrand, L. A., S. E. Strom, N. Calvet, K. M. Merrill, I. Gatley, R. B. Makidon, M. R. Meyer, & M. F. Skrutskie, 1998, *AJ* **116**, 1816.
- Holland, W. S., J. S. Greaves, B. Zuckerman, R. A. Webb, C. McCarthy, I. M. Coulson, D. M. Walther, W. R. F. Dent, W. K. Gear, & I. Robson, 1998, *Nature* **392**, 788.
- Huff, E. M., & S. W. Stahler, 2006, *ApJ* **644**, 355.
- Hughes, A. M., D. J. Wilner, N. Calvet, P. D'Alessio, M. J. Claussen, & M. R. Hogerheijde, 2007, *ApJ* **664**, 536.
- Iben, I. J., 1965, *ApJ* **141**, 993.
- Janes, K. A., C. Tilley, & G. Lynga, 1988, *AJ* **95**, 771.
- Jeffries, R. D., 2007, *MNRAS* **376**, 1109.
- Johnstone, D., D. Hollenbach, & J. Bally, 1998, *ApJ* **499**, 758.
- Jones, B. F., & M. F. Walker, 1988, *AJ* **95**, 1755.
- Jura, M., M. Malkan, R. White, C. Telesco, R. Pina, & R. S. Fisher, 1998, *ApJ* **505**, 897.
- Kastner, J. H., G. Franz, N. Grosso, J. Bally, M. J. McCaughrean, K. Getman, E. D. Feigelson, & N. S. Schulz, 2005, *ApJS* **160**, 511.
- Kenyon, S. J., & B. C. Bromley, 2002a, *AJ* **123**, 1757.
- Kenyon, S. J., & B. C. Bromley, 2002b, *ApJ* **577**, L35.

- Kenyon, S. J., & B. C. Bromley, 2004, *AJ* **127**, 513.
- Kenyon, S. J., & L. Hartmann, 1995, *ApJS* **101**, 117.
- Kessler-Silacci, J. E., L. A. Hillenbrand, G. A. Blake, & M. R. Meyer, 2005, *ApJ* **622**, 404.
- Kim, S. S., D. F. Figer, R. P. Kudritzki, & F. Najarro, 2006, *ApJ* **653**, L113.
- King, I. R., 1966, *AJ* **71**, 64.
- Koen, C., 2006, *MNRAS* **365**, 590.
- Kouwenhoven, M. B. N., A. G. A. Brown, S. F. Portegies Zwart, & L. Kaper, 2007, *A&A* **474**, 77.
- Kraus, S., Y. Y. Balega, J.-P. Berger, K.-H. Hofmann, R. Millan-Gabet, J. D. Monnier, K. Ohnaka, E. Pedretti, T. Preibisch, D. Schertl, F. P. Schloerb, W. A. Traub, *et al.*, 2007, *A&A* **466**, 649.
- Kroupa, P., 1995a, *MNRAS* **277**, 1491.
- Kroupa, P., 1995b, *MNRAS* **277**, 1507.
- Kroupa, P., 2000, *New Astronomy* **4**, 615.
- Kroupa, P., 2001, *MNRAS* **322**, 231.
- Kroupa, P., 2002, *Science* **295**, 82.
- Kroupa, P., 2005, in *The Three-Dimensional Universe with Gaia*, edited by C. Turon, K. S. O'Flaherty, & M. A. C. Perryman, volume 576 of *ESA Special Publication*, pp. 629–+.
- Kroupa, P., S. Aarseth, & J. Hurley, 2001, *MNRAS* **321**, 699.
- Kroupa, P., C. A. Tout, & G. Gilmore, 1993, *MNRAS* **262**, 545.
- Kustaanheimo, P., & E. Stiefel, 1965, *JRAM* **218**, 204.
- Lada, C. J., 1987, in *Star Forming Regions*, edited by M. Peimbert & J. Jugaku, volume 115 of *IAU Symposium*, pp. 1–17.
- Lada, C. J., & E. A. Lada, 2003, *ARA&A* **41**, 57.
- Lada, C. J., M. Margulis, & D. Dearborn, 1984, *ApJ* **285**, 141.
- Lada, C. J., A. A. Muench, K. E. Haisch, Jr., E. A. Lada, J. F. Alves, E. V. Tollestrup, & S. P. Willner, 2000, *AJ* **120**, 3162.

- Lada, C. J., A. A. Muench, E. A. Lada, & J. F. Alves, 2004, *AJ* **128**, 1254.
- Lada, C. J., A. A. Muench, K. L. Luhman, L. Allen, L. Hartmann, T. Megeath, P. Myers, G. Fazio, K. Wood, J. Muzerolle, G. Rieke, N. Siegler, *et al.*, 2006, *AJ* **131**, 1574.
- Lada, E. A., 1992, *ApJ* **393**, L25.
- Lada, E. A., N. J. Evans, D. L. Depoy, & I. Gatley, 1991, *ApJ* **371**, 171.
- Laques, P., & J. L. Vidal, 1979, *A&A* **73**, 97.
- Larson, R. B., 1973, *ARA&A* **11**, 219.
- Larson, R. B., 1984, *MNRAS* **206**, 197.
- Lawson, W. A., A.-R. Lyo, & J. Muzerolle, 2004, *MNRAS* **351**, L39.
- Liebert, J., & R. G. Probst, 1987, *ARA&A* **25**, 473.
- Lin, S.-Y., N. Ohashi, J. Lim, P. T. P. Ho, M. Fukagawa, & M. Tamura, 2006, *ApJ* **645**, 1297.
- Liu, W. M., M. R. Meyer, A. S. Cotera, & E. T. Young, 2003, *AJ* **126**, 1665.
- Luhman, K. L., & G. H. Rieke, 1999, *ApJ* **525**, 440.
- Luhman, K. L., G. H. Rieke, E. T. Young, A. S. Cotera, H. Chen, M. J. Rieke, G. Schneider, & R. I. Thompson, 2000, *ApJ* **540**, 1016.
- Lyo, A.-R., W. A. Lawson, E. E. Mamajek, E. D. Feigelson, E.-C. Sung, & L. A. Crause, 2003, *MNRAS* **338**, 616.
- Lyons, J. R., & E. D. Young, 2005, *Nature* **435**, 317.
- Maíz Apellániz, J., N. R. Walborn, N. I. Morrell, V. S. Niemela, & E. P. Nelan, 2007, *ApJ* **660**, 1480.
- Makino, J., 1991, *ApJ* **369**, 200.
- Makino, J., & S. J. Aarseth, 1992, *PASJ* **44**, 141.
- Makino, J., & P. Hut, 1988, *ApJS* **68**, 833.
- Makino, J., M. Taiji, T. Ebisuzaki, & D. Sugimoto, 1997, *ApJ* **480**, 432.
- Malkov, O., & H. Zinnecker, 2001, *MNRAS* **321**, 149.
- Mamajek, E. E., M. R. Meyer, P. M. Hinz, W. F. Hoffmann, M. Cohen, & J. L. Hora, 2004, *ApJ* **612**, 496.

- Massey, P., 1998, in *ASP Conf. Ser. 142: The Stellar Initial Mass Function (38th Herstmonceux Conference)*, edited by G. Gilmore & D. Howell, pp. 17–+.
- Massey, P., L. R. Penny, & J. Vukovich, 2002, *ApJ* **565**, 982.
- Massi, F., L. Testi, & L. Vanzi, 2006, *A&A* **448**, 1007.
- Mathieu, R. D., 1994, *ARA&A* **32**, 465.
- Mayne, N. J., & T. Naylor, 2008, *ArXiv e-prints* **801**.
- McCaughrean, M., H. Zinnecker, M. Andersen, G. Meeus, & N. Lodieu, 2002, *The Messenger* **109**, 28.
- McCaughrean, M. J., & C. R. O'Dell, 1996, *AJ* **111**, 1977.
- McCaughrean, M. J., & J. R. Stauffer, 1994, *AJ* **108**, 1382.
- McKee, C. F., & J. C. Tan, 2003, *ApJ* **585**, 850.
- McMillan, S. L. W., & P. Hut, 1996, *ApJ* **467**, 348.
- Menten, K. M., M. J. Reid, J. Forbrich, & A. Brunthaler, 2007, *A&A* **474**, 515.
- Meyer, M. R., 1996, Ph.D. Thesis .
- Meyer, M. R., F. C. Adams, L. A. Hillenbrand, J. M. Carpenter, & R. B. Larson, 2000, *Protostars and Planets IV* , 121.
- Meyer, M. R., D. E. Backman, A. J. Weinberger, & M. C. Wyatt, 2006, *ArXiv Astrophysics e-prints astro-ph/0606399*.
- Meyer, M. R., N. Calvet, & L. A. Hillenbrand, 1997, *AJ* **114**, 288.
- Mikkola, S., & S. J. Aarseth, 1993, *Celestial Mechanics and Dynamical Astronomy* **57**, 439.
- Moeckel, N., & J. Bally, 2006, *ApJ* **653**, 437.
- Moeckel, N., & J. Bally, 2007a, *ApJ* **661**, L183.
- Moeckel, N., & J. Bally, 2007b, *ApJ* **656**, 275.
- Muench, A. A., E. A. Lada, & C. J. Lada, 2000, *ApJ* **533**, 358.
- Muench, A. A., E. A. Lada, C. J. Lada, & J. Alves, 2001, *Bulletin of the American Astronomical Society* **33**, 1423.

- Muench, A. A., E. A. Lada, C. J. Lada, & J. Alves, 2002, *ApJ* **573**, 366.
- Mundy, L. G., L. W. Looney, & W. J. Welch, 2000, *Protostars and Planets IV*, 355.
- Muzerolle, J., N. Calvet, C. Briceño, L. Hartmann, & L. Hillenbrand, 2000, *ApJ* **535**, L47.
- Myers, P. C., & P. J. Benson, 1983, *ApJ* **266**, 309.
- O'Dell, C. R., Z. Wen, & X. Hu, 1993, *ApJ* **410**, 696.
- O'Dell, C. R., & K. Wong, 1996, *AJ* **111**, 846.
- Oey, M. S., & C. J. Clarke, 2005, *ApJ* **620**, L43.
- Olczak, C., S. Pfalzner, & R. Spurzem, 2006, *ApJ* **642**, 1140.
- Oliveira, J. M., R. D. Jeffries, & J. T. van Loon, 2004, *MNRAS* **347**, 1327.
- Oliveira, J. M., R. D. Jeffries, J. T. van Loon, S. P. Littlefair, & T. Naylor, 2005, *MNRAS* **358**, L21.
- Öpik, E., 1924, *Tartu Obs. Publ.* **25**, No. 6.
- Ostriker, E. C., 1994, *ApJ* **424**, 292.
- Ouellette, N., S. J. Desch, & J. J. Hester, 2007, *ApJ* **662**, 1268.
- Padgett, D. L., S. E. Strom, & A. Ghez, 1997, *ApJ* **477**, 705.
- Palla, F., 2005, in *Massive Star Birth: A Crossroads of Astrophysics*, edited by R. Cesaroni, M. Felli, E. Churchwell, & M. Walmsley, volume 227 of *IAU Symposium*, pp. 196–205.
- Palla, F., & D. Galli, 1997, *ApJ* **476**, L35+.
- Palla, F., & S. W. Stahler, 1999, *ApJ* **525**, 772.
- Palla, F., & S. W. Stahler, 2000, *ApJ* **540**, 255.
- Patel, N. A., P. F. Goldsmith, M. H. Heyer, R. L. Snell, & P. Pratap, 1998, *ApJ* **507**, 241.
- Pfalzner, S., 2003, *ApJ* **592**, 986.
- Pfalzner, S., 2004, *ApJ* **602**, 356.
- Pfalzner, S., 2006, *ApJ* **652**, L129.
- Pfalzner, S., & C. Olczak, 2007a, *A&A* **462**, 193.

- Pfalzner, S., & C. Olczak, 2007b, *A&A* **475**, 875.
- Pfalzner, S., C. Olczak, & A. Eckart, 2006, *A&A* **454**, 811.
- Pfalzner, S., J. Tackenberg, & M. Steinhausen, 2008, *A&A* **487**, L45.
- Pfalzner, S., S. Umbreit, & T. Henning, 2005a, *ApJ* **629**, 526.
- Pfalzner, S., P. Vogel, J. Scharwächter, & C. Olczak, 2005b, *A&A* **437**, 967.
- Phelps, R. L., & K. A. Janes, 1994, *ApJS* **90**, 31.
- Pinto, F., 1987, *PASP* **99**, 1161.
- Plummer, H. C., 1911, *MNRAS* **71**, 460.
- Preibisch, T., Y. Balega, K.-H. Hofmann, G. Weigelt, & H. Zinnecker, 1999, *New Astronomy* **4**, 531.
- Preibisch, T., Y.-C. Kim, F. Favata, E. D. Feigelson, E. Flaccomio, K. Getman, G. Micela, S. Sciortino, K. Stassun, B. Stelzer, & H. Zinnecker, 2005, *ApJS* **160**, 401.
- Press, W. H., S. A. Teukolsky, W. T. Vetterling, B. P. Flannery, C. Lloyd, P. Rees, S. A. Teukolsky, W. T. Vetterling, B. P. Flannery, C. Lloyd, & P. Rees, 1993, *The Observatory* **113**, 214.
- Pringle, J. E., 1981, *ARA&A* **19**, 137.
- Przygodda, F., R. van Boekel, P. Àbrahàm, S. Y. Melnikov, L. B. F. M. Waters, & C. Leinert, 2003, *A&A* **412**, L43.
- Reid, M. A., & C. D. Wilson, 2006, *ApJ* **644**, 990.
- Reipurth, B., M. M. Guimarães, M. S. Connelley, & J. Bally, 2007, *AJ* **134**, 2272.
- Richling, S., & H. W. Yorke, 1998, *A&A* **340**, 508.
- Rieke, G. H., K. Y. L. Su, J. A. Stansberry, D. Trilling, G. Bryden, J. Muzerolle, B. White, N. Gorlova, E. T. Young, C. A. Beichman, K. R. Stapelfeldt, & D. C. Hines, 2005, *ApJ* **620**, 1010.
- Rucinski, S. M., 2001, *AJ* **122**, 1007.
- Sagar, R., & T. Richtler, 1991, *A&A* **250**, 324.
- Saigo, K., K. Tomisaka, & T. Matsumoto, 2008, *ApJ* **674**, 997.

- Salpeter, E. E., 1955, *ApJ* **121**, 161.
- Scally, A., & C. Clarke, 2001, *MNRAS* **325**, 449.
- Scally, A., C. Clarke, & M. J. McCaughrean, 2005, *MNRAS* **358**, 742.
- Scalo, J., 1998, in *ASP Conf. Ser. 142: The Stellar Initial Mass Function (38th Herstmonceux Conference)*, edited by G. Gilmore & D. Howell, pp. 201–+.
- Scalo, J. M., 1986, *Fundamentals of Cosmic Physics* **11**, 1.
- Schoedel, R., D. Merritt, & A. Eckart, 2008, *ArXiv e-prints* 0810.0204.
- Shatsky, N., & A. Tokovinin, 2002, *A&A* **382**, 92.
- Shu, F. H., F. C. Adams, & S. Lizano, 1987, *ARA&A* **25**, 23.
- Shuping, R. Y., M. Kassis, M. Morris, N. Smith, & J. Bally, 2006, *ApJ* **644**, L71.
- Sicilia-Aguilar, A., L. Hartmann, N. Calvet, S. T. Megeath, J. Muzerolle, L. Allen, P. D'Alessio, B. Merín, J. Stauffer, E. Young, & C. Lada, 2006, *ApJ* **638**, 897.
- Sicilia-Aguilar, A., L. W. Hartmann, J. Hernández, C. Briceño, & N. Calvet, 2005a, *AJ* **130**, 188.
- Sicilia-Aguilar, A., L. W. Hartmann, A. H. Szentgyorgyi, D. G. Fabricant, G. Fűrész, J. Roll, M. A. Conroy, N. Calvet, S. Tokarz, & J. Hernández, 2005b, *AJ* **129**, 363.
- Silverstone, M. D., M. R. Meyer, E. E. Mamajek, D. C. Hines, L. A. Hillenbrand, J. Najita, I. Pascucci, J. Bouwman, J. S. Kim, J. M. Carpenter, J. R. Stauffer, D. E. Backman, *et al.*, 2006, *ApJ* **639**, 1138.
- Simon, M., & L. Prato, 1995, *ApJ* **450**, 824.
- Simón-Díaz, S., A. Herrero, C. Esteban, & F. Najarro, 2006, *A&A* **448**, 351.
- Skrutskie, M. F., D. Dutkevitch, S. E. Strom, S. Edwards, K. M. Strom, & M. A. Shure, 1990, *AJ* **99**, 1187.
- Slesnick, C. L., L. A. Hillenbrand, & J. M. Carpenter, 2004, *ApJ* **610**, 1045.
- Smith, B. A., & R. J. Terrile, 1984, *Science* **226**, 1421.
- Snell, R. L., 1981, *ApJS* **45**, 121.
- Spangler, C., A. I. Sargent, M. D. Silverstone, E. E. Becklin, & B. Zuckerman, 2001, *ApJ* **555**, 932.

- Spitzer, L. J., & M. H. Hart, 1971, *ApJ* **164**, 399.
- Spurzem, R., 1999, *Journal of Computational and Applied Mathematics* **109**, 407.
- Stahler, S. W., F. Palla, & E. E. Salpeter, 1986, *ApJ* **302**, 590.
- Stassun, K. G., R. D. Mathieu, T. Mazeh, & F. J. Vrba, 1999, *AJ* **117**, 2941.
- Sterzik, M. F., & R. H. Durisen, 1995, *A&A* **304**, L9+.
- Stolte, A., W. Brandner, B. Brandl, & H. Zinnecker, 2006, *AJ* **132**, 253.
- Stolte, A., W. Brandner, B. Brandl, H. Zinnecker, & E. K. Grebel, 2004, *AJ* **128**, 765.
- Störzer, H., & D. Hollenbach, 1999, *ApJ* **515**, 669.
- Strom, S. E., K. M. Strom, & G. L. Grasdalen, 1975, *ARA&A* **13**, 187.
- Tachibana, S., & G. R. Huss, 2003, *ApJ* **588**, L41.
- Takeuchi, T., & P. Artymowicz, 2001, *ApJ* **557**, 990.
- Tan, J. C., 2004, *ApJ* **607**, L47.
- Terebey, S., F. H. Shu, & P. Cassen, 1984, *ApJ* **286**, 529.
- Testi, L., F. Palla, & A. Natta, 1998, *A&AS* **133**, 81.
- Testi, L., F. Palla, T. Prusti, A. Natta, & S. Maltagliati, 1997, *A&A* **320**, 159.
- Throop, H. B., & J. Bally, 2005, *ApJ* **623**, L149.
- Trimble, V., 1990, *MNRAS* **242**, 79.
- Umbreit, S., 2001, *Simulation der Wechselwirkung von Akkretionsscheiben in dichten Sternhaufen*, Diploma thesis, University of Jena, Germany.
- Umbreit, S., 2005, *The Theory of the Formation of Brown Dwarfs*, Ph.D. thesis, University of Heidelberg, Germany.
- Valtonen, M., 2004, in *Revista Mexicana de Astronomia y Astrofisica Conference Series*, edited by C. Allen & C. Scarfe, volume 21 of *Revista Mexicana de Astronomia y Astrofisica Conference Series*, pp. 147–151.
- Valtonen, M., & S. Mikkola, 1991, *ARA&A* **29**, 9.
- Valtonen, M., A. Mylläri, V. Orlov, & A. Rubinov, 2005, *MNRAS* **364**, 91.

- Valtonen, M. J., 1997, ApJ **485**, 785.
- van Albada, T. S., 1968, BAN **19**, 479.
- van Altena, W. F., J. T. Lee, J.-F. Lee, P. K. Lu, & A. R. Upgren, 1988, AJ **95**, 1744.
- van Boekel, R., L. B. F. M. Waters, C. Dominik, J. Bouwman, A. de Koter, C. P. Dullemond, & F. Paresce, 2003, A&A **400**, L21.
- Verschueren, W., & M. David, 1989, A&A **219**, 105.
- Vicente, S. M., & J. Alves, 2005, A&A **441**, 195.
- Weidenschilling, S. J., 1977, Ap&SS **51**, 153.
- Weidner, C., & P. Kroupa, 2004, MNRAS **348**, 187.
- Weidner, C., & P. Kroupa, 2006, MNRAS **365**, 1333.
- Weigelt, G., Y. Balega, T. Preibisch, D. Schertl, M. Schöller, & H. Zinnecker, 1999, A&A **347**, L15.
- Weinberger, A. J., E. E. Becklin, B. Zuckerman, & I. Song, 2004, AJ **127**, 2246.
- White, G. J., B. Lefloch, C. V. M. Fridlund, C. A. Aspin, G. Dahmen, N. R. Minchin, & M. Huldgren, 1997, A&A **323**, 931.
- Williams, J. P., S. M. Andrews, & D. J. Wilner, 2005, ApJ **634**, 495.
- Wilson, T. L., L. Filges, C. Codella, W. Reich, & P. Reich, 1997, A&A **327**, 1177.
- Wolk, S. J., & F. M. Walter, 1996, AJ **111**, 2066.
- Zhang, Q., 2005, in *Massive Star Birth: A Crossroads of Astrophysics*, edited by R. Cesaroni, M. Felli, E. Churchwell, & M. Walmsley, volume 227 of *IAU Symposium*, pp. 135–144.
- Zinnecker, H., & H. W. Yorke, 2007, ARA&A **45**, 481.



# A. Conic Sections

A conic section is the curve obtained by intersecting a circular conical surface, or cone, with a plane. There are three types of conic sections known as ellipse, parabola and hyperbola, with eccentricities of  $0 \leq e < 1$ ,  $e = 1$ , and  $e > 1$ , respectively. In the two-body problem they correspond to orbits of systems with total energy  $E < 0$ ,  $E = 0$ , and  $E > 0$ .

In the following the calculations will be taken out in a frame which is centred on one body, while the other is moving on a orbit of one of the given type.

To determine the angle  $\psi_{\text{slr}}$  enclosed by the separation and the velocity vector at semi-latus rectum,  $\vec{r}_{\text{slr}}$  and  $\vec{v}_{\text{slr}}$ , the conservation of the specific angular momentum  $\vec{l}$  has to be considered.

At periastron,

$$l = |\vec{l}| = r_{\text{p}}v_{\text{p}} = \sqrt{GM(1+e)r_{\text{p}}},$$

where the subscript p denotes the periastron, while at semi-latus rectum,

$$l = |\vec{l}| = r_{\text{slr}}v_{\text{slr}} \sin \psi_{\text{slr}}.$$

The norm of the separation and velocity vector,  $r = |\vec{r}|$  and  $v = |\vec{v}|$ , of the orbiting body at any point is given by

$$r = \frac{a(1-e^2)}{1+e \cos \varphi}, \quad v^2 = GM \left( \frac{2}{r} - \frac{1}{a} \right), \quad a = \frac{r_{\text{p}}}{1-e} \quad \text{if } 0 \leq e < 1, \quad (\text{A.1})$$

$$r = \frac{2r_{\text{p}}}{1+e \cos \varphi}, \quad v^2 = \frac{2GM}{r} \quad \text{if } e = 1, \quad (\text{A.2})$$

$$r = \frac{a(e^2-1)}{1+e \cos \varphi}, \quad v^2 = GM \left( \frac{2}{r} + \frac{1}{a} \right), \quad a = \frac{r_{\text{p}}}{e-1} \quad \text{if } e > 1. \quad (\text{A.3})$$

At semi-latus rectum  $\varphi = \pi/2$ , leading to one single expression valid for all three conic section types,

$$\sin \psi_{\text{slr}} = \frac{1}{\sqrt{e^2+1}}. \quad (\text{A.4})$$



## B. Observational Constraints

### B.1. Observability of tidal tails due to star-disc encounters in the ONC

The relevant physical quantity that determines the prominence of tidal tails due to an encounter is the change of angular momentum in the disc. According to Pfalzner & Olczak (2007a), it is valid to assume that a fractional angular momentum loss (AML) of at least 10 % is required to form observationally detectable tidal tails (see also Fig. 9 and 10 of Pfalzner & Olczak, 2007a).

For an estimate of the rate of encounters in the ONC in which the AML is at least 10 % one might consider an encounter of a star with mass  $m = 0.5 M_{\odot}$ , which corresponds to the mean stellar mass in the ONC (see §4.1). A star of that mass is thought to be surrounded by a protoplanetary disc of typical size  $r_d = 100$  AU. To be on the safe side, the estimate should involve the upper limit of the encounter rate and the assumption that the encounter partner is the highest mass star of the ONC,  $M = 50 M_{\odot}$ . Referring to Table 1 of Pfalzner & Olczak (2007a), the specified minimum AML requires an encounter at a relative periastron  $r_p/r_d \approx 10$ , or a periastron  $r_p \approx 1000$  AU. Moreover, the encounter is assumed to have occurred in the Trapezium Cluster (TC), the dense central part of the ONC, where it is most probable (see Fig. 4 of Pfalzner *et al.*, 2006). The number of stars, the density and the velocity dispersion of the TC are  $N_{\text{TC}} \approx 750$ ,  $\rho_{\text{TC}} \approx 10^3 \text{ pc}^{-3}$ , and  $\sigma_{\text{ID}}^{\text{JW}} = 2.5 \text{ km s}^{-1}$  (see Section 4.1).

The time scale for encounters of the assumed type is given by Eq. (C.1); substituting  $n = \rho_{\text{TC}}$ ,  $\sigma = \sigma_{\text{ID}}^{\text{JW}}$ ,  $r_{\star} = r_p$ , and  $m_{\star} = M$ , one arrives at  $t_{\text{enc}} \approx 2 \cdot 10^5 \text{ yr}$ . With a dissipation time scale of the tidal tails of  $t_{\text{diss}} \lesssim 1000 \text{ yr}$ , the probability of a detection is roughly  $P_{\text{obs}} \lesssim t_{\text{diss}}/t_{\text{enc}} \approx 5 \cdot 10^{-3}$ . With the number of stars in the TC,  $N_{\text{TC}}$ , one expects at most  $N_{\text{obs}} \lesssim P_{\text{obs}} N_{\text{TC}} \approx 4$  stars to be accompanied by tidal tails that could be observed at the current time.

### B.2. Estimate of the mean uncertainty of stellar ages

Since individual errors of the derived stellar ages are not provided by Hillenbrand (1997), one has to estimate the mean error from the quoted observational and theoretical uncertainties and

the constructed HR diagram. The uncertainties of the derived luminosities,  $\log(L_*/L_\odot) \lesssim 0.2$ , translate into an age uncertainty of  $\sim 0.2$ - $0.4$  dex for stars with masses  $1.0$ - $0.1 M_\odot$ . Uncertainties of the derived effective temperatures,  $\log T_{\text{eff}} \lesssim 0.02$ , translate into an age uncertainty of typically  $\sim 0.3$  dex, but can be as large as  $\sim 1$  dex for stars with mass  $\lesssim 0.1 M_\odot$ . Further uncertainties of the derived ages are introduced due to differences between different pre-main-sequence evolutionary tracks, which can be as large as  $0.6$  dex. Assuming a typical uncertainty of  $0.3$  dex due to uncertainties from luminosity, effective temperature and evolutionary tracks a mean uncertainty of stellar ages of  $\sim 0.5$  dex is estimated.

## C. Stellar Dynamics

### C.1. Minimum velocity for unperturbed escape of stars in the ONC

High-velocity stars that have been generated due to a close triple encounter in the cluster centre are expected to leave the cluster without significant perturbation. This is due to the fact that (a) the fractional change of the velocity  $v$  of a high-velocity star is less than 10 % unless the impact parameter is not lower than 100 AU (Binney & Tremaine, 1987, Eq. 4-8), and (b) only a small fraction of stars experiences more than one encounter closer than 100 AU in one crossing time of the ONC (Scally & Clarke, 2001; Olczak *et al.*, 2006). Alternatively, one can evaluate the collision time scale of the escaper and a binary with semi-major axis  $a \approx 100$  AU in the ONC (Binney & Tremaine, 1987, Eq. 8-123),

$$t_{\text{coll}} = \left[ 16\sqrt{\pi}n\sigma r_{\star}^2 \left( 1 + \frac{Gm_{\star}}{2\sigma^2 r_{\star}} \right) \right]^{-1} \approx 10 \text{ Myr}, \quad (\text{C.1})$$

where the gravitational focusing of a  $10 M_{\odot}$  binary in the dense Trapezium Cluster has been considered in order to obtain a robust lower limit on  $t_{\text{coll}}$ , using  $r_{\star} = a$ ,  $n = \rho_{\text{TC}} \approx 10^3 \text{ pc}^{-3}$  and  $\sigma = \sigma_{3\text{D}}^{\text{JW}} = \sqrt{3}\sigma_{1\text{D}}^{\text{JW}} = 4.3 \text{ km s}^{-1}$  (see Section 4.1). Since the collision time scale is much longer than the time to reach the cluster outskirts,  $t_{\text{coll}} \gtrsim 10 \text{ Myr} \gg 0.2 \text{ Myr} \gtrsim t_{\text{esc}}$ , it is valid to assume that stars with velocities  $v \geq 3\sigma_{3\text{D}}^{\text{JW}}$  are effectively unperturbed before they escape from the cluster.

### C.2. Maximum velocity of a star ejected from a bound triple system

The maximum velocity of a star that has been ejected from a bound triple system is obtained from the analysis of a triple system after the ejection event forming a configuration of a binary

and an escaping body (cf. Valtonen *et al.*, 2005). The total energy of the system is then

$$E_0 = \frac{1}{2}m\dot{r}_s^2 - G\frac{m_B m_s}{r_s} + \frac{1}{2}M\dot{r}^2 - G\frac{m_a m_b}{r}, \quad (\text{C.2})$$

where  $r_s$  is the separation of the third body relative to the barycentre of the binary,  $r$  the separation of the binary components,  $m_s$ ,  $m_a$  and  $m_b$  the masses of the escaper and the binary components,  $m_B = m_a + m_b$  the binary mass, and  $M = m_a m_b / m_B$  and  $m = m_B m_s / (m_B + m_s)$  the reduced masses.

The observational detection of the escaper will usually occur when the distance to the binary components greatly exceeds the size of the binary system,  $r_s \gg r$ . Thus one can neglect the second term in Eq. (C.2). Moreover, in most cases the ejected body will be the lowest mass component of the triple system,  $m_s \ll m_B$  (see Section 5.2.2), hence Eq. (C.2) reduces to

$$E_0 = \frac{1}{2}m_s \dot{r}_s^2 + \frac{1}{2}M\dot{r}^2 - G\frac{m_a m_b}{r} = \frac{1}{2}m_s \dot{r}_s^2 - G\frac{m_a m_b}{2a}, \quad (\text{C.3})$$

where the last term denotes the total binary energy in the general case of an elliptical orbit with semi-major axis  $a$ .

Using the same parameters for the triple system as in Section 5.2.2 and assuming a nearly equal-mass binary,  $m_s = 0.25 M_\odot$ ,  $2a = 100$  AU,  $m_a m_b \approx 4 M_\odot$ , one finds from Eq. (C.3) the maximum velocity of the escaper from a triple system with negative total energy,  $v_s = \dot{r}_s \lesssim 18 \text{ km s}^{-1}$ . In fact, the simulations show that the binary that generates a high-velocity star never is less massive than  $10 M_\odot$  and usually exceeds  $20 M_\odot$ , and the mass ratio is never below  $1/6$  and usually about  $1/3$ . Using these parameters, one finds  $v_s \lesssim 30\text{-}80 \text{ km s}^{-1}$ .

## D. Star Cluster Models

### D.1. Determination of boundaries of mass groups

Boundaries of mass groups of low-, intermediate- and high-mass stars have been determined individually for different sizes of stellar populations on the basis of the canonical IMF (Kroupa, 2001, but see also Section 2.4). The derivation involves the requirement for the three mass ranges to be equidistant in logarithmic space, weighted by the slope of the IMF (of each mass range). The weighting accounts for the steepness of the slope in the high-mass regime which would otherwise cause a very sparsely populated group of high-mass stars.

In the case of a lower mass cutoff at  $m_0 = 0.08 M_\odot$ , and an upper mass limit  $m_3$ , the IMF is characterised by just two different slopes,  $\alpha_1 = 1.3$  in the range  $m_0 \leq m < 0.50 M_\odot$ , and  $\alpha_2 = 2.3$  in the range  $0.50 M_\odot \leq m \leq m_3$ . Because the break in the slope of the IMF at the critical mass  $m_c^{\text{br}} = 0.5 M_\odot$  does not necessarily coincide with one of the boundaries of the mass ranges, the cases  $m_1 < m_c^{\text{br}}$  and  $m_1 \geq m_c^{\text{br}}$  have to be differentiated. Though from the theoretical point of view the same differentiation would be required for the higher mass boundary  $m_2$ , this is not relevant for the stellar systems in the focus of the present work. The four mass ranges,  $m_k$ ,  $k = 0, \dots, 3$ , and the two slopes,  $\alpha_k$ ,  $k = 1, 2$ , are then interrelated as follows:

$$\begin{aligned}
 (m_1 \geq m_c^{\text{br}}) \wedge (m_2 \geq m_c^{\text{br}}) : & \quad (\log m_1 - \log m_c^{\text{br}}) \alpha_2^{-1} + (\log m_c^{\text{br}} - \log m_0) \alpha_1^{-1} \\
 & \quad \equiv (\log m_2 - \log m_1) \alpha_2^{-1} \\
 & \quad \equiv (\log m_3 - \log m_2) \alpha_2^{-1},
 \end{aligned} \tag{D.1}$$

$$\begin{aligned}
 (m_1 < m_c^{\text{br}}) \wedge (m_2 \geq m_c^{\text{br}}) : & \quad (\log m_1 - \log m_0) \alpha_1^{-1} \\
 & \quad \equiv (\log m_2 - \log m_c^{\text{br}}) \alpha_2^{-1} + (\log m_c^{\text{br}} - \log m_1) \alpha_1^{-1} \\
 & \quad \equiv (\log m_3 - \log m_2) \alpha_2^{-1}.
 \end{aligned}$$

	1000	2000	4000	8000	16000
$m_0[M_\odot]$	$8.00 \cdot 10^{-2}$				
$m_1[M_\odot]$	$3.30 \cdot 10^{-1}$	$3.54 \cdot 10^{-1}$	$3.82 \cdot 10^{-1}$	$3.95 \cdot 10^{-1}$	$4.15 \cdot 10^{-1}$
$m_2[M_\odot]$	2.94	3.78	4.95	5.58	6.61
$m_3[M_\odot]$	$1.47 \cdot 10^2$	$1.47 \cdot 10^2$	$1.48 \cdot 10^2$	$1.48 \cdot 10^2$	$1.50 \cdot 10^2$

Table D.1.: Boundaries of the three mass groups of low-, intermediate-, and high-mass stars of the density-scaled and size-scaled models with 1000, 2000, 4000, 8000, and 16000 particles.

Solving these equations, and substituting  $\alpha_{12} \equiv \alpha_1 \alpha_2^{-1}$ ,  $\alpha_{21} \equiv \alpha_2 \alpha_1^{-1}$ , one obtains

$$\begin{aligned}
 m_1 \geq m_c^{\text{br}} : & \begin{cases} \log m_1 = \frac{1}{3} [\log m_3 + 2(1 - \alpha_{21}) \log m_c^{\text{br}} + 2\alpha_{21} \log m_0] \\ \log m_2 = \frac{1}{3} [2 \log m_3 + (1 - \alpha_{21}) \log m_c^{\text{br}} + \alpha_{21} \log m_0] \end{cases}, \\
 m_1 < m_c^{\text{br}} : & \begin{cases} \log m_1 = \frac{1}{3} [\alpha_{12} \log m_3 + (1 - \alpha_{12}) \log m_c^{\text{br}} + 2 \log m_0] \\ \log m_2 = \frac{1}{3} [2 \log m_3 + (1 - \alpha_{21}) \log m_c^{\text{br}} + \alpha_{21} \log m_0] \end{cases},
 \end{aligned} \tag{D.2}$$

under the restriction  $m_2 \geq m_c^{\text{br}}$ . The choice of the appropriate solution is determined by the upper mass limit  $m_3$ . For this purpose the ‘‘critical maximum mass’’  $m_c^{\text{max}}$ ,

$$m_c^{\text{max}} = \log^{-1} [(1 + 2\alpha_{12}) \log m_c^{\text{br}} - 2\alpha_{12} \log m_0], \tag{D.3}$$

is estimated from Eq. (D.2) and  $m_1 \equiv m_c^{\text{br}}$ . Consequently, the following relations hold:

$$\begin{aligned}
 m_3 < m_c^{\text{max}} & \implies m_1 \geq m_c^{\text{br}}, \\
 m_3 \geq m_c^{\text{max}} & \implies m_1 < m_c^{\text{br}}.
 \end{aligned} \tag{D.4}$$

With the given values of the parameters  $m_0$ ,  $\alpha_1$ , and  $\alpha_2$  one finds

$$m_c^{\text{max}} \approx 3.97 M_\odot.$$

The derived mass boundaries,  $m_k$ ,  $k = 0, \dots, 3$ , for each cluster of the families of models are presented in Table D.1.





# Acknowledgements

I would like to express my thanks to everyone who supported me during my studies of physics.

First and foremost, I thank Prof. Dr. Susanne Pfalzner and Prof. Dr. Andreas Eckart for giving me the opportunity to write this thesis under their supervision. It has been a great experience.

Big, big thanks go as well to the (unfortunately small) group of “theoreticians”: lively discussions, heavy coding, funny conferences, and a superb working atmosphere with Thomas Kaczmarek, Manuel Steinhausen, Christina Hövel and Jochen Tackenberg – all this (and much, much more) will remain unforgotten.

Similarly, great table football fights, (rare) tea sessions, mad hat constructions, and exciting observing sessions in Effelsberg would have been impossible without Sebastian Fischer, Jens Zuther, Rainer Schödel, Koraljka Muzic, Sabine König, Macarena Garcia Marin, Steffen Rost, and Gunther Witzel.

Thanks also go to the whole group whose kind working atmosphere makes astrophysics fun.

And last but not least I would like to thank my family and my lovely girlfriend, and my friends for their endless support, ongoing encouragement and probing questions.



# Erklärung

“Ich versichere, dass ich die von mir vorgelegte Dissertation selbständig angefertigt, die benutzten Quellen und Hilfsmittel vollständig angegeben und die Stellen der Arbeit – einschließlich Tabellen, Karten und Abbildungen –, die anderen Werken im Wortlaut oder dem Sinn nach entnommen sind, in jedem Einzelfall als Entlehnung kenntlich gemacht habe; dass diese Dissertation noch keiner anderen Fakultät oder Universität zur Prüfung vorgelegen hat; dass sie – abgesehen von unten angegebenen Teilpublikationen – noch nicht veröffentlicht worden ist sowie, dass ich eine solche Veröffentlichung vor Abschluss des Promotionsverfahrens nicht vornehmen werde. Die Bestimmungen der Promotionsordnung sind mir bekannt. Die von mir vorgelegte Dissertation ist von Frau Prof. Dr. Susanne Pfalzner betreut worden.”

Köln, 1. März 2009



